

ENHANCED HYDROGEN SORPTION PROPERTIES OF MgH_2 -BASED
SYSTEMS FOR HYDROGEN STORAGE APPLICATIONS



SOPHIDA THIANGVIRIYA

A Thesis Submitted in Partial Fulfillment of the Requirements for the
Degree of Doctor of Philosophy in Chemistry
Suranaree University of Technology
Academic Year 2021

การเพิ่มคุณสมบัติการดูดซับไฮโดรเจนของแมกนีเซียมไฮไดรด์
สำหรับการประยุกต์ใช้เป็นแหล่งกักเก็บไฮโดรเจน

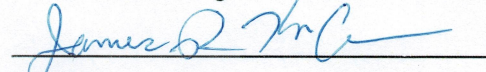


วิทยานิพนธ์นี้เป็นส่วนหนึ่งของการศึกษาตามหลักสูตรปริญญาวิทยาศาสตรดุษฎีบัณฑิต
สาขาวิชาเคมี
มหาวิทยาลัยเทคโนโลยีสุรนารี
ปีการศึกษา 2564

ENHANCED HYDROGEN SORPTION PROPERTIES OF
MgH₂-BASED SYSTEMS FOR HYDROGEN STORAGE APPLICATIONS

Suranaree University of Technology has approved this thesis submitted in partial fulfillment of the requirements for the Degree of Doctor of Philosophy.

Thesis Examining Committee


(Prof. Dr. James R. Ketudat-Cairns)

Chairperson


(Assoc. Prof. Dr. Rapee Utke)

Member (Thesis Advisor)


(Dr. Claudio Pistidda)

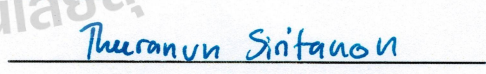
Member (Thesis Co-Advisor)


(Dr. Thi Thu Le)

Member


(Prof. Dr. Jatuporn Wittayakun)

Member


(Assoc. Prof. Dr. Theeranun Siritanon)

Member


(Assoc. Prof. Dr. Chatchai Jothityangkoon)
Vice Rector for Academic Affairs
and Quality Assurance


(Prof. Dr. Santi Maensiri)
Dean of Institute of Science

โสภิตา เทียงวิริยะ : การเพิ่มคุณสมบัติการดูดซับไฮโดรเจนของแมกนีเซียมไฮไดรด์สำหรับการประยุกต์ใช้เป็นแหล่งกักเก็บไฮโดรเจน (ENHANCED HYDROGEN SORPTION PROPERTIES OF MgH_2 -BASED SYSTEMS FOR HYDROGEN STORAGE APPLICATION)
อาจารย์ที่ปรึกษา : รองศาสตราจารย์ ดร.ระพี อุทเคอ, 81 หน้า

คำสำคัญ: การดูดซับไฮโดรเจน/ โลหะไฮไดรด์/ จลพจนศาสตร์/ การซึมผ่านของไฮโดรเจน/คาร์บอน/ การกักเก็บไฮโดรเจน/ โลหะทรานซิชัน/ แมกนีเซียม/ การแทนที่/ การผันกลับได้

การกักเก็บไฮโดรเจนในวัสดุแมกนีเซียม (Mg-based) ยังคงได้รับความสนใจอย่างกว้างขวาง เนื่องจากวัสดุแมกนีเซียมมีข้อดีคือ มีความจุไฮโดรเจน และปริมาตรการกักเก็บสูง (7.6 wt.% H_2 และ $110 \text{ kg } H_2 / \text{m}^3$ ตามลำดับ) มีความเสถียรในการเกิดปฏิกิริยากักเก็บและปลดปล่อยไฮโดรเจน ราคาถูก และมีความต้านทานความร้อน อย่างไรก็ตาม พันธะระหว่างแมกนีเซียมและไฮโดรเจน มีความเสถียรทางความร้อนสูง ส่งผลให้ต้องใช้อุณหภูมิสูงในการทำให้เกิดปฏิกิริยาการปลดปล่อยไฮโดรเจน และอัตราเร็วในการเกิดปฏิกิริยาช้า ดังนั้นการจะปรับปรุงคุณสมบัติการดูดซับไฮโดรเจนของแมกนีเซียมไฮไดรด์ (MgH_2) นั้นได้ถูกศึกษาดังนี้ (i) การคอมโพสิตแมกนีเซียมไฮไดรด์กับลิเทียมโบโรไฮไดรด์ ($LiBH_4$) และ ผสมกับเส้นใยคาร์บอนระดับนาโนเมตร (activated carbon nanofiber, ACNFs) (ii) การเติมโลหะนิกเกิล (Ni) ในระบบ MgH_2/Fe นอกจากนี้ยังได้ศึกษาการเพิ่มขนาดด่างกักเก็บไฮโดรเจนของระบบ MgH_2 ที่เติม TiF_4 และ คาร์บอนนาโนทิวบ์ ($MgH_2-TiF_4-MWCNTs$) จากการศึกษาประสิทธิภาพการกักเก็บไฮโดรเจนของคอมโพสิต $2LiBH_4-MgH_2$ ที่ถูกอัดเป็นเม็ด ทั้งที่เติมและไม่เติม ACNFs พบว่าตัวอย่างที่เติม 30 wt.% ACNFs สามารถเกิดปฏิกิริยาการปลดปล่อยไฮโดรเจนได้ที่อุณหภูมิต่ำกว่าตัวอย่างที่ไม่เติม ACNFs มากถึง $85 \text{ }^\circ\text{C}$ อีกทั้งยังลดพลังงานก่อกัมมันต์ (Activation energy, E_a) ระหว่างปฏิกิริยาปลดปล่อยไฮโดรเจนของ MgH_2 และ $LiBH_4$ นอกจากนี้การคงรูปร่าง ความสามารถในการซึมผ่านของไฮโดรเจน และการนำความร้อน ระหว่างการเกิดปฏิกิริยา ยังได้รับการปรับปรุงหลังเติม ACNFs สำหรับประสิทธิภาพการกักเก็บไฮโดรเจนและกลไกการเกิดปฏิกิริยาของตัวอย่างแมกนีเซียมไฮไดรด์ (Mg_2FeH_6) ทั้งที่เติม (5 และ 20 wt. %) และไม่เติมโลหะนิกเกิลถูกศึกษา พบว่าตัวอย่าง Mg_2FeH_6 เกิดปฏิกิริยาการปลดปล่อยไฮโดรเจนเพียงขั้นตอนเดียวที่อุณหภูมิ $250 \text{ }^\circ\text{C}$ ความจุไฮโดรเจน 5.4 wt.% ส่วนตัวอย่างที่เติมโลหะนิกเกิลเกิดการปลดปล่อยไฮโดรเจน 2 ขั้นตอนที่อุณหภูมิ $170 \text{ }^\circ\text{C}$ และ $220-250 \text{ }^\circ\text{C}$ ซึ่งเป็นปฏิกิริยาการปลดปล่อยไฮโดรเจนของแมกนีเซียมนิกเกิลไฮไดรด์ (Mg_2NiH_4) และ Mg_2FeH_6 ตามลำดับ ความจุไฮโดรเจน 2.83-3.70 wt.% นอกจากนี้ตัวอย่างที่เติม 20 wt.% โลหะนิกเกิล เกิดสารใหม่ขึ้นคือแมกนีเซียมไฮไดรด์นิกเกิลไฮไดรด์ ($Mg_2Fe_{0.75}Ni_{0.25}H_6$) ระหว่างเกิดปฏิกิริยาการปลดปล่อยไฮโดรเจน

ซึ่ง $Mg_2Fe_{0.75}Ni_{0.25}H_6$ ช่วยเพิ่มความเร็วในการดูดซับไฮโดรเจนเมื่อเปรียบเทียบกับตัวอย่าง Mg_2FeH_6 ที่ไม่เติมโลหะนิกเกิล และการศึกษาการเพิ่มขนาดดักเก็บไฮโดรเจนของระบบ MgH_2 ที่เติม TiF_4 และ คาร์บอนนาโนทิวบ์ที่มีระบบแลกเปลี่ยนความร้อน พบว่าตัวอย่างนี้เกิดปฏิกิริยาการปลดปล่อยไฮโดรเจนที่อุณหภูมิต่ำกว่าตัวอย่างที่ไม่ถูกเติม TiF_4 และ MWCNTs จาก $433\text{ }^{\circ}C$ เป็น $388\text{ }^{\circ}C$ ความจุไฮโดรเจน $4.1\text{ wt.}\%$ เกิดปลดปล่อยและปฏิกิริยากักเก็บไฮโดรเจนสมบูรณ์ภายใน $120-150$ และ 25 นาทีตามลำดับซึ่งใช้เวลาสั้นกว่าเมื่อเปรียบเทียบกับงานวิจัยก่อนหน้านี้ และเมื่อทำปฏิกิริยากักเก็บและปลดปล่อยไฮโดรเจนผ่านไป 20 รอบ ได้ความจุไฮโดรเจนเฉลี่ย และความจุไฮโดรเจนเมื่อเทียบกับวัสดุ 5.60 และ $5.40\text{ wt.}\%$ ตามลำดับ โดยไม่มีการรวมตัวกันของอนุภาคตัวอย่าง ดังนั้นการเพิ่มความเร็วในการเกิดปฏิกิริยาและการผันกลับได้ของตัวอย่างนี้ไม่เพียงแต่อธิบายได้โดยผลของตัวเร่งปฏิกิริยา TiF_4 และ MWCNTs แต่ยักรวมถึงผลของระบบแลกเปลี่ยนความร้อนอีกด้วย สำหรับการศึกษาศมรรถนะทางไฟฟ้าของระบบดักเก็บที่ต่อกับ PEMFC พบว่าผลิตกำลังไฟฟ้ารวมได้ 19 Wh



สาขาวิชาเคมี

ปีการศึกษา 2564

ลายมือชื่อนักศึกษา ไฉ่ฉัตร เกียรติวิริยะ

ลายมือชื่ออาจารย์ที่ปรึกษา Uthairat Ratanaporn

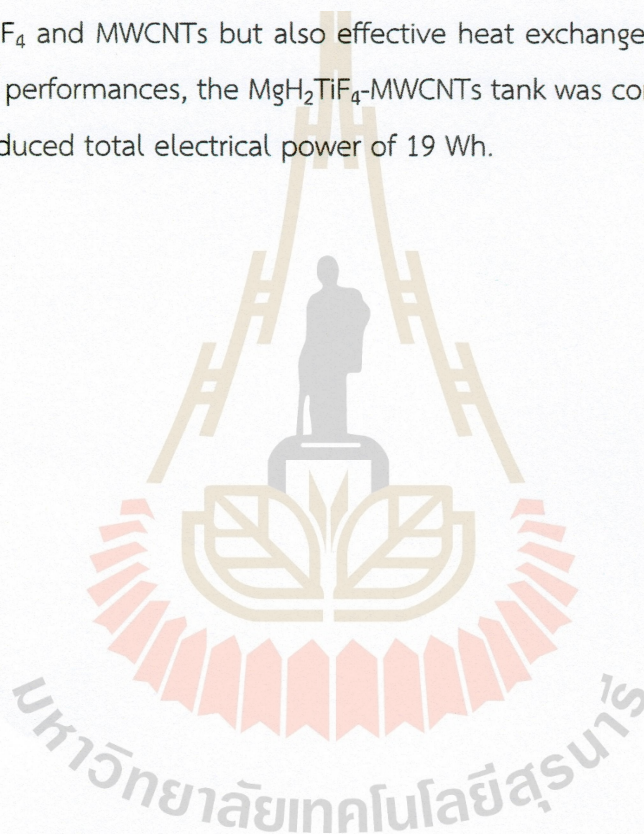
ลายมือชื่ออาจารย์ที่ปรึกษาร่วม Chandana P. P. P.

SOPHIDA THIANGVIRIYA : ENHANCED HYDROGEN SORPTION PROPERTIES OF MgH₂-BASED SYSTEMS FOR HYDROGEN STORAGE APPLICATIONS. THESIS
ADVISOR : ASSOC. PROF. RAPEE UTKE, Ph.D. 81 PP.

Keyword: HYDROGEN SORPTION/ METAL HYDRIDES/ KINETICS/ HYDROGEN PERMEABILITY/ CARBON/ HYDROGEN STORAGE/ TRANSITION METAL/ MAGNESIUM/ SUBSTITUTION/ REVERSIBILITY

Mg-based hydrogen storage materials have been investigated due to their advantages of high gravimetric and volumetric storage capacities (7.6 wt. % H₂ and 110 kg H₂ m⁻³, respectively), good cycling stability, abundance, low cost, and heat resistance. However, the high thermal stability of Mg-H bonds leads to a high dehydrogenation temperature and sluggish kinetics. Therefore, the improvement of hydrogen sorption properties of MgH₂ by (i) compositing with LiBH₄ and doping with activated carbon nanofibers (ii) doping with Ni into MgH₂/Fe were investigated in detail. Moreover, upscaling of MgH₂ doped with TiF₄ and multi-walled carbon nanotubes (MWCNTs) to tank scale was proposed. The hydrogen storage performance of compacted 2LiBH₄-MgH₂ composite with and without activated carbon nanofiber (ACNFs) was studied. The dehydrogenation temperature of compacted 2LiBH₄-MgH₂ with 30 wt.% ACNFs (onset temperature = 275 °C) was significantly lower than that of 2LiBH₄-MgH₂ ($\Delta T=85$ °C) together with reduction of activation energy (E_a) during dehydrogenation of MgH₂ and LiBH₄ after doping with ACNFs. Moreover, the mechanical stability, hydrogen permeability, and thermal conductivity, during cycling were enhanced. The hydrogen storage performance and dehydrogenation pathways of Mg₂FeH₆ with (5 and 20 wt.% Ni) and without Ni were studied. As-prepared Mg₂FeH₆ showed single-step dehydrogenation at 250 °C with hydrogen capacity of 5.4 wt.% H₂. Mg₂FeH₆ with Ni doping showed two-steps dehydrogenation at 170 and 220-250 °C of Mg₂NiH₄ and Mg₂FeH₆, respectively, with storage capacity of 2.83-3.70 wt.% H₂. Moreover, 20 wt.% Ni exhibited a new phase of Mg₂Fe_{0.75}Ni_{0.25}H₆ during dehydrogenation. Mg₂Fe_{0.75}Ni_{0.25}H₆ had improved hydrogen sorption kinetics compared to Mg₂FeH₆, together with the improved kinetics and cycling stability. MgH₂-TiF₄-MWCNT

based tank with heat exchanger system was studied. The dehydrogenation temperature of $\text{MgH}_2\text{-TiF}_4\text{-MWCNT}$ was reduced from 433 to 388 °C with hydrogen capacity of 4.1 wt.%. De/rehydrogenation was done within 120-150 and 25 min, respectively, which were a shorter time compared with the previous work. Upon the 20th cycling, the average capacity and material capacity were 5.60 and 5.40 wt.% H_2 , respectively, with no particle agglomeration. Thus, the enhanced kinetics and reversibility of the $\text{MH-TiF}_4\text{-MWCNT}$ -based tank was explained by not only catalytic effects of TiF_4 and MWCNTs but also effective heat exchanger system. For the study of electrical performances, the $\text{MgH}_2\text{-TiF}_4\text{-MWCNTs}$ tank was combined with the PEMFC stack. It produced total electrical power of 19 Wh.



School of Chemistry
Academic Year 2021

Student's Signature Sophida Thiangviriya
Advisor's Signature Uthairat Ratanaprasit
Co-advisor's Signature Claudia P. Middle

ACKNOWLEDGEMENTS

This work would have never been accomplished without the contribution of many people. Firstly, I would like to thank my supervisor, Assoc. Prof. Dr. Rapee Utke for her expert guidance, support, discussions, encouragement, putting up with my moaning in many years and always believing in me over the course of my thesis.

I also would like to thank my co-supervisor, Dr. Claudio Pistidda from Institute of Hydrogen Technology, Helmholtz-Zentrum Hereon GmbH, Geestacht, Germany for his great help and support. Other members from his group, such as Dr. Thi Thu Le, Dr. Gökhan Gizer, Yuanyuan Shang, and Annbritt Hagenah are also gratefully acknowledged for valuable help with the experimental work and kindly suggestion during my visits to Helmholtz-Zentrum Hereon GmbH.

I wish to gratefully acknowledge the financial support I have received from The Royal Golden Jubilee (RGJ) Ph.D. program, Thailand (PHD/0153/2558) which enable me to continue my study after my master degree.

Also, I would like to thank all members of the Hydrogen Storage Material Lab and Solid-state Chemistry at SUT for their help, fulfill, discussions and friendship. I would like to thank The Synchrotron Light Research Institute (Public Organization), Nakhon Ratchasima, Thailand and the people from Mechanical work shop at Facility Building 1 (F1) SUT, especially Mr. Nasart Boonyada for characterization equipment.

Finally, I would also like to thank my parents for their encouragement and moral support in every step of my academic career.

Sophida Thiangviriya

CONTENTS

	Page
ABSTRACT IN THAI.....	I
ABSTRACT IN ENGLISH.....	III
ACKNOWLEDGEMENTS	V
CONTENTS.....	VI
LIST OF TABLES	VII
LIST OF FIGURES	VIII
CHAPTER	
I INTRODUCTION.....	1
1.1 Hydrogen energy.....	1
1.2 Hydrogen storage methods and applications.....	2
1.3 References.....	6
II LITERATURE REVIEW	8
2.1 Hydrogen in metal hydrides.....	8
2.2 Properties of magnesium hydride and their tuning strategies	11
2.3 References.....	22
III EXPERIMENTAL SECTION	28
3.1 Chemicals.....	28
3.2 Apparatus	28
3.2.1 Glove box.....	28
3.2.2 High energy ball milling	29
3.2.3 Autoclave	31
3.3 Preparation of compacted $2\text{LiBH}_4\text{-MgH}_2\text{-ACNFs}$	31
3.4 Synthesis of Ni-doped Mg_2FeH_6	32
3.5 Up scaling of $\text{MgH}_2\text{-TiF}_4\text{-MWCTs}$ to tank scale.....	32
3.6 Characterizations	34
3.6.1 Chemical compositions and structure	34

CONTENTS (Continued)

	Page
3.6.1.1 Powder X-ray diffraction (PXD).....	34
3.6.1.2 In situ synchrotron radiation powder X-ray diffraction (SR-PXD).....	34
3.6.1.3 X-ray absorption spectroscopy (XAS)	35
3.6.1.4 Fourier Transform Infrared Spectrometry (FTIR).....	36
3.6.2 Hydrogen sorption properties.....	37
3.6.2.1 Simultaneous Thermal Analysis (STA) coupled with Mass Spectroscopy (MS)	37
3.6.2.2 Differential scanning calorimetry (DSC)	37
3.6.2.3 Sievert-type apparatus in laboratory scale.....	38
3.6.2.4 Sievert's type apparatus in tank scale	40
3.6.3 Integration of PEMFC stack and hydrogen storage tank.....	41
3.6.4 Hydrogen diffusion and thermal conductivity properties.....	42
3.6.4.1 Hydrogen permeability	42
3.6.4.2 Thermal conductivity	43
3.7 References.....	44
IV RESULTS AND DISCUSSION	46
4.1 Compacted $2\text{LiBH}_4\text{-MgH}_2\text{-ACNF}$	46
4.2 Ni-doped Mg_2FeH_6	56
4.3 $\text{MgH}_2\text{-TiF}_4\text{-MWCNT}$ hydrogen storage tank.....	67
4.4 References.....	74
V CONCLUSIONS	79
CURRICULUM VITAE.....	81

LIST OF TABLES

Table	Page
1.1	Materials-based automotive hydrogen storage systems compared to the 2020 and ultimate targets set by the US-DOE 3
1.2	The comparison of specification and performance of different fuel cars..... 4
3.1	Chemicals used in this work..... 28
4.1	Photographs, thickness, and density of 2Li-MH and 2Li-MH-30% ACNF in as-prepared and rehydrogenated states 49
4.2	Thermal conductivity, thermal diffusivity, and specific heat capacity of compacted 2Li-MH and 2Li-MH-30% ACNF 55
4.3	Phase compositions and quantities in as-prepared samples were determined by Rietveld refinement 58
4.4	Scattering paths, coordination number, the path range (R), the mean squared displacement (σ^2) and R -factor extracted from the fitted data for Ni atoms substituted in Mg_2FeH_6 of 20%Ni-Mg-Fe 65
4.5	Specification of PEMFC stack supplying hydrogen from MH-TiF ₄ -MCNT tank..... 74

LIST OF FIGURES

Figure	Page
1.1 World historical and projected primary energy consumption from 1970 to 2050.....	1
1.2 The global surface air temperature anomalies.....	2
1.3 Physical- and material-based methods to store hydrogen.....	5
2.1 Interaction of hydrogen with material in various steps.....	8
2.2 Pressure-composition isotherm plot of metal-to-metal hydride phase transition.....	10
2.3 Activation energy (E_a) and enthalpy (ΔH) diagram.....	11
2.4 Crystal structures of five MgH_2 phases crystallite size.....	12
2.5 The changes in decomposition temperature for MgH_2 vs. crystallite size.....	13
2.6 TDS spectra of the $xMgH_2@CT$ composites.....	14
2.7 Thermal desorption mass spectra (TDMS) of hydrogen for milled- MgH_2 and MgH_2 doped with 1 mol % Cu^{nano} , Fe^{nano} , Co^{nano} , and Ni^{nano}	15
2.8 Temperature programmed desorption during dehydrogenation of all as-prepared samples.....	16
2.9 Experimental evolutions of temperature, pressure, and hydrogen volume during dehydrogenation at 340 °C under 0.1 MPa.....	17
2.10 Axial and radial permeabilities of MgH_2 disks versus ENG content.....	18
2.11 Thermodynamics of $LiBH_4/MgH_2$ composite as an example of evolution of the ΔH and ΔS as a function of the reaction paths.....	19
2.12 Schematic showing the formation procedures of the $Mg_2Fe(Ni)H_6$	21
2.13 DSC curves during desorption of the $Mg-Fe-H$ and $Mg-Fe(Ni)-H$	22
3.1 Glove box.....	29
3.2 Different types of ball mill.....	29
3.3 Autoclave.....	31
3.4 The components of hydrogen storage tank.....	33

LIST OF FIGURES (Continued)

Figure	Page
3.5 An airtight sample holder for PXD experiments.....	34
3.6 In situ SR-PXD sample cell.....	35
3.7 The set-up at BL5.2 SUT-NANOTEC-SLRI XAS beamline at SLRI, Thailand	36
3.8 FTIR spectrometer of Tensor 27-Hyperion 2000	36
3.9 STA 449 F3 Jupiter coupled with QMS 403C	37
3.10 Photo and schematic diagram of Sievert-type apparatus.....	38
3.11 Sievert's type apparatus (HERA, Quebec, Canada).....	39
3.12 Photo and schematic diagram of Sievert-type apparatus in tank scale.....	41
3.13 The measurement setup of electrical performances of integrated PEMFC-H ₂ tank system.....	42
3.14 Schematic diagram of hydrogen permeability setup	43
4.1 Simultaneous STA-MS results during dehydrogenation of 2Li-MH and 2Li-MH-30% ACNF.....	47
4.2 Dehydrogenation kinetics and reversibility of 2LiMH and 2Li-MH -30% ACNF.....	48
4.3 PXD and FTIR spectra of as-prepared, dehydrogenated, and rehydrogenated pellets of 2Li-MH.	50
4.4 PXD and FTIR spectra of as-prepared, dehydrogenated, and rehydrogenated of 2Li-MH-30%ACNF	51
4.5 DSC curves with heating rates of 5-20 °C/min and the Kissinger plots of 2Li-MH and 2Li-MH-30%ACNF.....	53
4.6 Pu and Pd versus time and hydrogen permeability of 2Li-MH and 2Li-MH-30%ACNF.....	54
4.7 Rietveld refinement of SR-PXD results of as-prepared Mg ₂ FeH ₆ , 5%Ni-Mg-Fe, and 20%Ni-Mg-Fe.....	67
4.8 First hydrogen desorption kinetics at 330 °C under 10 kPa of pure Mg-Fe, 5%Ni-Mg-Fe, and 20%Ni-Mg-Fe.....	59

LIST OF FIGURES (Continued)

Figure	Page
4.9 In situ SR-XRD spectra of as-prepared Mg_2FeH_6 and peak intensities versus temperature.	60
4.10 In situ SR-XRD spectra of 5%Ni-Mg-Fe and peak intensities versus temperature.	61
4.11 In situ SR-XRD spectra of 20%Ni-Mg-Fe and peak intensities versus temperature.	62
4.12 Ni K-edge EXAFS data and model fitting in k-space and R-space, and Ni K-edge XANES spectrum of $Mg_2Fe_{0.75}Ni_{0.25}$	64
4.13 Dehydrogenation kinetics and reversibility under vacuum at 330 °C of Mg_2FeH_6 , 5%Ni-Mg-Fe, and 20%Ni-Mg-Fe.....	66
4.14 PXD and STA-MS results of as-prepared MH-TiF ₄ -MWCNT	68
4.15 Dehydrogenation of MH-TiF ₄ -MWCNT based tank at isothermal condition and the positions of thermocouples (TCs) located in the axial and radial directions of the tank.....	69
4.16 Hydrogenation of MH-TiF ₄ -MWCNT based tank at isothermal condition.	70
4.17 Cycling stability upon 20 de/rehydrogenation cycles of MH-TiF ₄ -MWCNT based tank.	71
4.18 PXD spectrum and physical appearance of MH-TiF ₄ -MWCNT after the 20 th hydrogenation	72
4.19 Polarization curve and electrical performance of PEMFC stack supplied with hydrogen gas from MH-TiF ₄ -MWCNT tank.....	73

CHAPTER I

INTRODUCTION

1.1 Hydrogen energy

Demand for clean and environmentally friendly energy resources has been enhanced due to the awareness of increasing worldwide energy consumption and pollution. From Figure 1.1, world primary energy consumption is projected to peak in 2035 and fossil fuels are most consumed. However, the use of fossil fuels will not last for longer than a few decades due to the limitation of crude oil resources (Shafiee et al, 2009).

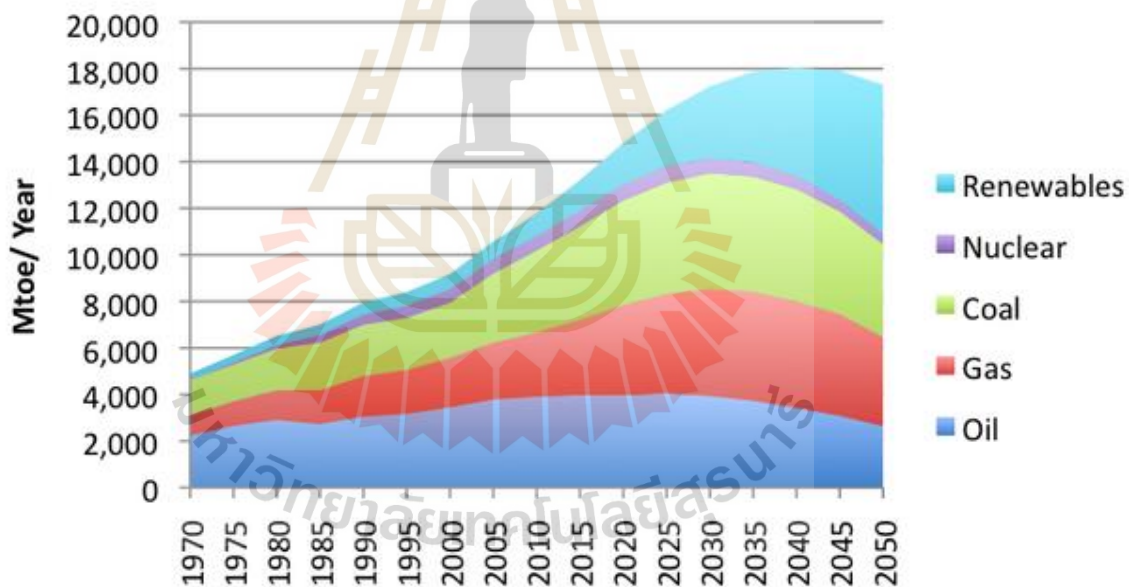


Figure 1.1 World historical and projected primary energy consumption from 1970 to 2050 (Randers, 2013).

Moreover, the consumption of fossil fuel also generates pollutants and carbon dioxide (CO_2), leading to global warming and climate change. For example, in June 2021, the global surface temperature was 0.88°C , which is warmer than the average value in 1991-2020 (0.21°C) and the fifth-highest for in the 142-year period (Figure 1.2). (C3S., 2021, NCEI, 2021, and CHANGE, 2021).

**Global Land and Ocean
May Temperature Anomalies**

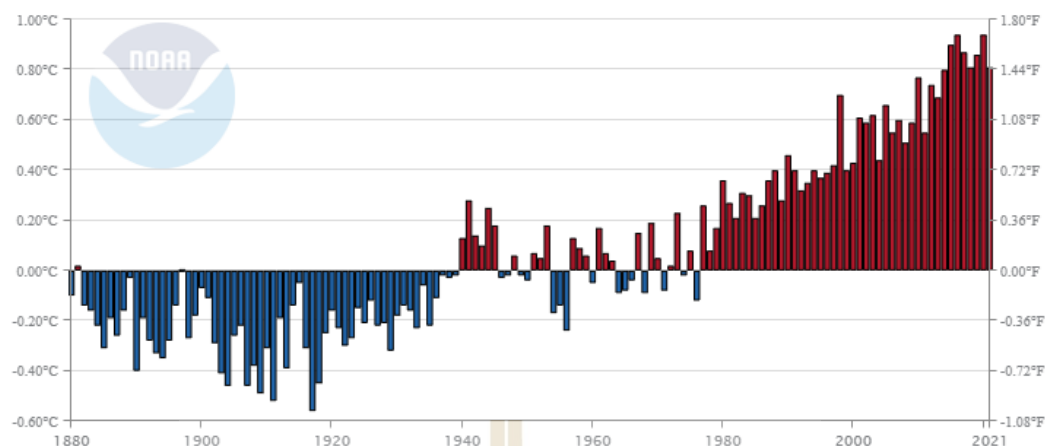


Figure 1.2 The global surface air temperature anomalies (NCEI, 2021).

Thus, many scientists are looking for alternative renewable resources to reduce the overall dependency on fossil fuels. Extensive research has recently been carried out on renewable energy sources, such as hydrogen, solar, wind, nuclear, tidal, hydro, biofuels, and geothermal energy. Hydrogen has drawn a lot of attention due to its high energy density per unit mass of 120 MJ/kg (~three and seven times greater than gasoline and coal, respectively), cleanness, and abundance, and various production methods.

1.2 Hydrogen storage methods and applications

To use hydrogen energy effectively, one of the most important components is an effective hydrogen storage system with high volumetric and gravimetric capacities (30 gH₂/L and 45 gH₂/kg, respectively) and moderate operating temperatures and pressures (-40 to 85 °C and 5-12 bar H₂) as targeted by the US-DOE for 2025 (Table 1.1) (Partnership, 2017). These targets are still challenging to achieve, and no existing material can well satisfy them.

Table 1.1 Materials-based automotive hydrogen storage systems compared to the 2020 and ultimate targets set by the US-DOE (US-DOE, 2017).

Storage System Targets	Gravimetric Density (kg H ₂ /kg system)	Volumetric Density (kg H ₂ /L system)	Temperature (°C)	Pressure (bar H ₂)
2025	0.055	0.040	-40-85	5-12
Ultimate	65	50	-40-85	5-12

Current Status	Gravimetric Density (kg H ₂ /kg system)	Volumetric Density (kg H ₂ /L system)	Temperature (°C)	Pressure (bar H ₂)
Metal Hydride (MH): NaAlH ₄	12	12	125	0.2-10
Sorbent: MOF-5	38	21	-193	100
Chemical Hydrogen (CH)	46	40	-	-
Storage: Off-Board Regenerable (AB)				

As an energy source, hydrogen can be used for different purposes including portable electronics, transportation, and stationary applications. However, several projects focus on personal vehicles, (Hao and Sarkis, 2016) eliminating carbon dioxide and others air pollution to the environment. Hydrogen is environmentally friendly since it can generate energy by converting the chemical free energy of hydrogen into electrical energy via a fuel cell. The most suitable type of fuel cells for mobile application is the polymer electrolyte membrane fuel cells (PEMFCs) owing to low operating temperatures about 80 °C (Sharaf and Orhan, 2014), high power density, rapid change in power on demand, and quick start up. Recently, the hydrogen fuel cell car is successfully developed by Toyota (Mirai) (TOYOTA, 2020), Mercedes Benz (GLC F-Cell) (Mercedes-Benz, 2021), Hyundai (Nexo) (HYUNDAI, 2018), and Honda (Clarity) (HONDA, 2017).

Table 1.2 The comparison of specification and performance of different fuel cars are listed in

Properties	Toyota Mirai	Mercedes Benz GLC F-Cell	Hyundai Nexo	Honda Clarity
Max. Power /kW	114	155	120	130
Max. Speed/kmh ¹	178	160	179	165
Battery	Ni-metal hydride	Li-ion	Li-ion	Li-ion
Tank volume /L	122.4	-	156	141.0
H ₂ storage/kg	5.00	4.40	6.33	5.00
Fuel tank pressure MPa	70	70	70	70
Refueling time/min	5	3	5	3
Rang/km	480	328	756	650

Hydrogen can be stored mainly by physical- and material-based methods (Figure 1.3). For the physical-based method, hydrogen stored in the forms of compressed gas (350-700 bar H₂ at room temperature) and liquefied hydrogen (at a cryogenic temperature of -253 °C) provide storage capacities of 40 and 71 gH₂/L, respectively (Ren et al., 2017). Due to severe storage pressure and temperature conditions of physical-based methods, not only safety issue is concerned but also the cost of fabrication for storage tanks with high tensile strength (compressed gas) and superior insulator (liquefied H₂). Alternatively, materials-based methods of chemical absorption in either solid-state hydrides (metal, complex, and composite hydrides) or liquid organic hydrogen as well as physical adsorption in porous materials with high surface area through van der Waals interaction, have been significantly interested (Ren et al., 2017). Among these materials-based methods, solid-state hydrides are promising for hydrogen storage applications due to their high volumetric and gravimetric hydrogen capacities (70-150 gH₂/L and 2-25 wt.% H₂, respectively) (Ren et al., 2017). Moreover, since hydride materials are claimed to store hydrogen in high purity, they can be used directly to supply hydrogen to fuel cells without a purification system. However, solid-state

hydrides still have some obstacles based on their severe operating temperature and pressure conditions, slow hydrogen sorption kinetics (rehydrogenation of LiBH_4 at ~ 600 °C under 155 bar H_2 for >12 h) (He et al., 2019), and release of toxic gases during operation (e.g., B_2H_6 from LiBH_4) (Yan et al., 2012).

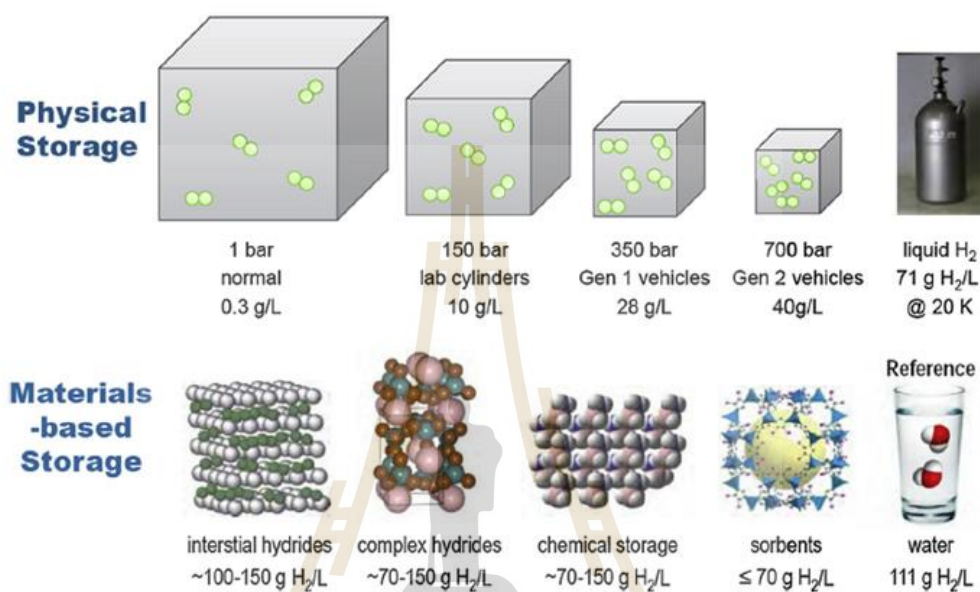


Figure 1.3 Physical- and material-based methods to store hydrogen (Ren et al., 2017).

In this work, we aim to approach the 2025 targets set by US-DOE, especially gravimetric and volumetric capacities of 5.5 wt.% H_2 and 30 gH_2/L , respectively, as well as reduction of operating temperatures and pressures (-40 to 85 °C and 5-12 bar H_2 for absorption) (US-DOE, 2017). Among hydride-based hydrogen storage materials, magnesium hydride (MgH_2) is one of the most promising candidates due to high gravimetric and volumetric storage capacities (7.6 wt.% H_2 and $110 \text{ kg H}_2 \text{ m}^{-3}$, respectively), good cycling stability, abundance, low cost, and heat resistance (Zhang et al., 2020). In addition, MgH_2 has the highest energy density (9 MJ/kg Mg) among all reversibility hydrides for hydrogen storage application (Jain et al., 2010). We would like to improve hydrogen sorption properties of MgH_2 by (i) compositing with LiBH_4 and doping with activated carbon nanofibers (ACNFs) (ii) doping with Ni into MgH_2/Fe system. Moreover, upscaling of MgH_2 doped with TiF_4 and multi-walled carbon nanotubes (MWCNTs) to tank scale is proposed. The goal of this study is to improve

hydrogen sorption kinetics and reversibility of MgH_2 -based hydrogen storage in both laboratory powder and tank scale.

1.3 References

- The Copernicus Climate Change Service (C3S). (2021). Surface air temperature for June 2021. [On-line]. Available: <https://climate.copernicus.eu/surface-air-temperature-june-2021>.
- CHANGE, N. G. C. (2021). NASA's AIRS Tracks Record-Breaking Heat Wave in Pacific Northwest. [On-line]. Available: <https://climate.nasa.gov/news/3095/nasas-airstracks-record-breaking-heat-wave-in-pacific-northwest/>.
- Hao, H., Geng, Y., and Sarkis, J. (2016). Carbon footprint of global passenger cars: Scenarios through 2050. *Energy*, *101*, 121-131. doi:10.1016/j.energy. 2016.01.089.
- He, Q., Zhu, D., Wu, X., Dong, D., Jiang, X., and Xu, M. (2019). The dehydrogenation mechanism and reversibility of LiBH_4 doped by active Al^* derived from AlH_3 . *Metals*, *9*, 559. doi:10.20944/preprints201904.0158.v1.
- HONDA. (2017). Honda Clarity Fuel Cell 2017-Press Kit. [On-line]. Available: <https://hondanews.eu/at/de/cars/media/pressreleases/107266/honda-clarity-fuel-cel2017-pressemappe>.
- HYUNDAI. (2018). Hyundai NEXO press kit. [On-line]. Available: <http://www.hyundai.news/eu/models/electrified/nexo/press-kit.html>.
- Jain, I. P., Lal, C., and Jain, A. (2010). Hydrogen storage in Mg: A most promising material. *International Journal of Hydrogen Energy*, *35*(10), 5133-5144. doi:10.1016/j.ijhydene.2009.08.088.
- Mercedes-Benz. (2021). Mercedes-Benz GLC F-CELL. [On-line]. Available: <https://www.mercedes-benz.de/passengercars/mercedes-benz-cars/models/glc/glc-f-cel/deer-neue-glc-f-cell/stage.module.html>.
- NCEI, N. (2021). Global Climate Report-June 2021. [On-line]. Available: <https://www.ncdc.noaa.gov/sotc/global/202106>.

- Partnership, U. S. D. (2017). Target Explanation Document: Onboard Hydrogen Storage for Light-Duty Fuel Cell Vehicles. [On-line]. Available: https://www.energy.gov/sites/prod/files/2017/05/f34/fcto_targets_onboard_hydro_storage_explanation.pdf.
- Randers, J. (2013). Energy Consumption to 2050, Peak oil news and message boards. [On-line]. Available: <http://peakoilbarrel.com/world-energy-2014-2050-part-3/>.
- Ren, J., Musyoka, N. M., Langmi, H. W., Mathe, M., and Liao, S. (2017). Current research trends and perspectives on materials-based hydrogen storage solutions: A critical review. *International Journal of Hydrogen Energy*, 42(1), 289-311. doi:10.1016/j.ijhydene.2016.11.195.
- Shafiee, S., and Topal, E. (2009). When will fossil fuel reserves be diminished. *Energy Policy*, 37(1), 181-189. doi:10.1016/j.enpol.2008.08.016.
- Sharaf, O. Z., and Orhan, M. F. (2014). An overview of fuel cell technology: Fundamentals and applications. *Renewable and Sustainable Energy Reviews*, 32, 810-853. doi:10.1016/j.rser.2014.01.012.
- TOYOTA. (2020). The toyota mirai. [On-line]. Available: <https://www.toyota-europe.com/world-of-toyota/feel/environment/better-air/fuel-cell-vehicle>.
- Yan, Y., Remhof, A., Hwang, S. J., Li, H. W., Mauron, P., Orimo, S., and Zuttel, A. (2012). Pressure and temperature dependence of the decomposition pathway of LiBH_4 . *Physical Chemistry Chemical Physics*, 14(18), 6514-6519. doi:10.1039/c2cp40131b.
- Zhang, X. L., Liu, Y. F., Zhang, X., Hu, J. J., Gao, M. X., and Pan, H. G. (2020). Empowering hydrogen storage performance of MgH_2 by nanoengineering and nanocatalysis. *Materials Today Nano*, 9. doi:10.1016/j.mtnano.2019.100064.

CHAPTER II

LITERATURE REVIEW

2.1 Hydrogen storage in metal hydrides

Generally, mechanisms to store hydrogen in the form of solid-state hydrides include physical adsorption of hydrogen molecule (van der Waals forces), dissociation of H_2 , chemisorption, and penetration of H atoms. Activation energy barrier has to be crossed for the chemisorption to take place. Afterward, hydrogen diffusion as well as nucleation and growth of hydride, proceed. This is accompanied by the phase transformation (α to β), resulting in change in crystal structure or lattice parameters. A typical sequence of steps during hydrogen adsorption in metal hydride is provided in Figure 2.2 (Gupta et al., 2021).

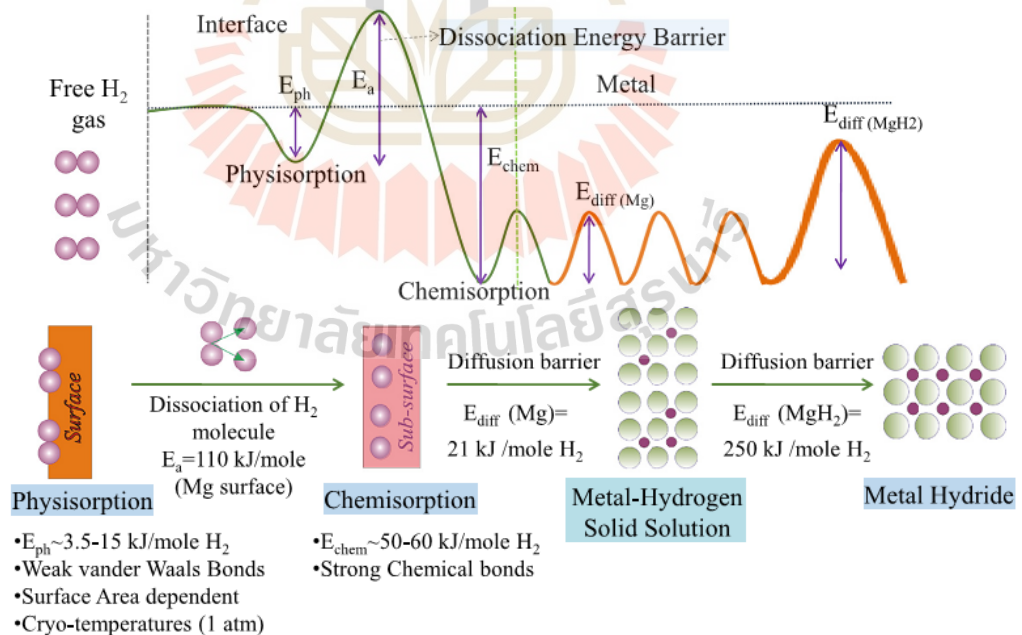


Figure 2.1 Interaction of hydrogen with material including steps (i) physisorption, (ii) chemisorption, (iii) solid solution, and (iv) compound formation (Broom, 2011).

From the thermodynamic point of view, it is examined through pressure-composition isotherms (PCT) (Figure 2.2) (Bardhan et al., 2011). The PCT curve shows the correlation of the equilibrium pressure and the hydrogen content at a given temperature. At low pressures, a solid solution is formed between the metal and hydrogen (α -phase), then nucleation and growth of the metal hydride initiate (β -phase). The two phases coexist and the amount of β -phase increases rapidly with further uptake of hydrogen at constant pressure. This is revealed as the plateau region in the PCT plot. The length of the plateau determines the practical amount of hydrogen stored. As the content of the β -phase reaches saturation point, the pressure starts to increase significantly. The equilibrium pressure (P_{eq}) as a function of temperature is related to the changes of enthalpy (ΔH) and entropy (ΔS) as explained by the Van't Hoff equation (equation (2.1)).

$$\ln(P_{eq}/P_0) = \Delta H/RT - \Delta S/R \quad (2.1)$$

where P_{eq} is the plateau pressure, T is the temperature, P_0 is the reference pressure (1 bar), R is the gas constant ($R = 8.314 \text{ J/mol.K}$), ΔH and ΔS are the enthalpy and entropy changes during the $\alpha \rightarrow \beta$ transformation, respectively.

For practical applications, the pressure at which this transition takes place is close to 1 bar at a relatively low temperature ($\sim 100 \text{ }^\circ\text{C}$). Assuming that ΔS is the entropy of gaseous hydrogen ($130 \text{ J mol}^{-1}\text{K}^{-1}$), the enthalpy of formation of the hydride (ΔH) should be between -30 and -55 kJmol^{-1} to achieve $P_{eq} = 1 \text{ bar H}_2$ $40\text{-}150 \text{ }^\circ\text{C}$ (Züttler, 2008). Unfortunately, none of the hydrides with sufficiently high hydrogen capacity has the desired thermodynamic properties.

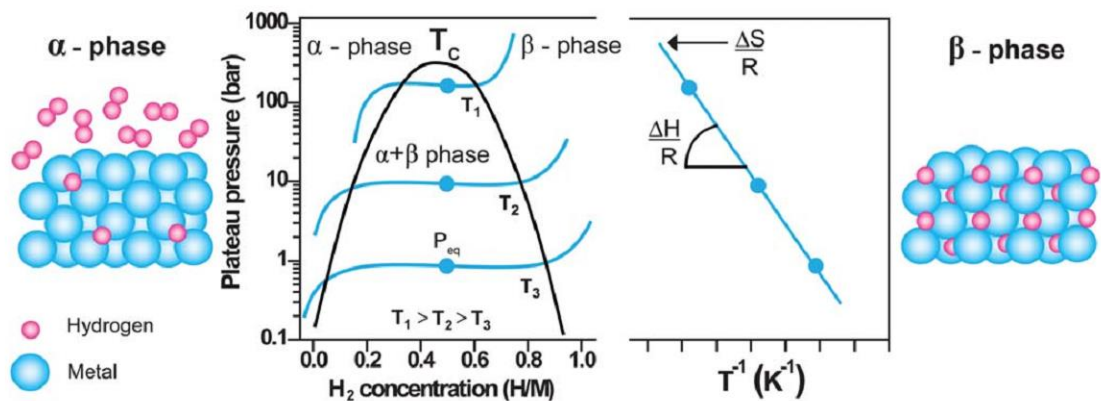


Figure 2.2 Pressure-composition isotherm plot of metal-to-metal hydride (α to β) phase transition (left) and Van't Hoff plot related to the phase transition (right) (Bardhan et al., 2011).

Not only thermodynamics but also the slow sorption kinetics is an obstacle to practical application for metal hydrides. A metal hydrogen system is required to rapidly absorb and desorb hydrogen at moderate temperature. The rate of many chemical reactions is dominated by the presence of activation barriers in the reaction pathway. The H_2 absorption and desorption of many hydrides are chemical reactions, which show significantly high activation barriers. Figure 2.3 shows a typical activation barrier for a generic system, where the activation energy (E_a) quantifies the value of the barrier and shows the effect of catalyst on the system. Although, the catalyst has no effect on the thermodynamics of the system as the nature of the reactants and products is unchanged, it favors E_a reduction (Züttle et al., 2008).

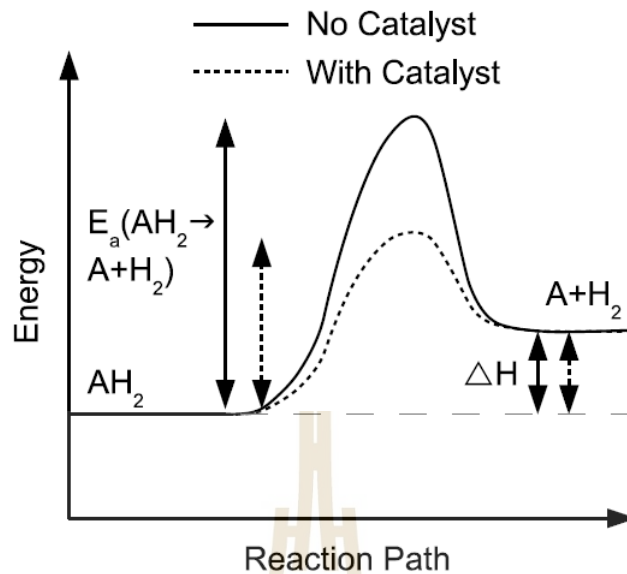


Figure 2.3 Activation energy (E_a) and enthalpy (ΔH) diagram of de/rehydrogenation reaction $AH_2 \leftrightarrow A + H_2$.

Kissinger analysis can be employed to measure the E_a of the reaction using the results from differential scanning calorimetry (DSC), decrised in equation (2.2)

$$\ln(\beta/T_p^2) = -E_a/RT_p + \ln(k_0) \quad (2.2)$$

where β is the heating rate ($^{\circ}C/min$), T_p is the peak temperature of desorption, R is the gas constant ($8.314 \text{ j mol}^{-1} \text{ K}^{-1}$), E_a is the activation energy, and k_0 is a constant. The activation energy is calculated from the slope of $\ln(\beta/T_p^2)$ versus $1/T_p$ plot (Züttle, 2008).

2.2 Properties of magnesium hydride and their tuning strategies

Among all the hydride materials, magnesium hydride (MgH_2) has attracted particular attention because of its high gravimetric and volumetric capacities (7.6 wt% H_2 and 110 gH_2/L , respectively), low cost, and natural abundance (Jain et al., 2010 and Crivello et al., 2016). MgH_2 is an ionic compound of an alkaline earth metal (Mg) and hydride (H^-). At ambient condition, MgH_2 has α - MgH_2 rutile structure (space group P42/mnm) and transforms to γ , δ , ϵ , and ζ when pressures increase to 5, 10, 100, and 180 GPa, respectively (Figure 2.4) (Zhang et al., 2017).

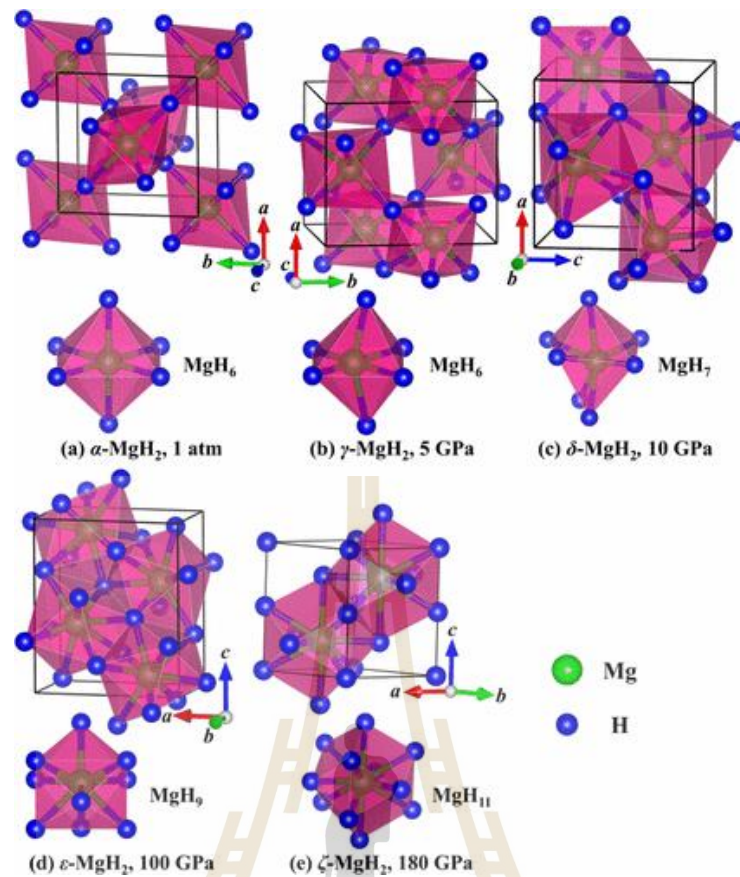


Figure 2.4 Crystal structures of α -MgH₂ at 1 atm (a), γ -MgH₂ at 5 GPa (b), δ -MgH₂ at 10 GPa (c), ϵ -MgH₂ at 100 GPa (d), and ζ -MgH₂ at 180 GPa (e) (Zhang et al., 2017).

Although Mg/MgH₂ is attractive for storing hydrogen, high dehydrogenation temperature ($T > 400$ °C), slow sorption kinetics, and rapid oxidation with oxygen in air prohibit its practical use in fuel cells (El-Eskandarany et al., 2017). Several approaches have been proposed to improve the hydrogen storage properties of MgH₂, such as particle size reduction (ball milling and nanoconfinement) (Czujko et al., 2020 and Ma et al., 2021), addition of catalysts and additives (Sun et al., 2020 and Wang et al., 2021), reactive hydride composites (Cho et al., 2016), and alloying with other metals (Sun et al., 2020). The first approach of Mg/MgH₂ particle size reduction using mechanical ball milling technique with different parameters (e.g., ball-to-powder weight ratio, milling time, and speed) is the most common method to increase the contact surface and decrease the diffusion distance of hydrogen for significant improvement in sorption kinetics. Rahmaninasab et al. (2018) studied the effects of ball milling times (10, 30, and 40 h) on the hydrogen desorption properties of MgH₂. By increasing milling time up to 40 h, the onset desorption temperature of MgH₂

decreased by 80 °C as compared with as-received MgH_2 (Rahmaninasab et al., 2018). Next, Czujko et al. (2020) found that dehydrogenation temperature of MgH_2 reduced almost linearly with the size of crystallites (Figure 2.5) (Czujko et al., 2020).

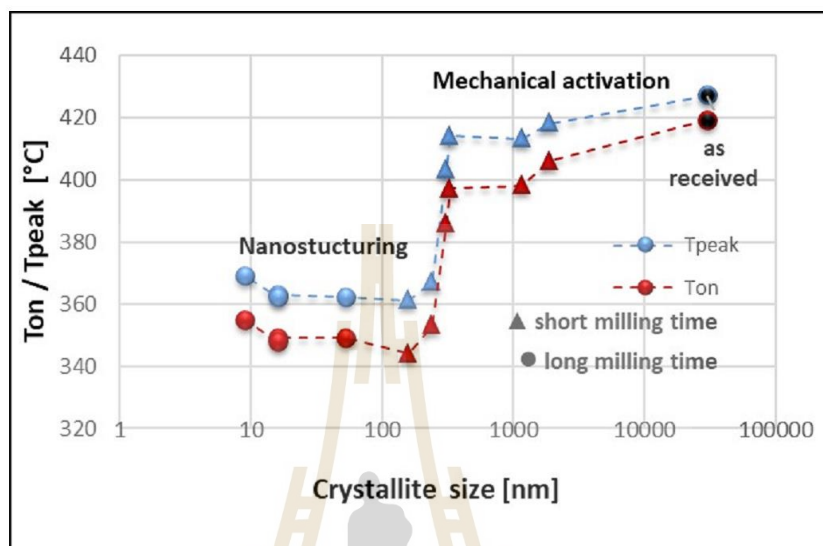


Figure 2.5 The changes in decomposition temperature for MgH_2 versus crystallite size (Czujko et al., 2020).

Next approach is the nanoconfinement of MgH_2 into nanoporous materials with high surface area and porosity. Nanoconfined MgH_2 showed greatly enhanced desorption properties, good cyclic stability, and preventing agglomeration during cycling. For example, MgH_2 was confined into nanoporous resorcinol-formaldehyde carbon aerogels prepared by solution impregnation of dibutyl magnesium (MgBu_2) precursor solution and hydrogenation. Two carbon aerogel scaffolds with pore volumes of 1.27 and 0.65 mL/g and average pore sizes of 22 and 7 nm were studied. It was found that the smaller the pores size, the faster the dehydrogenation rate. This was possibly due to the particle size reduction of MgH_2 after nanoconfinement, leading to high reactive surface area and kinetic improvement. Furthermore, ultra-small MgH_2 nanoparticles embedded in an ordered microporous carbon (15, 25, and 50 wt. % MgH_2 denoted as 15 MgH_2 @CT, 25 MgH_2 @CT, and 50 MgH_2 @CT, respectively) was prepared by solution impregnation using MgBu_2 precursor solution (Zlotea et al., 2015). The more the MgH_2 loading content, the bigger the particle size. For example, the average particle sizes of

15MgH₂@CT, 25MgH₂@CT, and 50MgH₂@CT were 1.3, 3.0, and 4-10 nm, respectively. Thermal desorption spectroscopy (TDS) showed that bulk MgH₂ started to desorb hydrogen at 635 K, while nanoconfined samples of 15MgH₂@CT, 25MgH₂@CT, and 50MgH₂@CT started at 390, 390, and 525 K, respectively (Figure 2.6). Improved desorption kinetics was due to the shorter diffusion length of hydrogen within nanoparticles.

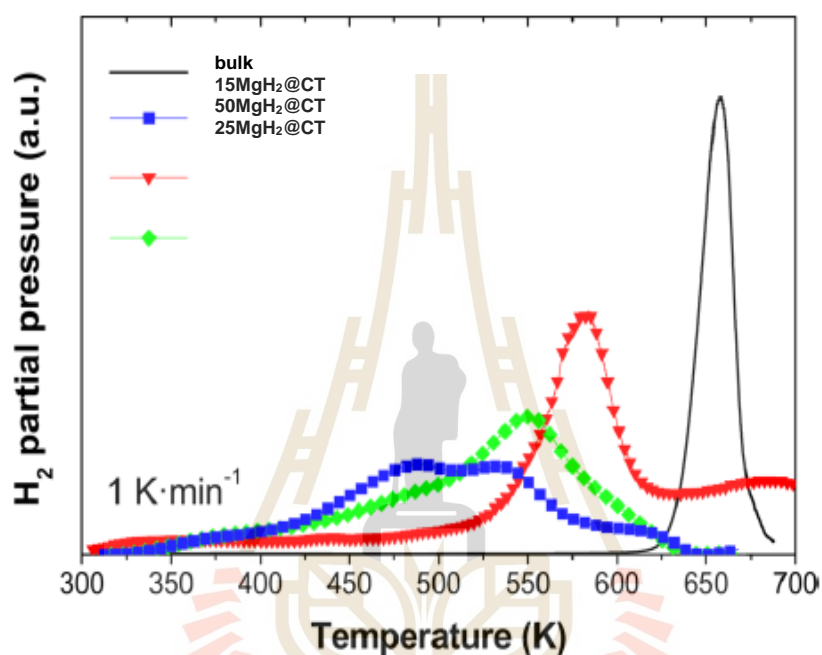


Figure 2.6 TDS spectra of the xMgH₂@CT composites with x = 15, 25, and 50 wt.% Mg and bulk MgH₂ recorded at a heating rate of 1 K·min⁻¹ (Zlotea et al., 2015).

Another strategy to enhance the properties of MgH₂ is catalytic doping to improve the hydrogen sorption kinetics of MgH₂. In addition, catalysts generally act as activation agents to form trapping centers or intermediate metastable states, reducing the reaction barriers (West et al., 2013) and accelerating reaction rate (Gaboardi et al., 2014). For instance, Nobuko et al. (2005) examined the catalytic effects of 3d-transition metals (Fe ^{nano}, Co ^{nano}, Ni ^{nano}, and Cu ^{nano}) on hydrogen desorption properties of MgH₂ (Figure 2.7). In particular, 1 mol % Ni ^{nano}-doped MgH₂ prepared by ball milling (2h) shows the best hydrogen desorption properties, for example, the desorption peak temperature (260 °C) was about 100 °C lower than that of milled MgH₂ (Nobuko et al., 2005).

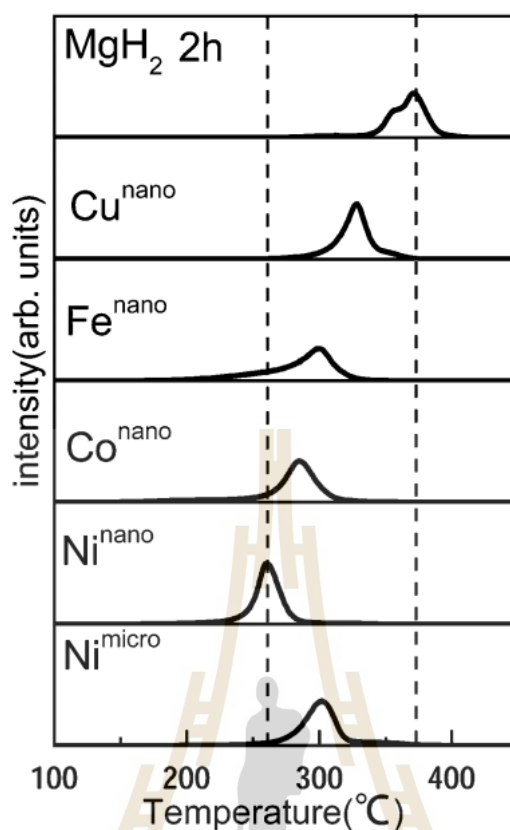


Figure 2.7 Thermal desorption mass spectra of hydrogen for milled MgH_2 and MgH_2 doped with 1 mol % Cu^{nano} , Fe^{nano} , Co^{nano} , and Ni^{nano} nanoparticle metals (Nobuko et al., 2005).

Furthermore, the kinetic properties of MgH_2 can be improved by carbon-based materials, such as graphite, carbon nanotubes (CNTs), multi-walled carbon nanotubes (MWCNTs), activated carbon (AC), and graphene (Guo et al., 2008). These carbon materials prevent particle agglomeration of MgH_2 upon cycling and facilitate hydrogen diffusion during the dehydrogenation and rehydrogenation (Liu et al., 2014). Recently, synergistic effects of the carbon materials and transition metal-based catalysts on hydrogen storage properties of Mg-H system have been intensively reported. For example, MgH_2 with 5wt.% NbF_5 + 5 wt.% single-walled carbon nanotubes absorbed 6.3 wt.% H_2 within 30 s at 300 °C (Luo et al., 2007). Moreover, Ismail et al. (2014) prepared $\text{MgH}_2\text{-FeCl}_3\text{-CNTs}$ showed the decrease of dehydrogenation temperature ($\Delta 90$ °C) and the improvement of sorption kinetics compared with the undoped $\text{MgH}_2\text{-FeCl}_3$ composite with hydrogen capacity of 4.3 wt.% within 4 min. Furthermore,

synergistic effects of transition metal halides (TiF_4 , NbF_4 , and ZrCl_4) and activated carbon nanofibers (ACNF) on reversible hydrogen storage of MgH_2 was investigated by Plerdsranoy et al. (2019). The onset and main desorption temperatures of MgH_2 reduced from 416 and 423 °C respectively, to 173 and 265 °C, respectively, with 4.7-5.0 wt.% H_2 within 1 h 30 min (Figure 2.8). Moreover, the activation energy (E_a) for desorption of MgH_2 significantly reduced from 140 to 37 kJ/mol (Plerdsranoy et al., 2019).

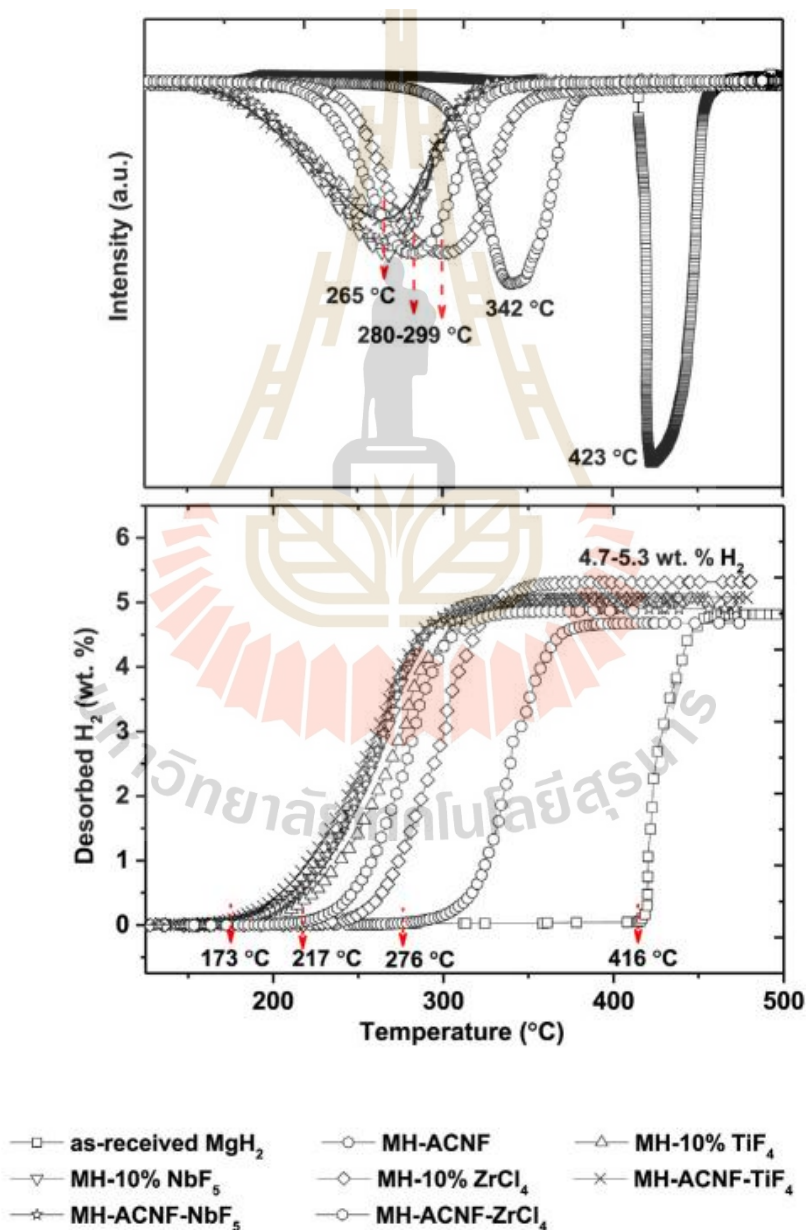
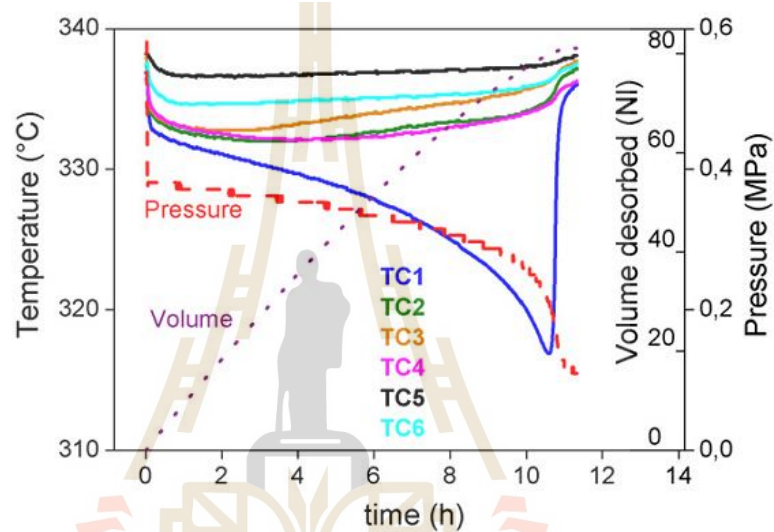


Figure 2.8 Temperature programmed desorption during desorption of all as-prepared samples (Plerdsranoy et al., 2019).

Currently, MgH_2 in the scales of hydrogen storage tanks has been considerably proposed. Chaise et al. (2010) reported that MgH_2 -based tank (123 g) stored reversibly 80 nl H_2 (5.8 wt.% H_2) at a pressure lower than 1 MPa. However, rehydrogenation and dehydrogenation rates were slow (2 h 30 min and 11 h, respectively) (Figure 2.9) as a consequence of the limitation of heat diffusion due to low thermal conductivity of MgH_2 powder.

(A)



(B)

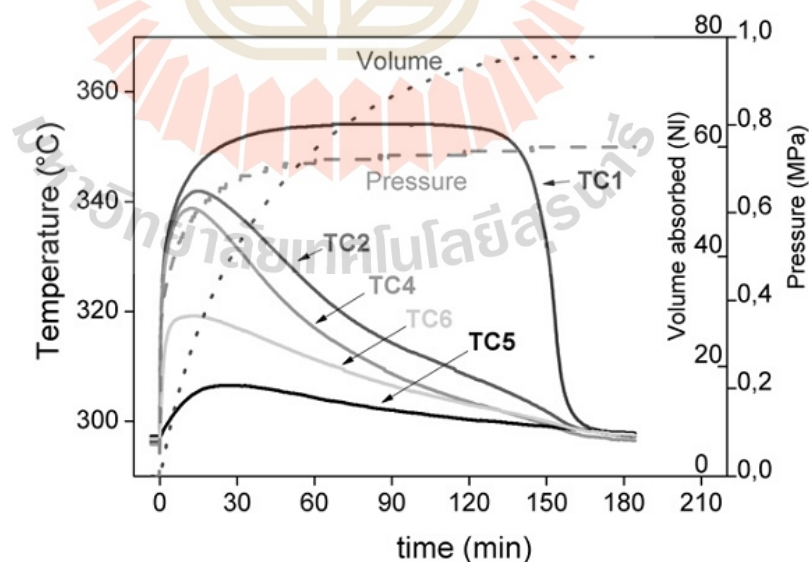


Figure 2.9 Experimental evolutions of temperature, pressure, and hydrogen volume during dehydrogenation at 340 °C under 0.1 MPa (A) and hydrogenation at 300 °C under 0.77 MPa (B) of MgH_2 -based tank (Chaise et al., 2010)

Therefore, for large-scale tanks using MgH_2 as hydrogen storage material, the basic problem lies with very low effective thermal conductivity, hydrogen diffusion, and mechanical stability during the cycling of hydride beds. In order to improve these problems, the MgH_2 was ball milled with expanded natural graphite (ENG), compacted into the pellets, and packed into the tanks integrated with heat exchanger systems in different geometries such as tube (Garrier et al., 2011 and Chibani and Bougriou, 2017), copper fins (Souahlia et al., 2014), and honeycomb (Bhouri et al., 2011). Furthermore, ENG improved not only the thermal conductivity but also hydrogen permeability, especially in radial direction as presented in Figure 2.10 (Garrier et al., 2011).

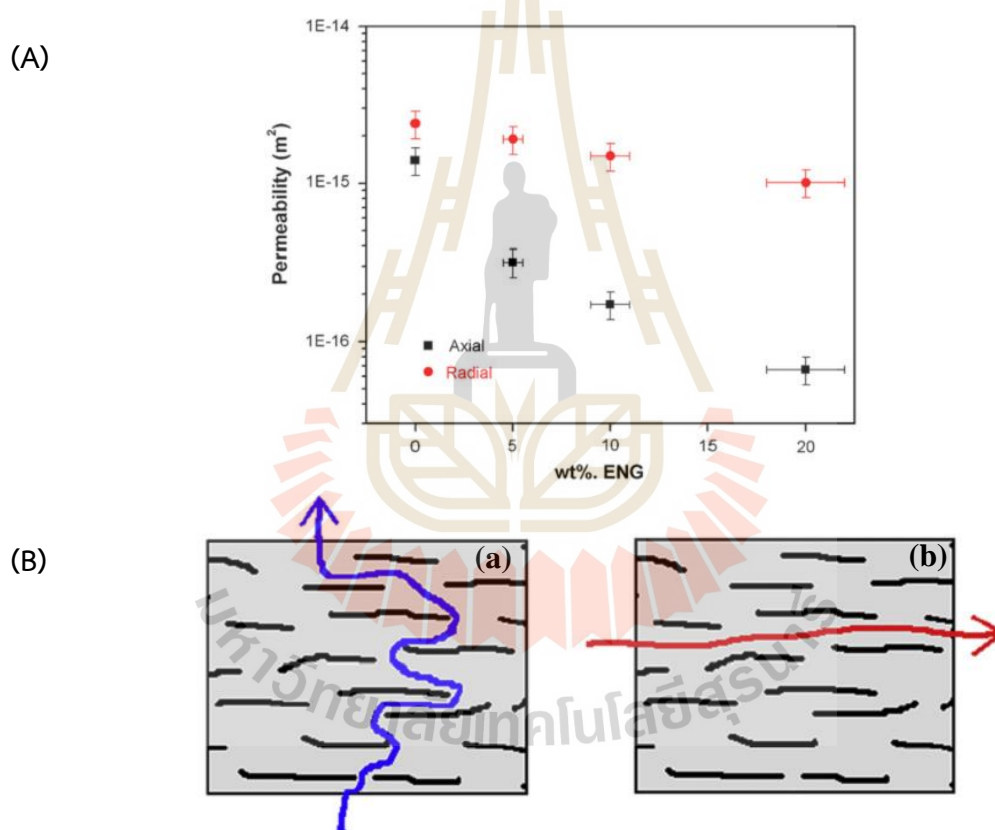


Figure 2.10 Axial and radial permeabilities of MgH_2 disks versus ENG contents (A) and diffusion path of hydrogen in compacted MgH_2 containing ENG (B) in the axial (a) and radial flows (b) (Garrier et al., 2011).

Next approach is the compositing of MgH_2 with other two or more hydrides, so-called reactive hydride composites (RHCs). RHCs lead to the formation of an unstable phase and/or a more stable product during dehydrogenation, facilitating the release

of hydrogen. For instance, MgH_2 composites with complex hydrides, such as amides (e.g., LiNH_2) (M. Ma et al., 2017), alanates (e.g., NaAlH_4) (Bhatnagar et al., 2014), and borohydrides (e.g., LiBH_4) (Cho et al., 2016). The MgH_2 - LiBH_4 composite has been widely investigated owing to high gravimetric hydrogen storage capacities of 11.4 wt.% H_2 . The desorption proceeds in two steps as shown in equations (2.3) and (2.4).



From Figure 2.11, it reveals the desorption enthalpy of $33 \text{ kJ mol}^{-1} \text{ H}_2$ for equation (2.3) lower than that of pristine LiBH_4 ($49 \text{ kJ mol}^{-1} \text{ H}_2$). In contrast, the entropy of equation (2.3) ($112 \text{ J K}^{-1} \text{ mol}^{-1} \text{ H}_2$) is in between those of pristine LiBH_4 ($97 \text{ J K}^{-1} \text{ mol}^{-1} \text{ H}_2$) and MgH_2 ($131 \text{ J K}^{-1} \text{ mol}^{-1} \text{ H}_2$). Achieving hydrogen reversibly for borohydrides is also found to be easier under this approach.

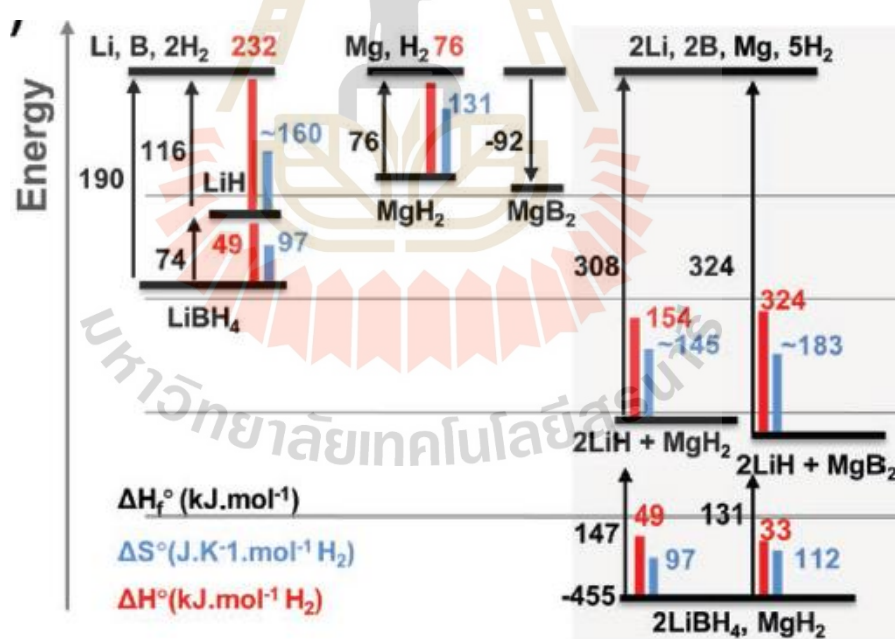


Figure 2.11 Thermodynamics of $\text{LiBH}_4/\text{MgH}_2$ composite as an example of evolution of the ΔH and ΔS as a function of the reaction paths. (Skeith, 2005) (Lai et al., 2019).

However, particle size agglomeration of RHCs was observed during cycling. The reduction of grain/particle size was done by addition of carbon-based materials, for

examples single-walled carbon nanotubes (SWCNTs), multi-walled carbon nanotubes (MWCNTs), activated carbon nanofibers (ACNFs), activated carbon (AC), and graphite. The addition of carbon-based materials not only reduces the particle size but also improves hydrogen diffusion and thermal conductivity. Furthermore, nanoconfinement of $2\text{LiBH}_4\text{-MgH}_2$ into nanoporous scaffold has been investigated because the nanoscale shortens diffusion distances for hydrogen and other light elements, leading to faster hydrogen desorption and absorption rates upon cycling as well as improvement of thermodynamic performance (Utke et al., 2016, Gosalawit-Utke et al., 2014 and Gosalawit-Utke et al., 2013). For further improvement of the packing efficiency, the hydride composite of $\text{LiBH}_4\text{-MgH}_2$ was compacted to pellet shape, benefiting thermal conductivity and mechanical stability during cycling (Jepsen et al., 2013). For example, the compacted sample of $\text{LiNH}_2\text{-MgH}_2\text{-ENG}$ (Pohlmann et al., 2012), $2\text{LiBH}_4\text{-MgH}_2$ doped with MWCNTs- TiO_2 (Plerdsranoy et al., 2017), and nanoconfined $\text{LiBH}_4\text{-LiAlH}_4$ in ACNFs (Plerdsranoy et al., 2017) showed not only the improvement of dehydrogenation kinetics and mechanical stability under high stress and expansion during cycling but also significant enhancement of thermal conductivity.

The last approach is alloying of MgH_2 with other metals. Besides thermodynamic improvement, hydrogen diffusion rates in Mg-based alloys have been demonstrated to be far more superior than that of pure Mg. Accordingly, introducing alloying elements to synthesize intermetallic compounds is an effective method to facilitate both the kinetics and thermodynamics of MgH_2 . In principle, there are two ways to prepare intermetallic hydrides. The first one is forming stable intermetallic hydrides with determined stoichiometry. Typical example is binary Mg_2Ni and ternary Mg_3MNi_2 ($\text{M} = \text{Al}, \text{Ti}, \text{Mn}$) alloys, which the stable intermetallic hydrides are formed when reacting with H_2 . The second one is a class of Mg-based solid solution or non-stoichiometry compounds, which can store a desirable amount of H_2 , such as Mg-In and Mg-In-Ni alloys (Lelis et al., 2010). Among Mg-based intermetallic hydride, Mg_2FeH_6 has drawn great attention for storing hydrogen due to the highest volumetric hydrogen density of $150 \text{ kg H}_2/\text{m}^3$, relatively high gravimetric content of 5.43 wt.% H_2 , and low cost (Mg and Fe) (Herrich et al., 2004). However, poor kinetics of Mg_2FeH_6 formation due to long distance for hydrogen diffusion obstructs its practical uses. Two methods

are proposed to solve this problem including (i) increase of the driving force for H, Mg, and Fe diffusion and (ii) reduction of H diffusion distance. Chen et al. (2016) synthesized $\text{Mg}_2\text{Fe}(\text{Ni})\text{H}_6$ nanowires from coarse-grained Mg and nano-sized-Fe(Ni) precursors by using γ -Fe stabilized by Ni instead of α -Fe commonly used for Mg_2FeH_6 formation. γ -Fe benefited the reduction of diffusion distance of Fe at the atomic level due to the same fcc lattice as Mg_2FeH_6 , which might remarkably shorten the diffusion distance of Fe during the formation of Mg_2FeH_6 from MgH_2 and Fe. In addition, the catalytic effect of Ni could facilitate the formation of Mg_2FeH_6 (Figure 2.12) (Chen et al., 2016).

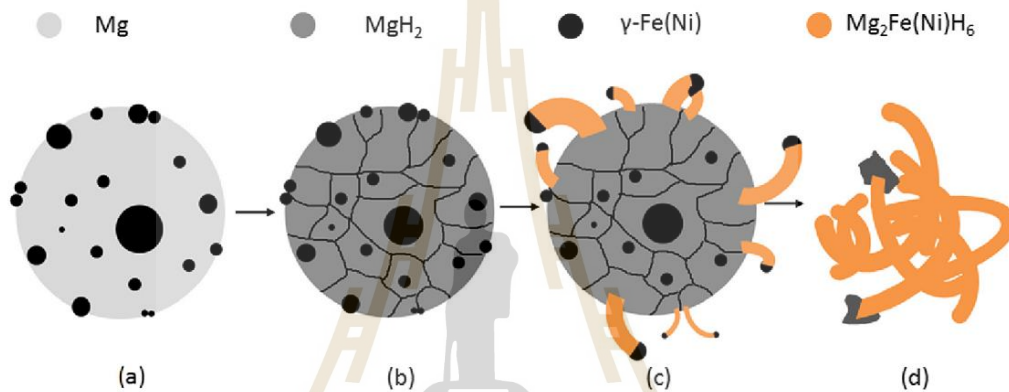


Figure 2.12 Schematic illustrations showing the formation of $\text{Mg}_2\text{Fe}(\text{Ni})\text{H}_6$ from coarse-grained Mg powder and γ -Fe(Ni) nanoparticles (Chen et al., 2016).

Besides, $\text{Mg}_2\text{Fe}(\text{Ni})\text{H}_6$ exhibited the reduction of dehydrogenation temperature and the improved desorption kinetics as compared to Mg_2FeH_6 prepared from α -Fe precursor. The peak dehydrogenation temperature decreases from 614.2 K (Mg_2FeH_6) to 592.6 K ($\text{Mg}_2\text{Fe}(\text{Ni})\text{H}_6$) (Figure 2.13) together with the reduction of sorption enthalpy of Mg_2FeH_6 (from 89 to 69 kJ/mol H_2). The improved thermodynamics was attributed to the destabilization of Mg_2FeH_6 through doping with Ni (Batalovic et al., 2014).

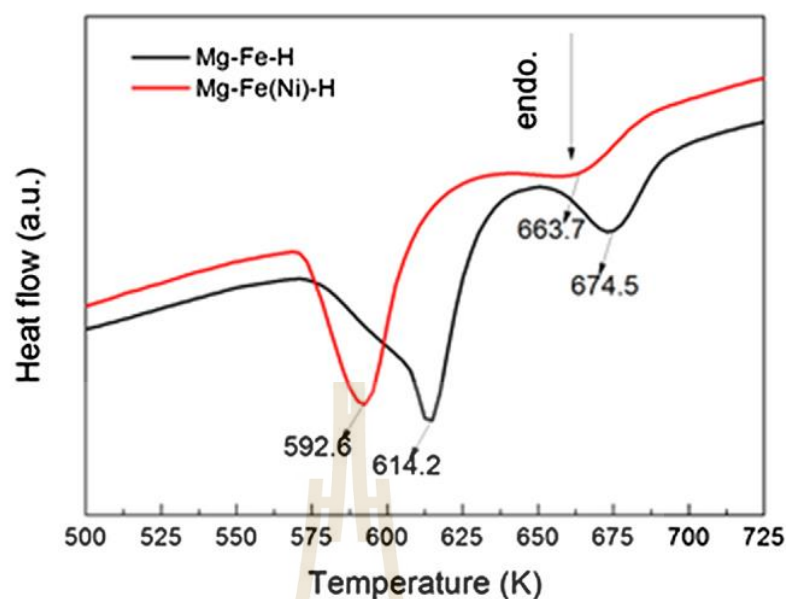


Figure 2.13 DSC curves during dehydrogenation of Mg-Fe-H and Mg-Fe(Ni)-H (Chen et al., 2016).

2.3 References

- Bardhan, R., Ruminski, A. M., Brand, A., and Urban, J. J. (2011). Magnesium nanocrystal-polymer composites: A new platform for designer hydrogen storage materials. *Energy & Environmental Science*, 4(12). doi:10.1039/c1ee02258j.
- Batalovic, K., Radakovic, J., Belosevic-Cavor, J., and Koteski, V. (2014). Transition metal doping of Mg_2FeH_6 -a DFT insight into synthesis and electronic structure. *Phys Chem Chem Phys*, 16(24), 12356-12361. doi:10.1039/c4cp01020e.
- Bhatnagar, A., Pandey, S. K., Dixit, V., Shukla, V., Shahi, R. R., Shaz, M. A., and Srivastava, O, N. (2014). Catalytic effect of carbon nanostructures on the hydrogen storage properties of MgH_2 - $NaAlH_4$ composite. *International Journal of Hydrogen Energy*, 39(26), 14240-14246. doi:10.1016/j.ijhydene.2014.04.179.
- Bhour, M., Goyette, J., Hardy, B. J., and Anton, D. L. (2011). Honeycomb metallic structure for improving heat exchange in hydrogen storage system. *International Journal of Hydrogen Energy*, 36(11), 6723-6738. doi:10.1016/j.ijhydene.2011.02.092.

- Broom, D. P. (2011). Hydrogen Storage Materials, The Characterisation of Their Storage Properties. *Springer London*. 23, ISBN-10:0857292226.
- Chaise, A., de Rango, P., Marty, P., and Fruchart, D. (2010). Experimental and numerical study of a magnesium hydride tank. *International Journal of Hydrogen Energy*, 35(12), 6311-6322. doi:10.1016/j.ijhydene.2010.03.057.
- Chen, X., Zou, J., Zeng, X., and Ding, W. (2016). Hydrogen storage in Mg₂Fe(Ni)H₆ nanowires synthesized from coarse-grained Mg and nano sized γ -Fe(Ni) precursors. *International Journal of Hydrogen Energy*, 41(33), 14795-14806. doi:10.1016/j.ijhydene.2016.06.024.
- Chibani, A., and Bougriou, C. (2017). Effect of the tank geometry on the storage and destocking of hydrogen on metal hydride (LaNi₅H₂). *International Journal of Hydrogen Energy*, 42(36), 23035-23044. doi:10.1016/j.ijhydene.2017.07.102.
- Cho, I. H., Gang, S., Lee, H., Shim, J-H., Park, M., and Choi, Y. N. (2016). Kinetic enhancement of LiBH₄-MgH₂ composite by pre-milled MWCNTs observed by in situ X-ray diffraction measurements. *International Journal of Hydrogen Energy*, 41(47), 22090-22096. doi:10.1016/j.ijhydene.2016.09.141.
- Chuanzhao, Z. G. S., Jingjing, W., Cheng, L., Yuanyuan, J., Xiaoyu, Ku., and Andreas, H. (2017). Prediction of Novel High-Pressure Structures of Magnesium Niobium Dihydride. *Applied Materials & Interfaces*, 31(9), 26169-26176.
- Crivello, J. C., Denys, R. V., Dornheim, M., Felderhoff, M., Grant, D. M., Huot, J., Jensen, T. R., de Jongh, P., Latroche, M., Walker, G. S., Webb, C. J., and Yartys, V. A. (2016). Mg-based compounds for hydrogen and energy storage. *Applied Physics A*, 122(2). doi:10.1007/s00339-016-9601-1.
- Czujko, T., Oleszek, E. E., and Szot, M. (2020). New Aspects of MgH₂ Morphological and Structural Changes during High-Energy Ball Milling. *Materials (Basel)*, 13(20). doi:10.3390/ma13204550.
- El-Eskandarany, M. S., Shaban, E., Aldakheel, F., Alkandary, A., Behbehani, M., and Al-Saidi, M. (2017). Synthetic nanocomposite MgH₂/5 wt.% TiMn₂ powders for solid-hydrogen storage tank integrated with PEM fuel cell. *Scientific Reports*, 7(1), 13296. doi:10.1038/s41598-017-13483-0.

- Gennari, F. C., Castro, F. J., and Andrade-Gamboa, J. J. (2002). Synthesis of Mg_2FeH_6 by reactive mechanical alloying: Formation. *Journal of Alloys and Compounds*, 339, 261-267.
- Gaboardi, M., Bliersbach, A., Bertoni, G., Aramini, M., Vlahopoulou, G., Pontiroli, D., Mauron, P., Magnani, G., Salviati, G., Züttel, A., and Riccò, M. (2014). Decoration of graphene with nickel nanoparticles: study of the interaction with hydrogen. *Journal of Materials Chemistry A*, 2(4), 1039-1046. doi:10.1039/c3ta14127f.
- Garrier, S., Chaise, A., de Rango, P., Marty, P., Delhomme, B., Fruchart, D., and Miraglia, S. (2011). MgH_2 intermediate scale tank tests under various experimental conditions. *International Journal of Hydrogen Energy*, 36(16), 9719-9726. doi:10.1016/j.ijhydene.2011.05.017.
- Gosalawit-Utke, R., Milanese, C., Nielsen, T. K., Karimi, F., Saldan, I., Pranzas, K., Jensen, T. R., Marini, A., Klassen, T., and Dornheim, M. (2013). Nanoconfined $2LiBH_4$ - MgH_2 for reversible hydrogen storages: Reaction mechanisms, kinetics and thermodynamics. *International Journal of Hydrogen Energy*, 38(4), 1932-1942. doi:10.1016/j.ijhydene.2012.11.064.
- Gosalawit-Utke, R., Thiangviriyaya, S., Javadian, P., Laipple, D., Pistidda, C., Bergemann, N., Horstmann, C., T. R., Marini, A., Klassen, T., and Dornheim, M. (2014). Effective nanoconfinement of $2LiBH_4$ - MgH_2 via simply MgH_2 premilling for reversible hydrogen storages. *International Journal of Hydrogen Energy*, 39(28), 15614-15626. doi:10.1016/j.ijhydene.2014.07.167.
- Gupta, A., Baron, G. V., Perreault, P., Lenaerts, S., Ciocarlan, R. G., Cool, P., Mileo, P. G. M., Rogge, S., Van Speybroeck, V., Watson, G., Van Der Voort, P., Houllberghs, M., Breynaert, E., Martens, J., and Denayer, J. F. M. (2021). Hydrogen Clathrates: Next Generation Hydrogen Storage Materials. *Energy Storage Materials*, 41, 69-107. doi:10.1016/j.ensm.2021.05.044.
- Herrich, M., Ismail, N., Lyubina, J., Handstein, A., Pratt, A., and Gutfleisch, O. (2004). Synthesis and decomposition of Mg_2FeH_6 prepared by reactive milling. *Materials Science and Engineering: B*, 108(1-2), 28-32. doi:10.1016/j.mseb.2003.10.031.

- Huang, Z. G., Guo, Z. P., Calka, A., Wexler, D., and Liu, H. K. (2007). Effects of carbon black, graphite and carbon nanotube additives on hydrogen storage properties of magnesium. *Journal of Alloys and Compounds*, 427(1-2), 94-100. doi:10.1016/j.jallcom.2006.03.069.
- Ismail, M., Juahir, N., and Mustafa, N. S. (2014). Improved Hydrogen Storage Properties of MgH₂ Co-Doped with FeCl₃ and Carbon Nanotubes. *The Journal of Physical Chemistry C*, 118(33), 18878-18883. doi:10.1021/jp5046436.
- Huot, J., Hayakawa, H., and Akiba, E. (1997). Preparation of the hydrides Mg₂FeH₆ and Mg₂CoH₅ by mechanical. *Journal of Alloys and Compounds* 248, 164-167.
- Jain, I. P., Lal, C., and Jain, A. (2010). Hydrogen storage in Mg: A most promising material. *International Journal of Hydrogen Energy*, 35(10), 5133-5144. doi:10.1016/j.ijhydene.2009.08.088.
- Jepsen, J., Milanese, C., Girella, A., Lozano, G. A., Pistidda, C., Bellosta von Colbe, J. M., Marini, A., Klassen, T., and Dornheim, M. (2013). Compaction pressure influence on material properties and sorption behaviour of LiBH₄-MgH₂ composite. *International Journal of Hydrogen Energy*, 38(20), 8357-8366. doi:10.1016/j.ijhydene.2013.04.090.
- Lai, Q., Sun, Y., Wang, T., Modi, P., Cazorla, C., Demirci, U. B., Ares Fernandez, J. R., Leardini, F., and Aguey, Z. K. F. (2019). How to Design Hydrogen Storage Materials Fundamentals, Synthesis, and Storage Tanks. *Advanced Sustainable Systems*, 3(9). doi:10.1002/adsu.201900043.
- Lelis, M., Milcius, D., Wirth, E., Hålenius, U., Eriksson, L., Jansson, K., Kadir, K., Ruan, J., Sato, T., Yokosawa, T., and Noréus, D. (2010). A mechanically switchable metal insulator transition in Mg₂NiH₄ discovers a strain sensitive, nanoscale modulated resistivity connected to a stacking fault. *Journal of Alloys and Compounds*, 496(1-2), 81-86. doi:10.1016/j.jallcom.2010.02.135.
- Liu, G., Wang, Y., Jiao, L., and Yuan, H. (2014). Solid-state synthesis of amorphous TiB₂ nanoparticles on graphene nanosheets with enhanced catalytic dehydrogenation of MgH₂. *International Journal of Hydrogen Energy*, 39(8), 3822-3829. doi:10.1016/j.ijhydene.2013.12.133.

- Luo, Y., Wang, P., Ma, L. P., and Cheng, H. M. (2007). Enhanced hydrogen storage properties of MgH_2 co-catalyzed with NbF_5 and single-walled carbon nanotubes. *Scripta Materialia*, 56(9), 765-768. doi:10.1016/j.scriptamat.2007.01.016
- Ma, M., Ouyang, L., Liu, J., Wang, H., Shao, H., and Zhu, M. (2017). Air-stable hydrogen generation materials and enhanced hydrolysis performance of MgH_2 - $LiNH_2$ composites. *Journal of Power Sources*, 359, 427-434. doi:10.1016/j.jpowsour.2017.05.087.
- Ma, Z., Panda, S., Zhang, Q., Sun, F., Khan, D., Ding, W., and Zou, J. (2021). Improving hydrogen sorption performances of MgH_2 through nanoconfinement in a mesoporous CoS nano-boxes scaffold. *Chemical Engineering Journal*, 406. doi:10.1016/j.cej.2020.126790.
- Nobuko, H. T. I., and Hironobu, F. (2005). Catalytic Effect of Nanoparticle 3d-Transition Metals on Hydrogen Storage Properties in Magnesium Hydride MgH_2 Prepared by Mechanical Milling. *The Journal of Physical Chemistry B*, 109, 7188-7194.
- Plerdsranoy, P., Chanthee, S., and Utke, R. (2017). Compaction of $LiBH_4$ - MgH_2 doped with $MWCNTs$ - TiO_2 for reversible hydrogen storage. *International Journal of Hydrogen Energy*, 42(2), 978-986. doi:10.1016/j.ijhydene.2016.11.066.
- Plerdsranoy, P., Javadian, P., Jensen, N. D., Nielsen, U. G., Jensen, T. R., and Utke, R. (2017). Compaction of $LiBH_4$ - $LiAlH_4$ nanoconfined in activated carbon nanofibers: Dehydrogenation kinetics, reversibility, and mechanical stability during cycling. *International Journal of Hydrogen Energy*, 42(2), 1036-1047. doi:10.1016/j.ijhydene.2016.09.056.
- Plerdsranoy, P., Thiangviriyaya, S., Dansirima, P., Thongtan, P., Kaewsuwan, D., Chanlek, N., and Utke, R. (2019). Synergistic effects of transition metal halides and activated carbon nanofibers on kinetics and reversibility of MgH_2 . *Journal of Physics and Chemistry of Solids*, 124, 81-88. doi:10.1016/j.jpocs.2018.09.001.
- Pohlmann, C., Röntzsch, L., Hu, J., Weißgärber, T., Kieback, B., and Fichtner, M. (2012). Tailored heat transfer characteristics of pelletized $LiNH_2$ - MgH_2 and $NaAlH_4$ hydrogen storage materials. *Journal of Power Sources*, 205, 173-179. doi:10.1016/j.jpowsour.2012.01.064.

- Rahmaninasab, M. A., Raygan, S., Abdizadeh, H., Pourabdoli, M., and Mirghaderi, S. H. (2018). Properties of activated MgH_2 + mischmetal nanostructured composite produced by ball-milling. *Materials for Renewable and Sustainable Energy*, 7(3). doi:10.1007/s40243-018-0122-z.
- Vajo, J. J., Skeith, S. L., and Mertens, F. (2005). Reversible Storage of Hydrogen in Destabilized LiBH_4 . *The Journal of Physical Chemistry B*, 109, 3719-3722.
- Souahlia, A., Dhaou, H., Mellouli, S., Askri, F., Jemni, A., and Ben, N. S. (2014). Experimental study of metal hydride-based hydrogen storage tank at constant supply pressure. *International Journal of Hydrogen Energy*, 39(14), 7365-7372. doi:10.1016/j.ijhydene.2014.02.121.
- Sun, Z., Lu, X., Nyahuma, F. M., Yan, N., Xiao, J., Su, S., and Zhang, L. (2020). Enhancing Hydrogen Storage Properties of MgH_2 by Transition Metals and Carbon Materials: A Brief Review. *Frontiers in Chemistry*, 8, 552. doi:10.3389/fchem.2020-00552.
- Utke, R., Thiangviriyaya, S., Javadian, P., Jensen, T. R., Milanese, C., Klassen, T., and Dornheim, M. (2016). $2\text{LiBH}_4\text{-MgH}_2$ nanoconfined into carbon aerogel scaffold impregnated with ZrCl_4 for reversible hydrogen storage. *Materials Chemistry and Physics*, 169, 136-141. doi:10.1016/j.matchemphys.2015.11.040.
- Wang, P., Tian, Z., Wang, Z., Xia, C., Yang, T., and Ou, X. (2021). Improved hydrogen storage properties of MgH_2 using transition metal sulfides as catalyst. *International Journal of Hydrogen Energy*, 46(53), 27107-27118. doi:10.1016/j.ijhydene.2021.05.172.
- Xie, W., West, D. J., Sun, Y., and Zhang, S. (2013). Role of nano in catalysis: Palladium catalyzed hydrogen desorption from nanosized magnesium hydride. *Nano Energy*, 2(5), 742-748. doi:10.1016/j.nanoen.2012.12.010.
- Zlotea, C., Oumellal, Y., Hwang, S.-J., Ghimbeu, C. M., de Jongh, P. E., and Latroche, M. (2015). Ultrasmall MgH_2 Nanoparticles Embedded in an Ordered Microporous Carbon Exhibiting Rapid Hydrogen Sorption Kinetics. *The Journal of Physical Chemistry C*, 119(32), 18091-18098. doi:10.1021/acs.jpcc.5b05754.
- Züttler, A., Borgschulte, A., and Schlapbach, L. (2008). Hydrogen as a Future Energy Carrier. *WILEY-VCH Verlag GmbH & Co. KGaA, Weinheim, ISBN: 978-3-527-30817-0*.

CHAPTER III

EXPERIMENTAL SECTION

3.1 Chemicals

Table 3.1 Chemicals used in this work.

Chemicals	Formular	specification	Supplier
Magnesium	Mg	≥99 %	Aldrich
Lithium borohydride	LiBH ₄	90% (hydrogen storage grade)	Aldrich
Magnesium hydride	MgH ₂	98%	Alfa Aesar
Titanium tetrafluoride	TiF ₄	99%	Acros Organics
Multiwall carbon nanotubes	-	-	Nano Generation
Activated carbon nanofibers	-	-	
Iron	Fe	99.99%	Aldrich
Nickel	Ni	≥99%, -100 mesh	Alfa Aesar
Polyacrylonitrile	(C ₃ H ₃ N) _n	Mw=150,000 g/mol	Aldrich
N, N-dimethylformamide	HCON(CH ₃) ₂	reagent	Carlo Erba Reagent
Potassium hydroxide	KOH	Analytical	QRëC

3.2 Apparatus

3.2.1 Glove box

Due to the sensitivity of hydride materials to air and moisture, the procedures during samples preparation and some characterizations were handled in a filled-N₂ glove boxes.



Figure 3.1 Glove box (Omni-Lab System, VAC) used in the laboratory.

3.2.2 High energy ball milling

The ball milling was used for particle size reduction and sample preparation.

(A)

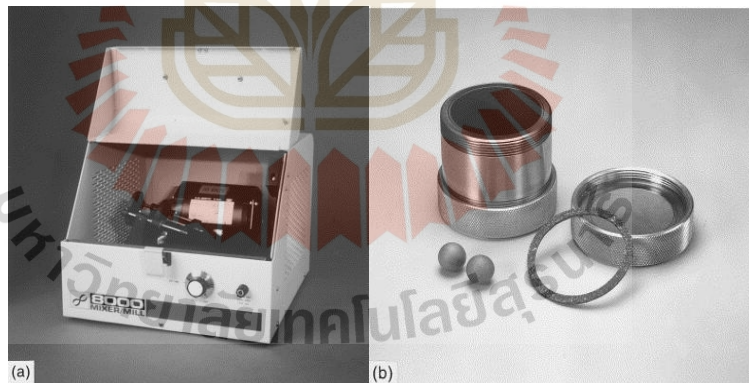


Figure 3.2 Different types of ball mill, a Spex 8000 M Mixer/Mill (A).

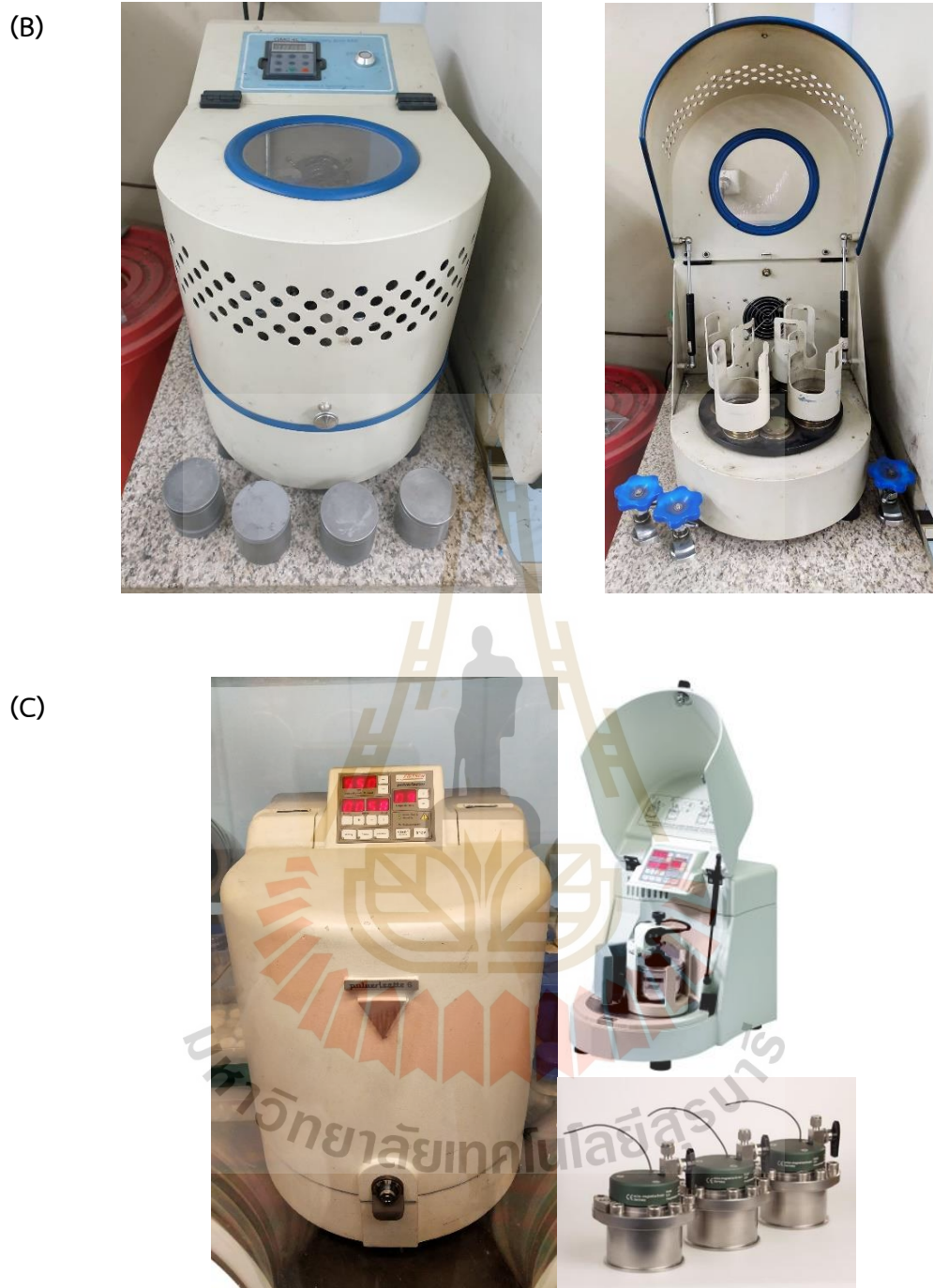


Figure 3.2 (Continued) Different types of ball mill, a QM0.4L Planetary Ball Mill, Nanjing Chishun Science & Technology (B) and a Planetary Mono Mill PULVERISETTE 6 (C).

3.2.3 Autoclave

The autoclave was used for heat treatment process at high pressure and temperature.



Figure 3.3 Autoclave from Parr Instruments (4838 reactor controller).

3.3 Preparation of compacted $2\text{LiBH}_4\text{-MgH}_2\text{-ACNFs}$

The activated carbon nanofibers (ACNFs) were prepared by the carbonization and electrospinning techniques. The 10 % w/v solution of polyacrylonitrile (PAN) in N, N-dimethylformamide was used as polymer precursor for electrospinning. The PAN solution was transferred to polypropylene syringe (10 ml) with stainless steel needle (diameter of 22 mm). A syringe pump injected PAN solution at a flow rate of 1.5 ml/h. The electrospinning was done using the voltage of 10 kV at room temperature with a distance between the spinner and the fiber collector of 15 cm. The PAN- nanofibers were stabilized in the air at 280 °C for 3 h and carbonized at 1000 °C in N_2 for 1 h to obtain carbon nanofibers (CNFs). The CNFs were treated with 30 % w/v KOH for 2 h at 80 °C and dried at room temperature for 24 h. CNFs were carbonized at 800 °C under N_2 atmosphere for 15 min to obtain activated carbon nanofibers (ACNFs). To neutralize residual KOH, ACNFs were immersed in 0.5 M HCl at room temperature for 30 min and washed with deionized water until the pH of the filtrate reached pH 6. The obtained

ACNFs were dried at 120 °C for 24 h. Before milling with 2LiBH₄-MgH₂ composite, ACNFs were treated at 500 °C under vacuum for 3 h.

The composite of 2LiBH₄-MgH₂ was prepared by milling LiBH₄ and powder Mg under a 2:1 molar ratio (LiBH₄: Mg). The powder sample was milled under a ball to powder ratio (BPR) of 20:1 for 10 h in a N₂-filled glove box using a SPEC Sample Prep 8000D DUAL Mixer/Mill. The mixture was hydrogenated at 350 °C under 80 bar H₂ for 12 h to obtain 2LiBH₄-MgH₂ composite, denoted as 2Li-MH. ACNFs (30 wt. %) were milled with 2Li-MH for 30 min (BPR = 10:1), to obtain 30 wt. % ACNFs-doped 2Li-MH, denoted as 2Li-MH-30%. The powder samples of 2Li-MH and 2Li-MH-30% were compacted into the pellets (diameter of 12 mm).

3.4 Synthesis of Ni-doped Mg₂FeH₆

Mg₂FeH₆ was synthesized by milling MgH₂ and Fe with a molar ratio of 2:1 (MgH₂: Fe) for 40 h under 20 bar H₂ using a Planetary Mono Mill PULVERISETTE 6. The BPR and the rotational speed of 30: 1 and 500 rpm, respectively, were applied. The as-milled sample was hydrogenated at 550 °C under 45 bar H₂ for 15 h with a Parr 4838 reactor controller (Figure 3.3). After heat treatment, the sample was milled using a Spex SamplePrep 8000M MIXER/MILL with BPR of 10:1 for 90 min under Ar atmosphere to obtain as-prepared Mg₂FeH₆. Ni powder of 5 and 20 wt.% was milled with as-prepared Mg₂FeH₆ for 30 min with BPR of 10:1 under Ar atmosphere. The mixtures were sintered at 450 °C under 60 bar H₂ for 48 h using a sieverts-type apparatus designed by HERA, Quebec, Canada to obtain Mg₂FeH₆ doped with 5 and 20 wt.% Ni, denoted as 5%Ni-Mg-Fe and 20%Ni-Mg-Fe, respectively.

3.5 Up scaling of MgH₂-TiF₄-MWCTs to tank scale

Mg powder was hydrogenated under 15-20 bar H₂ for 12 h at 320 °C to achieve as-prepared MgH₂. TiF₄ (5 wt.%) was milled for 5 h and milled with as-prepared MgH₂ for 3 h using BPR and rotation speed of 10:1 and 580 rpm, respectively. The powder sample of MgH₂ doped with TiF₄ was hydrogenated under 10-15 bar H₂ for 2 h at 250 °C. The obtained sample was milled with 5 wt.% treated MWCNTs for 30 min using BPR and rotational speed of 10:1 and 580 rpm, respectively, to obtain MgH₂ doped with 5 wt.% each of TiF₄ and MWCNTs, denoted as MH-TiF₄- MWCNT.

MH-TiF₄-MWCNT (45.15 g) was packed tightly into the stainless-steel mesh cylinder (SS304, No. 120), placed into the storage tank (packing volume of 96.2 mL) (Figure 3.4(A)). The top flange was mounted with hydrogen supply tube and five K-type thermocouples (TC1-TC5), located at different locations inside the storage tank, while the bottom one was with a double tube heat exchanger wrapped with SS mesh (Figure 3.4(A)). Heat transfer fluid (compressed air) was supplied to the inner tube and flowed through the space between the inner and outer tubes (Figure 3.4(D)).

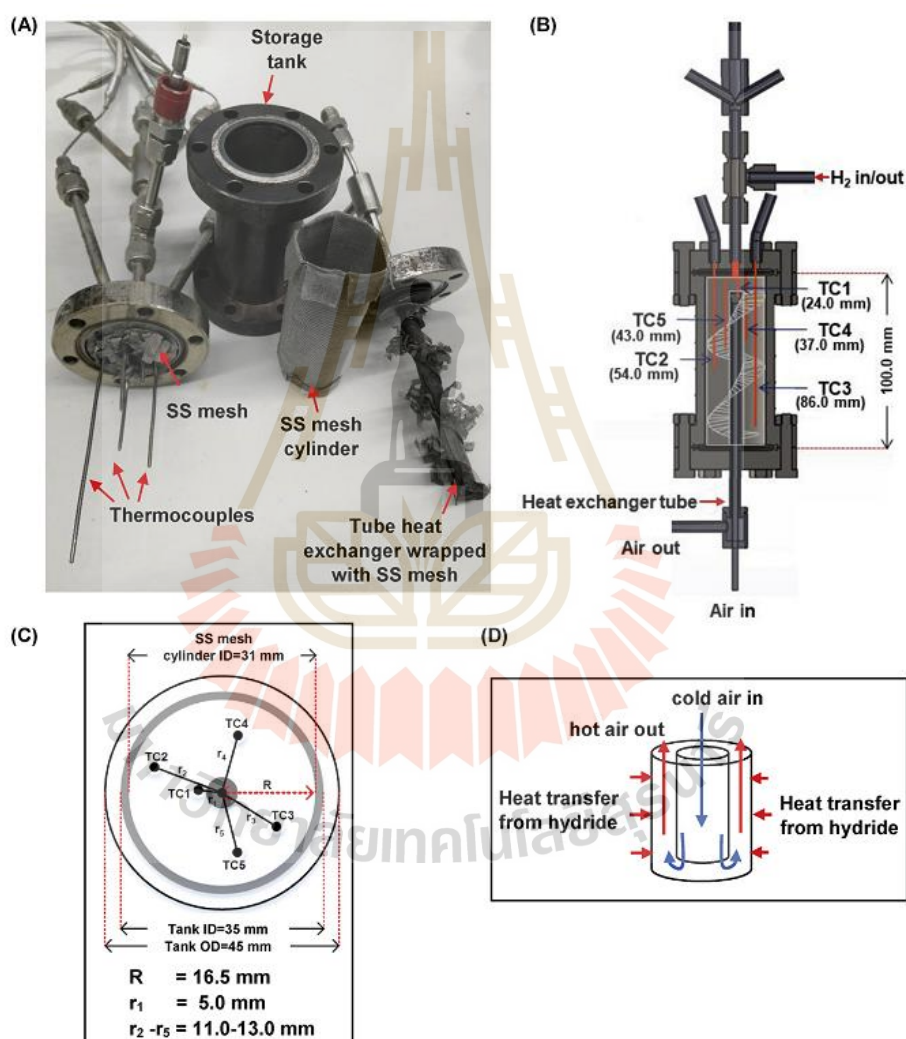


Figure 3.4 The components of hydrogen storage tank (A), positions of thermocouples along the tank length (B) and radius (C), and central tube heat exchanger (D).

3.6 Characterizations

3.6.1 Chemical compositions and structures

3.6.1.1 Powder x-ray diffraction (PXD)

Powder x-ray diffraction (PXD) was performed using a D2 PHASER, Bruker with Cu K α radiation ($\lambda=1.5406 \text{ \AA}$) and. The diffractions were collected in a 2θ range of $10-80^\circ$ with a scanning step of $0.02^\circ/\text{s}$. To prevent the sample from oxidation or hydrolysis, it was packed in an airtight sample holder, covered by a poly (methyl methacrylate) (PMMA) dome (Figure 3.5).



Figure 3.5 An airtight sample holder covered with PMMA dome for PXD experiments.

3.6.1.2 In situ synchrotron radiation powder x-ray diffraction (SR-PXD)

In situ synchrotron radiation powder x-ray diffraction (SR-PXD) was performed at the beamline P.02.1, PETRA III, Deutsches Elektronen-Synchrotron (DESY), Germany. The used wavelength (λ) was 0.20761 \AA and the 2D patterns were recorded using a Perkin Elmer plate image detector (2048×2048 pixel with the size of $200 \times 200 \mu\text{m}^2$). The sample was loaded into a sapphire capillary under Ar atmosphere in the glovebox and placed into a custom-designed sample cell with controlled temperature and pressure (Figure 3.6). The sample was heated from room temperature to $400 \text{ }^\circ\text{C}$ ($5 \text{ }^\circ\text{C}/\text{min}$), kept at $400 \text{ }^\circ\text{C}$ for 30 min, and cooled to room temperature. Collected data was integrated into one-dimensional diffraction pattern using a Fit2D software.

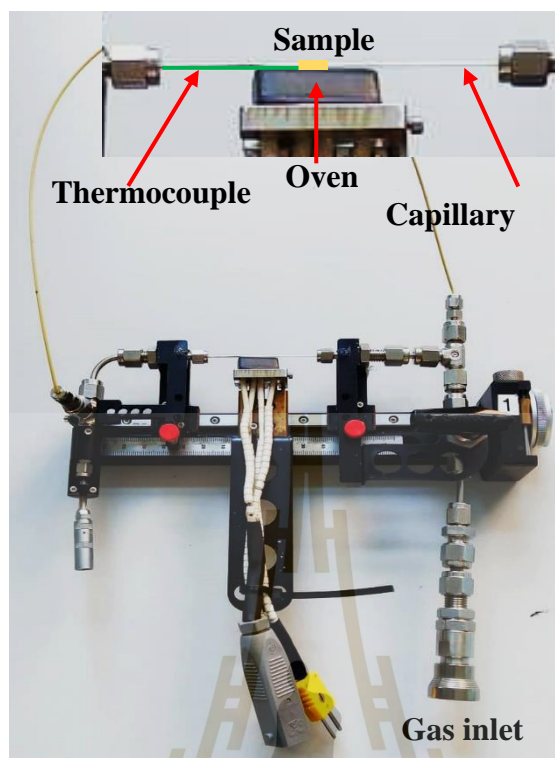


Figure 3.6 In situ SR-PXD sample cell.

3.6.1.3 X-ray absorption spectroscopy (XAS)

X-ray absorption spectroscopy (XAS), including x-ray absorption near edge structure (XANES) and extended x-ray absorption fine structure (EXAFS) were conducted at the SUT-NANOTEC-SLRI XAS beamline (BL5.2, electron energy of 1.2 GeV), Synchrotron Light Research Institute (SLRI), Nakhon Ratchasima, Thailand (Figure 3.7) (Kidkhunthod, 2017). XANES and EXAFS spectra at the Ni K-edge (8333 eV) were collected in a fluorescence mode using a 4-element Si-drifted detector. After background subtraction in the pre-edge and post-edge regions, XAS data were normalized using an ATHENA software included in an IFEFFIT package (Kidkhunthod, 2017, Klysubun and Limpijumnong, 2017, Newville, 2001, and Ravel and Newville, 2005). The local structure around Ni atoms was studied by fitting EXAFS data to the simulated model using a nonlinear least square fitting procedure in the ARTEMIS program. Due to the large noise at high k -space, the data fitting was performed with a maximum k -value of 10 \AA^{-1} and the fitting quality was evaluated by R -factor.

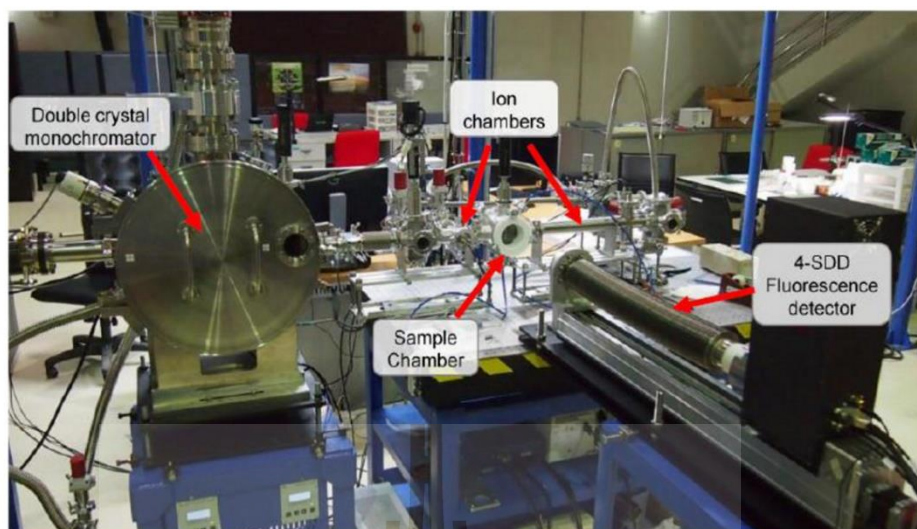


Figure 3.7 The set-up at BL5.2 SUT-NANOTEC-SLRI XAS beamline, SLRI, Thailand (Kidkhunthod, 2017).

3.6.1.4 Fourier Transform Infrared Spectrometry (FTIR)

Fourier transform infrared spectrometry (FTIR) experiment was carried out in the wavenumber range of $400\text{--}4000\text{ cm}^{-1}$ and the number of scans of 64 using a Tensor 27-Hyperion 2000 (Bruker) (Figure 3.8). The KBr powder was dried at $120\text{ }^{\circ}\text{C}$ overnight prior utilization. The sample was ground with dried KBr using a mortar and pressed under specific pressure to obtain the KBr pellet. The latter was assembled into FTIR spectrometer.



Figure 3.8 FTIR spectrometer of Tensor 27-Hyperion 2000 (Bruker).

3.6.2 Hydrogen sorption properties

3.6.2.1 Simultaneous Thermal Analysis (STA) coupled with Mass Spectroscopy (MS)

The dehydrogenation mechanisms were investigated by simultaneous thermal analysis (STA) and mass spectroscopy (MS) using a STA 449 F3 Jupiter coupled with a QMS 403C (Netzsch) (Figure 3.9). The powder sample (10-20 mg) was placed in an alumina crucible. The samples were heated from room temperature to 500 °C (5 °C/min) under the nitrogen flow of 50 mL/min. The relative composition of hydrogen in the exhaust gas was investigated by MS technique.

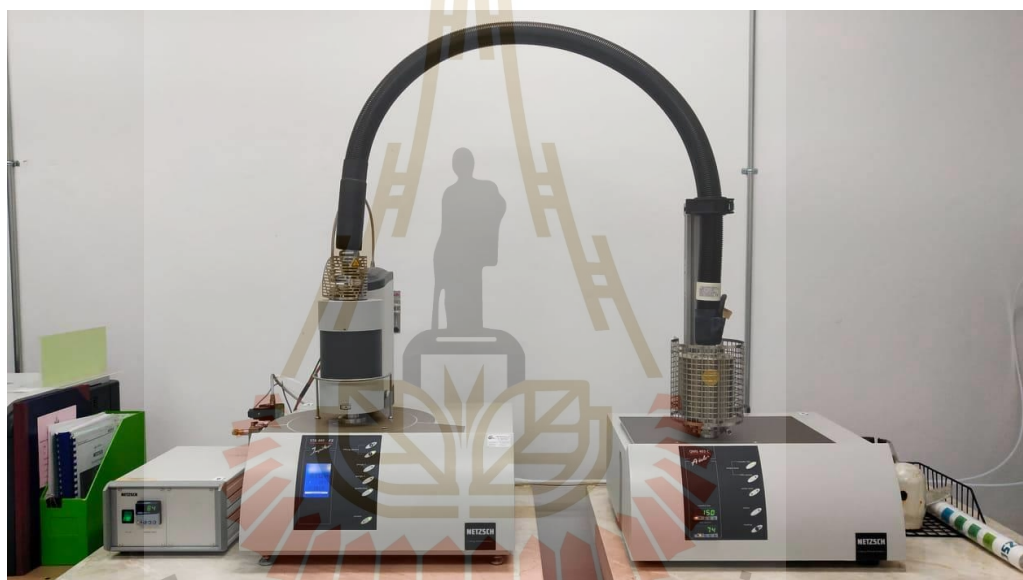


Figure 3.9 A STA 449 F3 Jupiter coupled with QMS 403C (Netzsch).

3.6.2.2 Differential scanning calorimetry (DSC)

The activation energy (E_a) during dehydrogenation was determined by differential scanning calorimetry using a DSC 204 F1 PHOENIX, Netzsch. The samples were heated from room temperature to 500 °C with the heating rates of 5, 10, 15, and 20 °C/min under N_2 flow of 50 mL/min. E_a was calculated using a Kissinger method (equation. (3.1)) (Kissinger, 1957) (Plerdsranoy et al, 2017).

$$\ln(\beta/T_p^2) = -(E_a/RT) + \ln(k_0R/E_a) \quad (3.1)$$

Where β is the heating rate, T_p indicates peak temperature of dehydrogenation in DSC curve, R is gas constant ($8.314 \text{ J K}^{-1}\text{mol}^{-1}$), and k_0 is frequency factor.

3.6.2.3 Sievert-type apparatus in laboratory scale

Hydrogen de/rehydrogenation performances of the samples were investigated using a sievert-type apparatus (Figure 3.10). The sample (60-70 mg) was packed into the stainless-steel sample holder in N₂ atmosphere in the glove box and transferred to the sievert-type apparatus. Dehydrogenation was investigated by heating the sample to 400 °C under 3 bar H₂. Rehydrogenation was carried out at 400 °C under 80 bar H₂ for 12 h. The amount of hydrogen release and uptake was calculated by the pressure change (ΔP) using the following equation:

$$(\Delta P) V = nRT \quad (3.2)$$

where P, V, n, R, and T are H₂ pressure (atm), volume of the system (L), the number of hydrogen moles (mol), and gas constant (0.0821 L atm K⁻¹ mol⁻¹) and temperature (K), respectively.

(A)



(B)

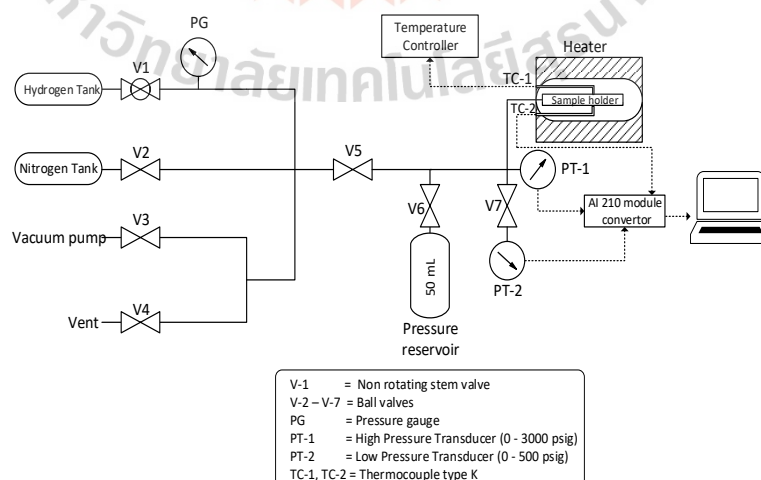


Figure 3.10 Photo (A) and schematic diagram (B) of Sievert-type apparatus.

Another sievert-type apparatus based on volumetric method used in this thesis work was from HERA, Quebec, Canada (Figure 3.11). The powder sample (150-180 mg) was packed to the sample holder under Ar atmosphere and transferred to the sievert-type apparatus. Dehydrogenation and rehydrogenation were investigated by heating the powder samples to 330 °C (3 °C/min) under 0.1 and 40 bar H₂ for dehydrogenation and rehydrogenation, respectively.

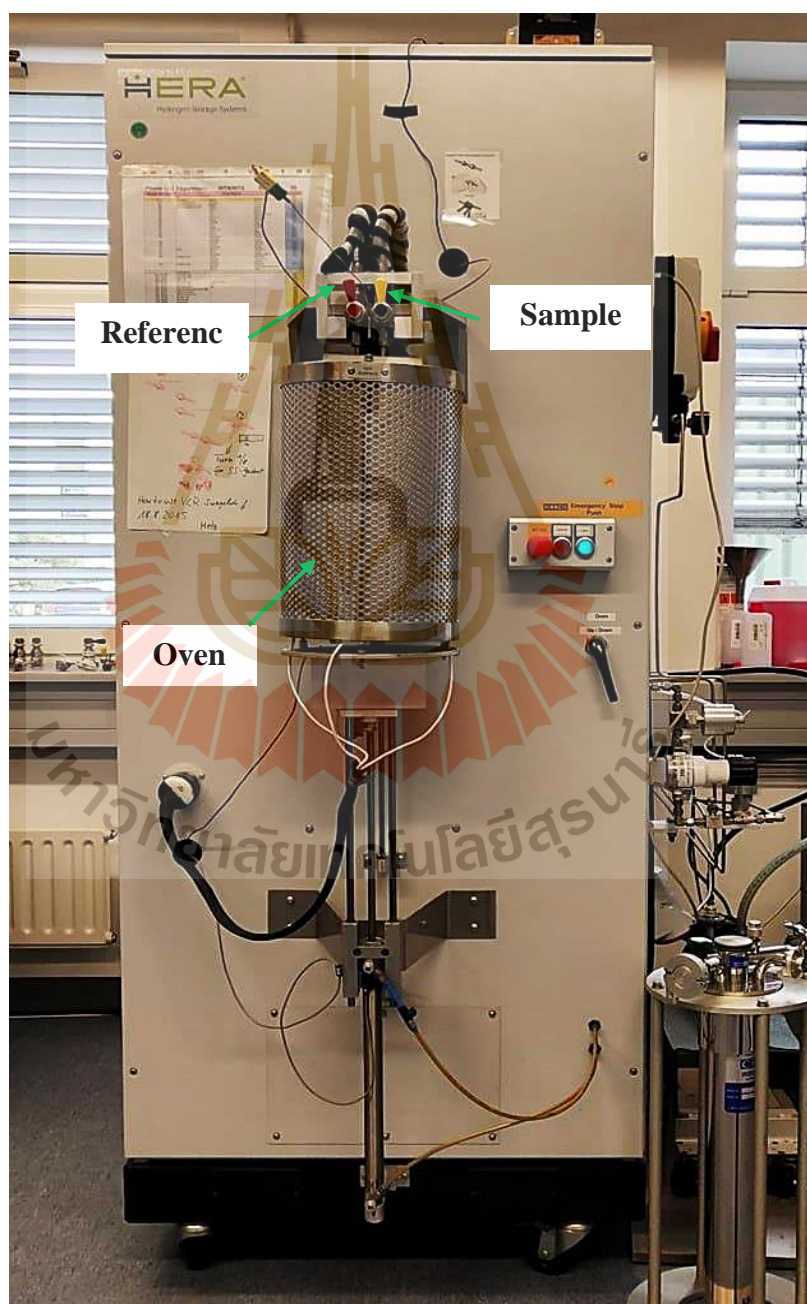


Figure 3.11 Sievert-type apparatus (HERA, Quebec, Canada).

3.6.2.4 Sievert-type apparatus in tank scale

De/rehydrogenation was carried out using a test station automatically controlled by the software developed in a LabVIEW® environment (Figure 3.12) (Thongtan et al., 2018). Two pressure transducers with operating pressures of 0-1500 psig (PX409-1.5KGI, OMEGA Engineering) and 0-3000 psig (PX309-3KGI, OMEGA Engineering) were used to measure the system pressure during the experiments. Hydrogen gas released from and applied to the tank during de/rehydrogenation was controlled by the direct-acting plunger solenoid valves (Type 0255, Bürkert). Hydrogen content liberated during desorption was measured by a mass flow controller (MFC, a Bronkhorst EL-FLOW select F-201CV) with operating flow rate of 0-2 standard L/min (SLM), which standard temperature (T_s) and pressure (P_s) were 294.15 K and 1.0085 bar, respectively. The temperature, pressure, and mass flow rate as well as the command to automatically open and close the solenoid valves were transferred to the computer using the module data loggers (NI USB-6009, National Instruments and AI210, Wisco). Hydrogenation was done under the isothermal condition at setting temperature (T_{set}) of 250-300 °C under 10-20 bar H_2 , while dehydrogenation was at $T_{set} = 300$ °C with the initial pressure of ~ 15 bar H_2 , remaining after hydrogenation. During hydrogenation, compressed air at room temperature ($T \sim 25-27$ °C) with the flow rate of $\sim 3-5$ L/min was used as heat transfer fluid. The volume of hydrogen gas released from the tank (standard L, SL) was calculated by integrating the area of the plot between hydrogen flow rate (SLM) and time (min). Total hydrogen storage capacity defined as the combination of material storage capacity and hydrogen content remaining after hydrogenation was calculated by the following equations:

$$V_{STP} = \frac{P_s V_s T_{STP}}{T_s P_{STP}} \quad (3.3)$$

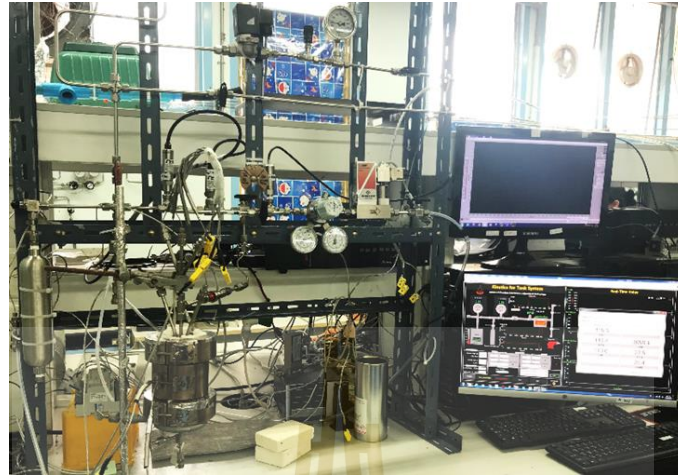
$$n_{H_2} = \frac{V_{STP}}{22.4 \text{ L/mol}} \quad (3.4)$$

$$H_2 \text{ capacity (wt.\%)} = \frac{n_{H_2} \times 2.016 \text{ g/mol}}{\text{sample weight (g)}} \times 100 \quad (3.5)$$

where V_{STP} (L) and V_s (SL) are the volumes of hydrogen gas at standard temperature and pressure condition (STP, $T_{STP} = 273.15$ K and $P_{STP} = 1.0133$ bar) and at the standard condition of MFC, respectively. n_{H_2} (mol) is hydrogen mole and standard molar volume

is 22.4 L/mol.

(A)



(B)

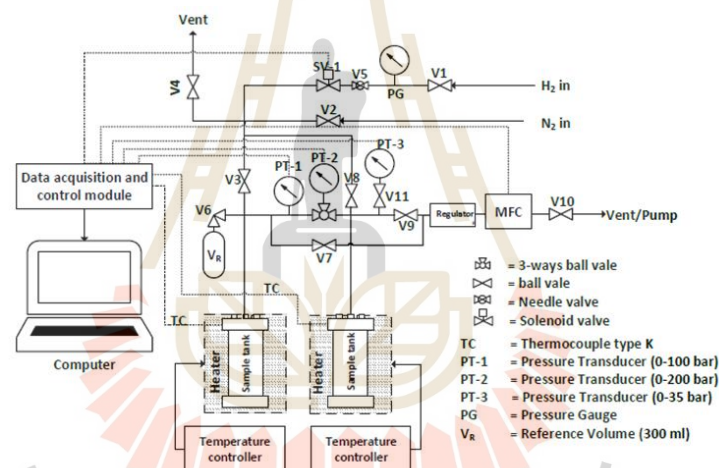


Figure 3.12 Photo (A) and schematic diagram (B) of Sievert-type apparatus in tank scale.

3.6.3 Integration of PEMFC stack and hydrogen storage tank

Proton exchange membrane fuel cell (PEMFC) stack containing 13 single cells with a rated power of 20 W requiring hydrogen flow rate at a maximum output of 0.28 L/min was purchased from Fuel Cell Store, USA (a Horizon 20WPEM Fuel cell). Polarization experiments and electrical performances of PEMFC stack supplied by hydrogen gas were characterized at room temperature (30 °C) under atmospheric pressure using a N3304A 300 W Electronic Load Module (Keysight Technologies, USA). Anode of PEMFC stack was fed by humidified hydrogen gas with flow rates of 0.10-0.25 SLM, while cathode was with air under atmospheric pressure. The measurements were

carried out using a constant current (CC) mode in the range of 0.05-2.55 A. The current increment and the dwelling time at each step were 0.05 A/step and 5 s/step, respectively. Stabilization time during an open-circuit voltage (OCV) for all experiments was 1 h.

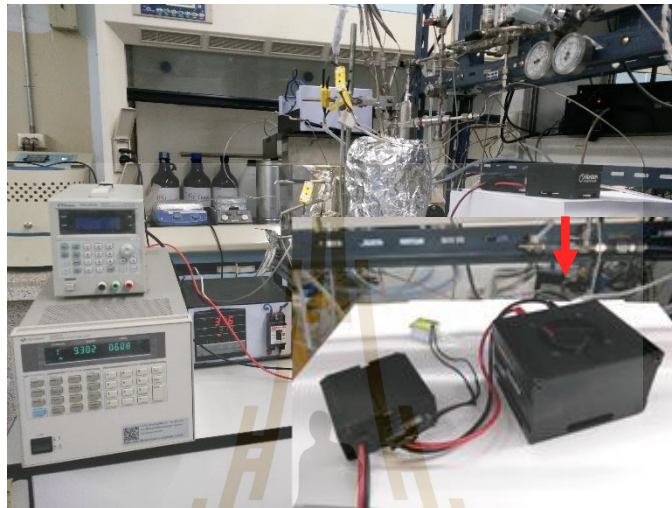


Figure 3.13 The measurement setup of electrical performances of integrated PEMFC-H₂ tank system.

3.6.4 Hydrogen diffusion and thermal conductivity

3.6.4.1 Hydrogen permeability

Hydrogen permeability in the axial direction was investigated using the same transient method, reported by Sitthiwet et al. (2017) (Figure 3.13) following the method of Brace et.al. (2015) and Ghanizadeh et al. (2017). The powder sample (~0.70-0.80 g) was compacted into the pellet using a die set (diameter of 12 mm) under the pressures of 1300 MPa to obtain the pellet samples with the thickness of 6.00 – 7.20 mm. The hydrogen permeability of the pellet sample was characterized at ambient temperature (~30 °C) by applying hydrogen pressure of 6 bar in the upstream chamber and evacuating the downstream chamber to ~0.7 bar. The pressures of the upstream and downstream chambers were recorded using pressure transducers (0–500 psig, C206 Cole Parmer). When volumes of upstream ($2.27 \times 10^{-5} \text{ m}^3$) and downstream ($2.22 \times 10^{-5} \text{ m}^3$) chambers were comparable and gas was ideal, the gas permeability was calculated by equations (3.6) and (3.7).

$$\frac{(P_u - P_d)}{(P_{u,0} - P_{d,0})} = e^{-\alpha t} \quad (3.6)$$

where $(P_u - P_d)$ is the difference pressure between the upstream and downstream chambers, $(P_{u,0} - P_{d,0})$ is the difference pressure between the upstream and downstream chambers at the initial stage, t is time (s), and α is explained by equation (3.7).

$$\alpha = \frac{kA(P_{u,0} + P_{d,0})}{2\mu L} (1/V_u + 1/V_d) \quad (3.7)$$

where k is hydrogen permeability (m^2), L is the sample thickness (6.1×10^{-3} m), A is the sample cross-section area (1.13×10^{-4} m^2), μ is hydrogen gas viscosity at 30 °C (8.95×10^{-6} Pa s), and V_u and V_d are the volumes of the upstream and downstream chambers, respectively (2.27×10^{-5} and 2.22×10^{-5} m^3 , respectively).

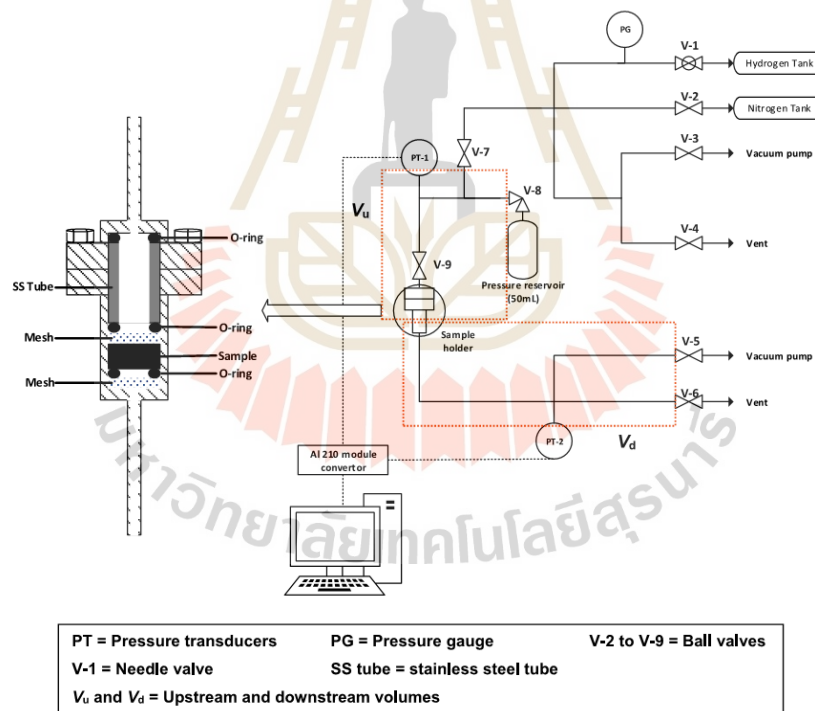


Figure 3.14 Schematic diagram of hydrogen permeability setup.

3.6.4.2 Thermal conductivity

Thermal conductivity and the thermal diffusivity were measured in the axial direction using Transient Plane Source (TPS) method (Al-Ajlan, 2006) (a TPS 1500

system, C3 Prozess-und Analysetechnik, Germany). The experiment was done at room temperature using the supplied power of 200 mW.

3.7 References

- Al-Ajlan, S. A. (2006). Measurements of thermal properties of insulation materials by using transient plane source technique. *Applied thermal engineering*, 26(17), 2184-2191.
- Kissinger, H. E. (1957). Reaction Kinetics in Differential Thermal Analysis. *Analytical Chemistry* 29(11), 1702-1706.
- Klysubun, W., Kidkhunthod, P., Tarawarakarn, P., Sombunchoo, P., Kongmark, C., and Limpijumnong, S. (2017). SUT-NANOTEC-SLRI beamline for X-ray absorption spectroscopy. *Journal of Synchrotron Radiation* 24, 707-716.
- Newville, M. (2001). EXAFS analysis using FEFF and FEFFIT. *Journal of Synchrotron Radiation*, 8, 96-100.
- Kidkhunthod, P. (2017). Structural studies of advanced functional materials by synchrotron-based x-ray adsorption spectroscopy: BL5.2 at SLRI, Thailand. *Advance Natural Sciences: Nanoscience and Nanotechnology*, 8(035007.).
- Pan, Z., Ma, Y., Connell, L. D., Down, D. I., and Camilleri, M. (2015). Measuring anisotropic permeability using a cubic shale sample in a triaxial cell. *Journal of Natural Gas Science and Engineering*, 26, 336-344.
- Plerdsranoy, P., Javadian, P., Jensen, N. D., Nielsen, U. G., Jensen, T. R., and Utke, R. (2017). Compaction of $\text{LiBH}_4\text{-LiAlH}_4$ nanoconfined in activated carbon nanofibers: Dehydrogenation kinetics, reversibility, and mechanical stability during cycling. *International Journal of Hydrogen Energy*, 42(2), 1036-1047. doi:10.1016/j.ijhydene.2016.09.056.
- Ravel, B., and Newville, M. (2005). ATHENA, ARTEMIS, HEPHAESTUS: data analysis for X-ray absorption spectroscopy using IFEFFIT. *Journal of Synchrotron Radiation*, 12(4), 537-541. doi:10.1107/S0909049505012719.

Sitthiwet, C., Thiangviriya, S., Thaweelap, N., Meethom, S., Kaewsuwan, D., Chanlek, N., and Utke, R. (2017). Hydrogen sorption and permeability of compacted LiBH_4 nanoconfined into activated carbon nanofibers impregnated with TiO_2 . *Journal of Physics and Chemistry of Solids*, 110, 344-353.

Thongtan, P., Dansirima, P., Thiangviriya, S., Thaweelap, N., Suthummapiwat, A., Plerdsranoy, P., and Utke, R. (2018). Reversible hydrogen sorption and kinetics of hydrogen storage tank based on MgH_2 modified by TiF_4 and activated carbon. *International Journal of Hydrogen Energy*, 43(27), 12260-12270. doi:10.1016/j.ijhydene.2018.04.171.

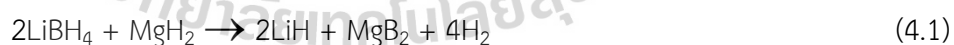


CHAPTER IV

RESULTS AND DISCUSSION

4.1 Compacted 2LiBH₄-MgH₂-ACNF

Dehydrogenation profiles of the compacted 2Li-MH and 2Li-MH-30% ACNF are characterized by simultaneous thermal analysis (STA) and mass spectroscopy (MS). From Figure 4.1(A), the DSC curve of 2Li-MH shows four endothermic peaks at 118, 291, 376, and 450 °C, corresponding to phase transformation of LiBH₄ (*o*- to *h*-LiBH₄), melting of LiBH₄, decomposition of MgH₂, and decomposition of LiBH₄, respectively. Meanwhile, the 2Li-MH-30% ACNF also shows four endothermic peaks at 120, 288, 336, and 431 °C (Figure 4.1(B)), in accordance with similar events as 2Li-MH. TGA and H₂-MS results of compacted 2Li-MH and 2Li-MH-30%ACNF reveal mainly two steps dehydrogenation. Decomposition temperature of MgH₂ and LiBH₄ of 2Li-MH reduce by 30 and 20 °C, respectively, after doping with ACNFs. Moreover, onset dehydrogenation temperature of 2Li-MH-30%ACNF is 275 °C, which is 85 °C lower than that of 2Li-MH (360 °C). With respect to theoretical dehydrogenation capacity of 2Li-MH of 11.4 wt.% H₂ according to equation (4.1), the total hydrogen contents desorbed from 2Li-MH and 2Li-MH-30% ACNF (5.31 wt.% and 6.51 wt.% H₂, respectively) are 46.60 and 57.10 % of theoretical capacity, respectively.



Significant reduction of dehydrogenation temperature and enhancement of hydrogen capacity suggest the improved kinetics of 2Li-MH after doping with ACNFs.

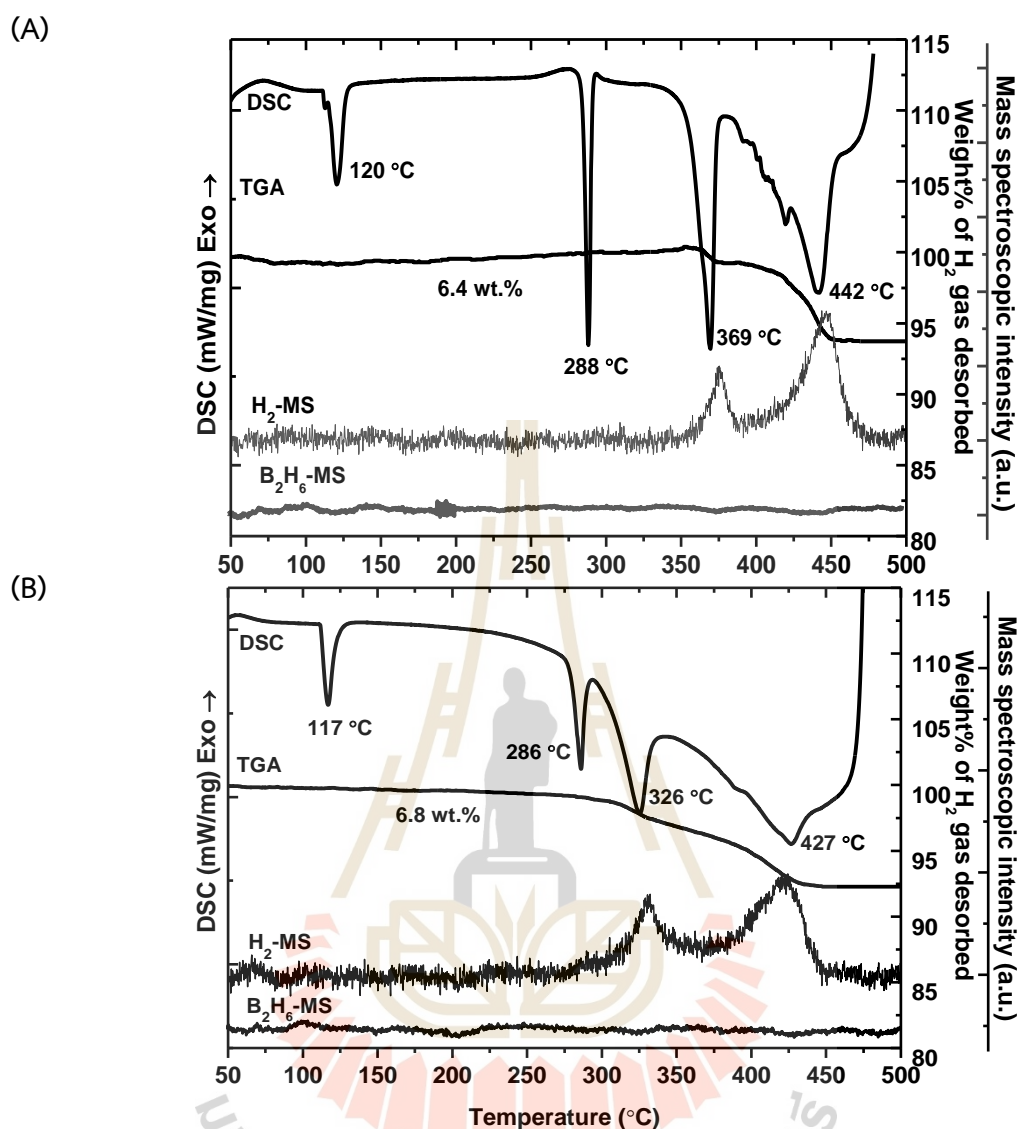
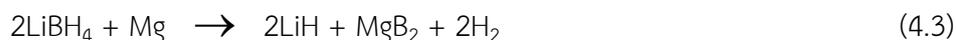


Figure 4.1 Simultaneous STA-MS results during dehydrogenation of 2Li-MH (A) and 2Li-MH-30% ACNF (B).

Furthermore, reversibility of compacted samples at 400 °C under 2 and 80 bar H₂ for dehydrogenation and rehydrogenation, respectively, was studied. From Figure 4.2, 2Li-MH releases hydrogen in one step during the 1st and 2nd cycles with capacity of 1.80 and 1.75 wt.%H₂, respectively. This dehydrogenation is mainly from MgH₂ (400 °C) with slightly LiBH₄, corresponding to the STA-MS results (Figure.4.2). In the case of 2Li-MH-30% ACNF, the 1st and 2nd cycles release hydrogen of 4.00 and 4.50 wt. % H₂, respectively, with two-step reaction, in accordance with equations (4.2) and (4.3) (Bösenberg et al., 2007 and Kim et al., 2015).



During the 1st step desorption (equation (4.2)), MgH₂ desorbs into Mg and H₂. Afterward, LiBH₄ reacts with Mg to produce LiH, MgB₂, and H₂ (equation (4.3)). It should be noted that the incubation period belonging to MgB₂ formation of the 2nd cycle is remarkably shorter than the 1st one. This is probably explained by the cracks due to pellet expansion and contraction during de/rehydrogenation (Table 4.1). This leads to the enhancement of hydrogen permeability through the pellet, benefiting hydrogen sorption kinetics of 2LiBH₄-MgH₂ system.

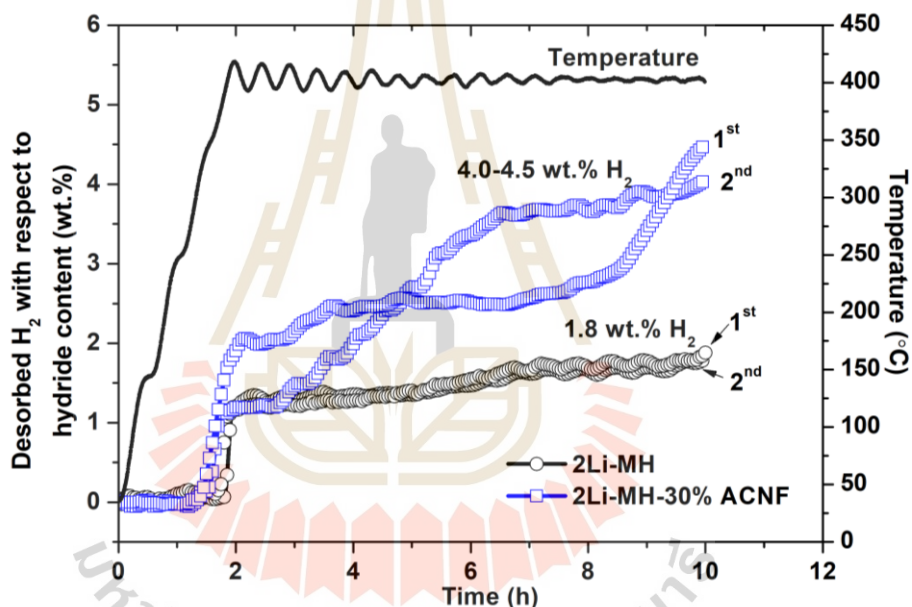
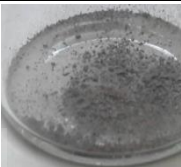
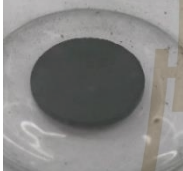
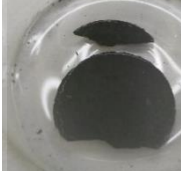


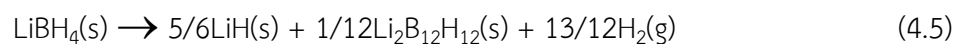
Figure 4.2 Dehydrogenation kinetics and reversibility of 2LiMH and 2Li-MH-30% ACNF.

Mechanical stability upon cycling of the pellet samples is further investigated. 2Li-MH-30%ACNF maintains its pellet shape with small cracks due to expansion and contraction during de/rehydrogenation, while 2Li-MH transforms to loose powder (Table 4.1). The fibrous structure of ACNFs probably plays an important role as reinforced frameworks for compacted 2Li-MH-30%ACNF. (Plerdsranoy et al., 2017 and Javadian et al., 2017).

Table 4.1 Photographs, thickness, and density of 2Li-MH and 2Li-MH-30% ACNF in as-prepared and rehydrogenated states.

samples	As-prepared		After Rehydrogenated	
	Compacted	Thickness (mm)		Density (g/cm ³)
2Li-MH		0.061	0.86	
2Li-MH-30%ACNF		0.055	0.93	

To study the de/rehydrogenation mechanisms, PXD and FTIR techniques are applied. From Figure 4.3(A)(a), as-prepared 2Li-MH reveals diffraction peaks of LiBH₄, hydrate LiBH₄ (Fang et al., 2010), and MgH₂ together with a small broad peak of MgO from oxidation with air during the experiment. After dehydrogenation, diffraction peaks of LiBH₄, MgH₂, Mg, LiH, and MgO are observed (Figure. 4.3(A)(b)). The appearances of LiBH₄ and MgH₂ refer to incomplete dehydrogenation of 2Li-MH. The formation of Mg and slight LiH is due to dehydrogenation of LiBH₄ and MgH₂ (equations (4.2) and (4.3)). After rehydrogenation, Figure 4.3(A)(c) reveals the diffraction peaks of LiBH₄ and MgH₂, corresponding to the reversibility of 2Li-MH. For FTIR results, all samples show strong vibrational peaks of B-H stretching and bending of LiBH₄ at 2389-2224 and 1126 cm⁻¹, respectively, (Thaweelap et al., 2017) together with O-H bending of oxygen and humidity during the experiment at 1635 cm⁻¹ (Figure 4.3(B)). For de/rehydrogenated 2Li-MH, the vibrational peaks of [B₁₂H₁₂]²⁻ from Li₂B₁₂H₁₂ (2486 cm⁻¹) (equation (4.5)) and B-O stretching of oxidized boron (B) (equation (4.4)) (1600-1300 cm⁻¹) are observed (Bösenberg et al., 2010) (Pitt et al., 2013).



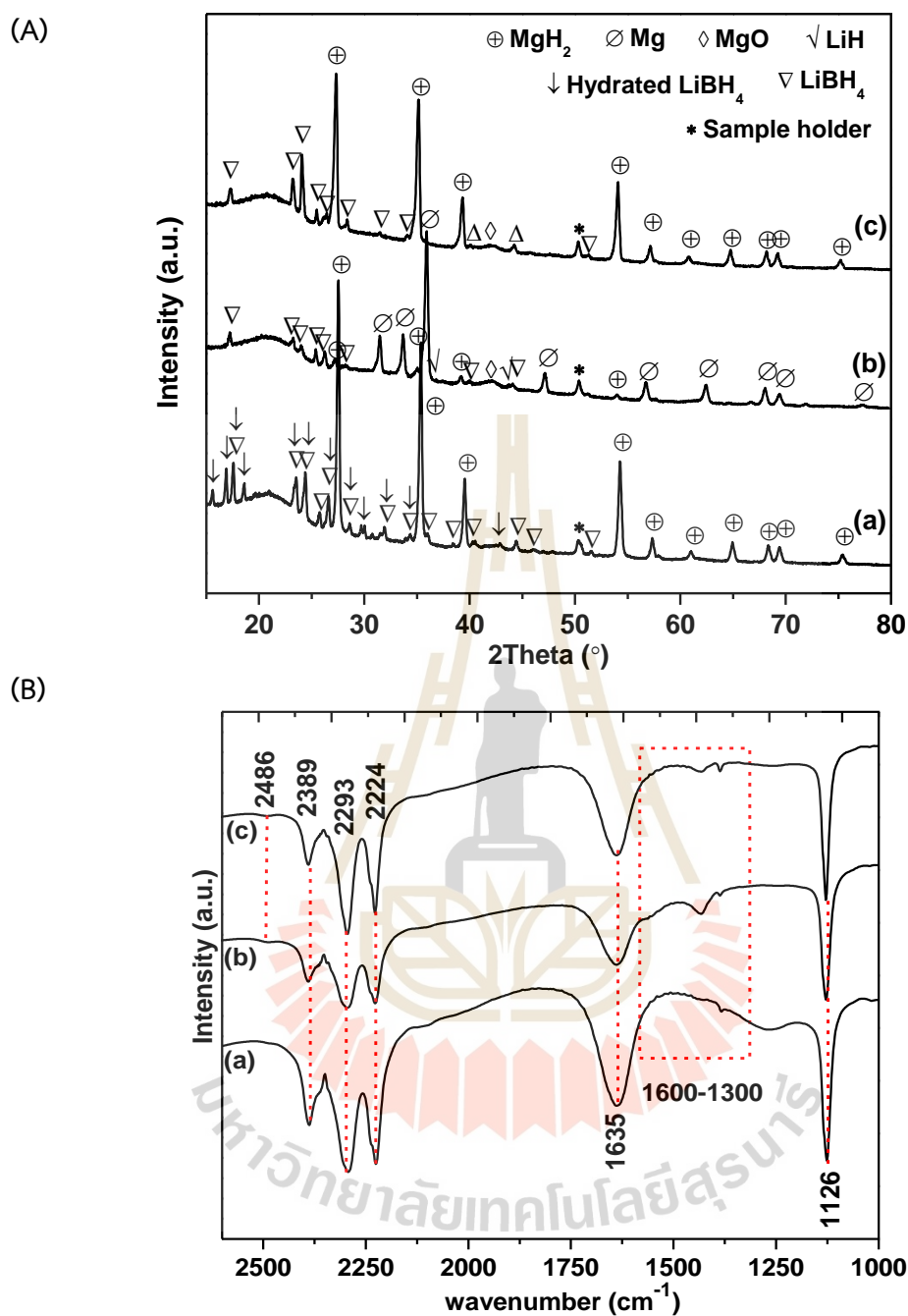


Figure 4.3 PXD (A) spectra of as-prepared and FTIR (B) spectra of as-prepared (a), dehydrogenated (b), and rehydrogenated (c) pellets of 2Li-MH.

For 2Li-MH-30%ACNF, the as-prepared sample shows the diffraction peaks of LiBH_4 , hydrated LiBH_4 , MgH_2 , and MgO (Figure 4.4(A)(a)). Dehydrogenated sample shows the diffraction peaks of MgB_2 , LiH , and MgO , suggesting successful dehydrogenation of LiBH_4 and MgH_2 (Figure 4.4(A)(b)). After rehydrogenation, the disappearance of LiBH_4 signals

(Figure 4.4(A)(c)) indicates nanoparticles or amorphous states probably due to melt infiltration into nanoporous ACNFs during the 1st dehydrogenation. The sharp peaks of MgO also appear due to the oxidation of Mg with oxygen and/or moisture. Furthermore, the FTIR results of all states of 2Li-MH-30%ACNF reveal the vibrations of B-H stretching and bending are found at 2389-2224 and 1126 cm⁻¹, respectively, together with O-H bending at 1635 cm⁻¹ (Figure 4.4(B)). After de/rehydrogenation, the vibration peaks of [B₁₂H₁₂]²⁻ from Li₂B₁₂H₁₂ and B-O stretching from oxidation of amorphous boron (a-B) at 2488 and 1600-1300 cm⁻¹, respectively, are observed (Bösenberg et al., 2010; Plerdsranoy et al., 2017; and Yan et al., 2011). The appearance of B-H stretching and bending of LiBH₄ after dehydrogenation indicates incomplete dehydrogenation reaction (Figure 4.4(B)(b)). After rehydrogenation, the vibrations of LiBH₄ suggest reversibility of LiBH₄ but incomplete reaction is obtained due to the formation of irreversible Li₂B₁₂H₁₂ and amorphous boron.

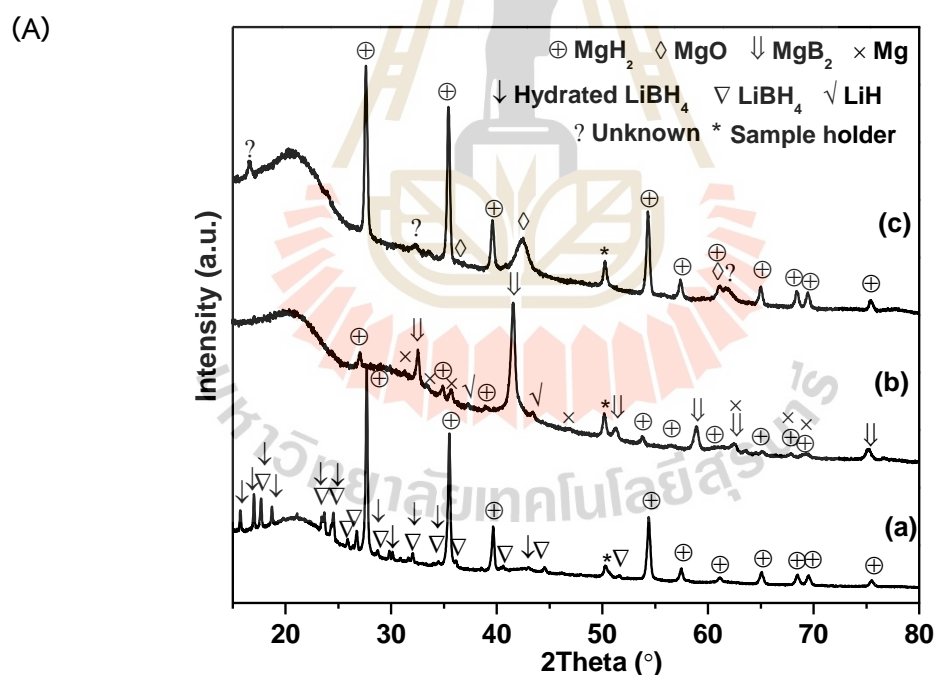


Figure 4.4 PXD (A) spectra of as-prepared (a), dehydrogenated (b), and rehydrogenated (c) of 2Li-MH-30%ACNF.

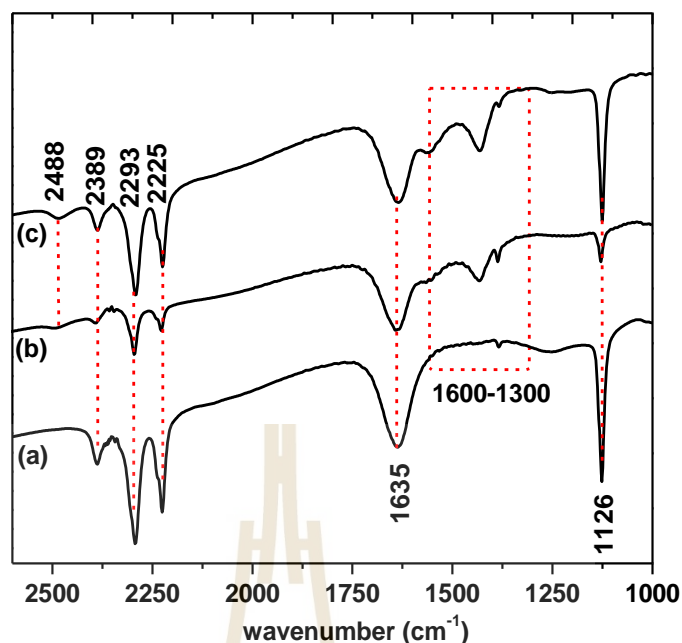


Figure 4.4 (Continued) FTIR (B) spectra of as-prepared (a), dehydrogenated (b), and rehydrogenated (c) of 2Li-MH-30%ACNF.

The activation energy (E_a) during dehydrogenation of 2Li-MH and 2Li-MH-30%ACNF was studied by DSC technique with different heating rates of 5, 10, 15, and 20 °C/min. DSC profiles of 2Li-MH and 2Li-MH-30%ACNF show the first endothermic peak at 288-297 °C belonging to the melting of h -LiBH₄. Three endothermic peaks at 338-396, 402.7-478, and 428.0-498 °C represent the dehydrogenation of MgH₂ as well as the 1st and 2nd steps of LiBH₄, respectively (Figure 4.5(A) and (C)). Based on the linear fitting of the Kissinger plot of 2Li-MH and 2Li-MH-30%ACNF (Figure 4.5(B) and (D)), the E_a is calculated from the slope of Kissinger plots. E_a during dehydrogenation of 2Li-MH is 250.6, 130.0, and 131.0 kJ/mol for dehydrogenation of MgH₂ as well as the 1st and 2nd steps of LiBH₄, respectively, while those of 2Li-MH-30%ACNF are 166.7, 103.9, and 124.6 kJ/mol, respectively. Significant reduction of E_a of 2Li-MH after doping with 30% ACNFs suggests the decrease of kinetic barrier, corresponding to the reduction of dehydrogenation temperature and results in Figures 4.1 and 4.2

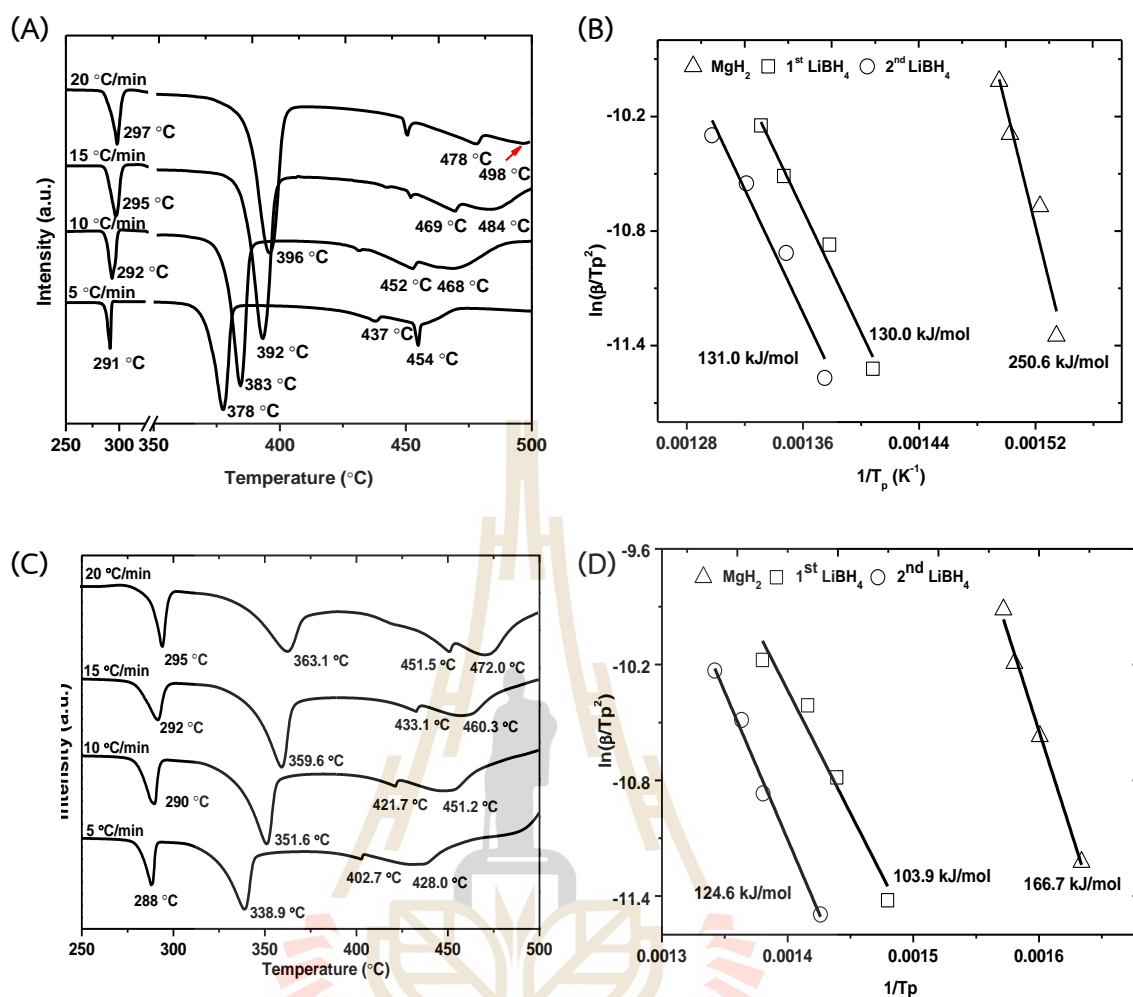


Figure 4.5 DSC curves with heating rates of 5-20 °C/min and the Kissinger plots of 2Li-MH ((A) and (B), respectively) and 2Li-MH-30%ACNF ((C) and (D), respectively).

Gas permeability measurements in the axial direction of compacted samples are carried out using the setup shown in Figure (3.13) of the experimental section (Sittiwet et al., 2017). The experiments are performed at room temperature (~ 30 °C) under vacuum to 6 bar H₂. From Figure 4.6, the experiments start with vacuum and ~ 5 -6 bar H₂ at downstream and upstream chambers, respectively. For 2Li-MH, the pressure at the upstream chamber (P_u) decreases with the increase of the downstream chamber (P_d) and stable pressure is found after about 500 min. In the case of 2Li-MH-30% ACNF, P_u and P_d change rapidly within about 80 min, significantly faster than that of 2Li-MH (Figure 4.6(A)). Figure 4.6(B) shows the linear plot between $\ln(P_u - P_d / P_{u,0} - P_{d,0})$ versus time (t) and α is obtained by slop of this plot. The hydrogen permeability (k) can be

calculated using α and equation (3.6). 2Li-MH and 2Li-MH-30%ACNF show α values of 0.00099 and 0.000088 s^{-1} , respectively, in accordance with hydrogen permeability of 1.56×10^{-18} and $1.49 \times 10^{-17} m^2$, respectively (inset of Figure 4.6(B)). Hydrogen permeability of 2Li-MH increases significantly after doping with 30% ACNFs. This can be explained by phase boundaries between hydride and ACNFs providing small void space for hydrogen diffusion. This leads to the improvement of dehydrogenation kinetics of hydride composite (Sitthiwet et al., 2017).

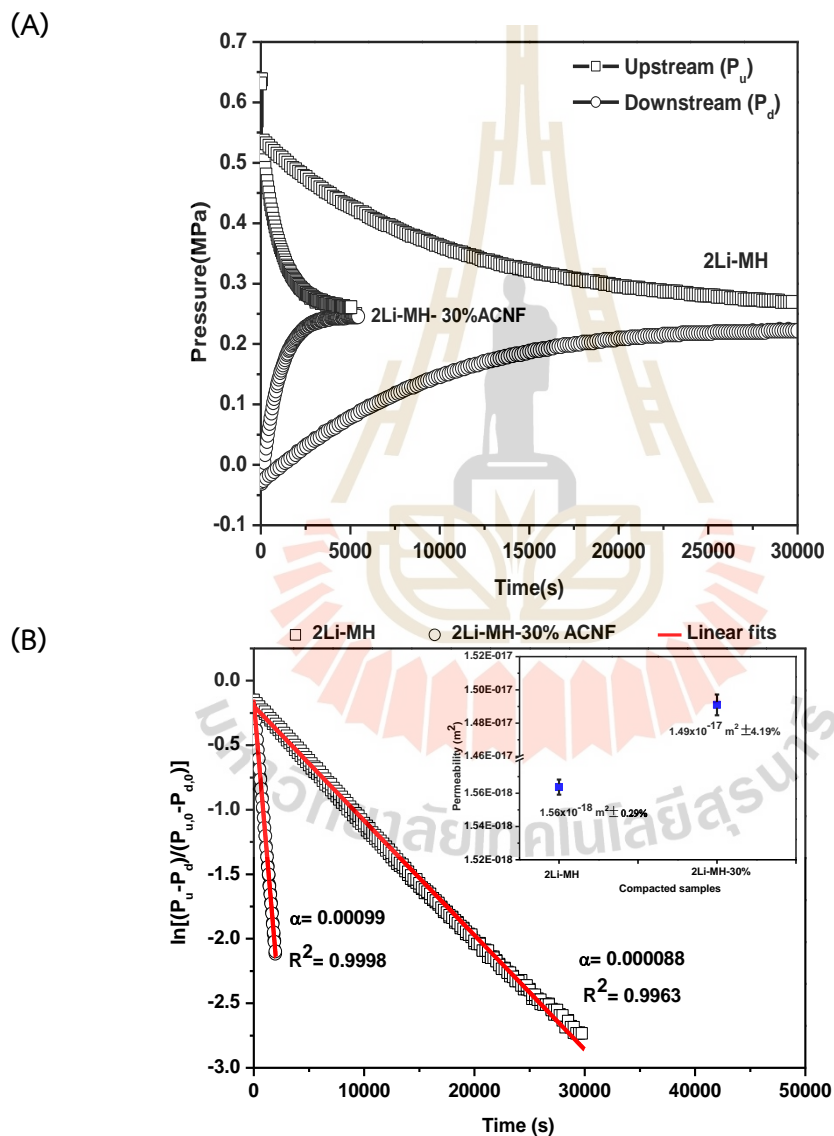


Figure 4.6 P_u and P_d versus time (A) and hydrogen permeability (B) of 2Li-MH and 2Li-MH-30%ACNF.

The thermal properties of 2Li-MH and 2Li-MH-30% ACNF, including thermal conductivity, thermal diffusivity, and specific heat capacity are characterized. The measured thermal conductivity of 2Li-MH and 2Li-MH-30% ACNF are $1.64 \pm 0.34\%$ and $1.67 \pm 0.40\%$ $\text{Wm}^{-1}\text{K}^{-1}$, respectively. From the previous work of the compacted hydride bed with expanded natural graphite (ENG), ENG led to the improvement of anisotropy thermal conductivity (along ENG alignment) (Chaise et al., 2009 and Pohlmann et al., 2010). In our work, thermal conductivity slightly increases after doping with ACNFs due to the homogeneous orientation of ACNFs in the pellet sample. Thermal diffusivity and specific heat capacity of compacted 2Li-MH are $0.20 \pm 0.10\%$ mm^2s^{-1} and $8.16 \pm 0.33\%$ $\text{MJ/m}^3\text{K}$, while those of 2Li-MH-30%ACNF are $0.33 \pm 0.33\%$ mm^2s^{-1} and $5.04 \pm 0.40\%$ $\text{MJ/m}^3\text{K}$, respectively. Considering the equation $\alpha = k/\rho C_p$, where α , k , ρ , and C_p are thermal diffusivity, thermal conductivity, density, and specific heat capacity, respectively, the higher the thermal diffusivity the lower the specific heat capacity. Therefore, heat transfer 2Li-MH of pellet is significantly improved by the addition of 30% ACNFs. Thus, the enhancement of hydrogen sorption kinetics and reversibility of 2Li-MH-30%ACNF is due to the improvement of not only hydrogen permeability but also heat transfer (Chaise et al., 2009; Plerdsranoy et al., 2017; Javadian, et al., 2017; Pohlmann et al., 2013; Shim et al., 2014).

Table 4.2 Thermal conductivity, thermal diffusivity, and specific heat capacity of compacted 2Li-MH and 2Li-MH-30% ACNF.

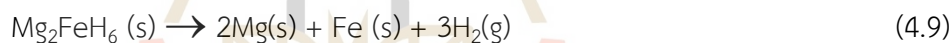
Samples	Thermal Conductivity (W/mK)	Thermal Diffusivity (mm^2/s)	Specific Heat Capacity ($\text{MJ/m}^3\text{K}$)
2Li-Mg	$1.64 \pm 0.34\%$	$0.20 \pm 0.10\%$	$8.16 \pm 0.33\%$
2Li-MH-30%ACNF	$1.67 \pm 0.40\%$	$0.33 \pm 0.33\%$	$5.04 \pm 0.40\%$

4.2 Ni-doped Mg₂FeH₆

Phase compositions of as-prepared Mg₂FeH₆ with and without Ni are characterized by in situ SR-XRD and Rietveld refinement method (Figure 4.7). As-prepared Mg₂FeH₆ shows the diffraction peaks of Mg₂FeH₆ and slight MgH₂ (Figure 4.7 (A)), indicating successful synthesis of Mg₂FeH₆ according to equation (4.7) (Polanski et al., 2019 and Zhao et al., 2014).



For as-prepared 5%Ni-Mg-Fe, the diffraction peaks of Mg₂FeH₆, Mg₂NiH₄, MgH₂, Mg₂NiH_{0.3}/Mg₂Ni, Mg, and Fe/Ni are observed (Figure 4.7(B)). The formation of Mg₂Ni, Mg, and Fe is due to partial dehydrogenation of Mg₂NiH₄ (equation (4.8)) and Mg₂FeH₆ (equation (4.9)), respectively. As-prepared 20%Ni-Mg-Fe reveals similar diffractions (Mg₂FeH₆, Mg₂NiH₄, MgH₂, and Fe) with the sample with 5% wt. % Ni as well as FeNi₃ (Figure 4.7(C)).



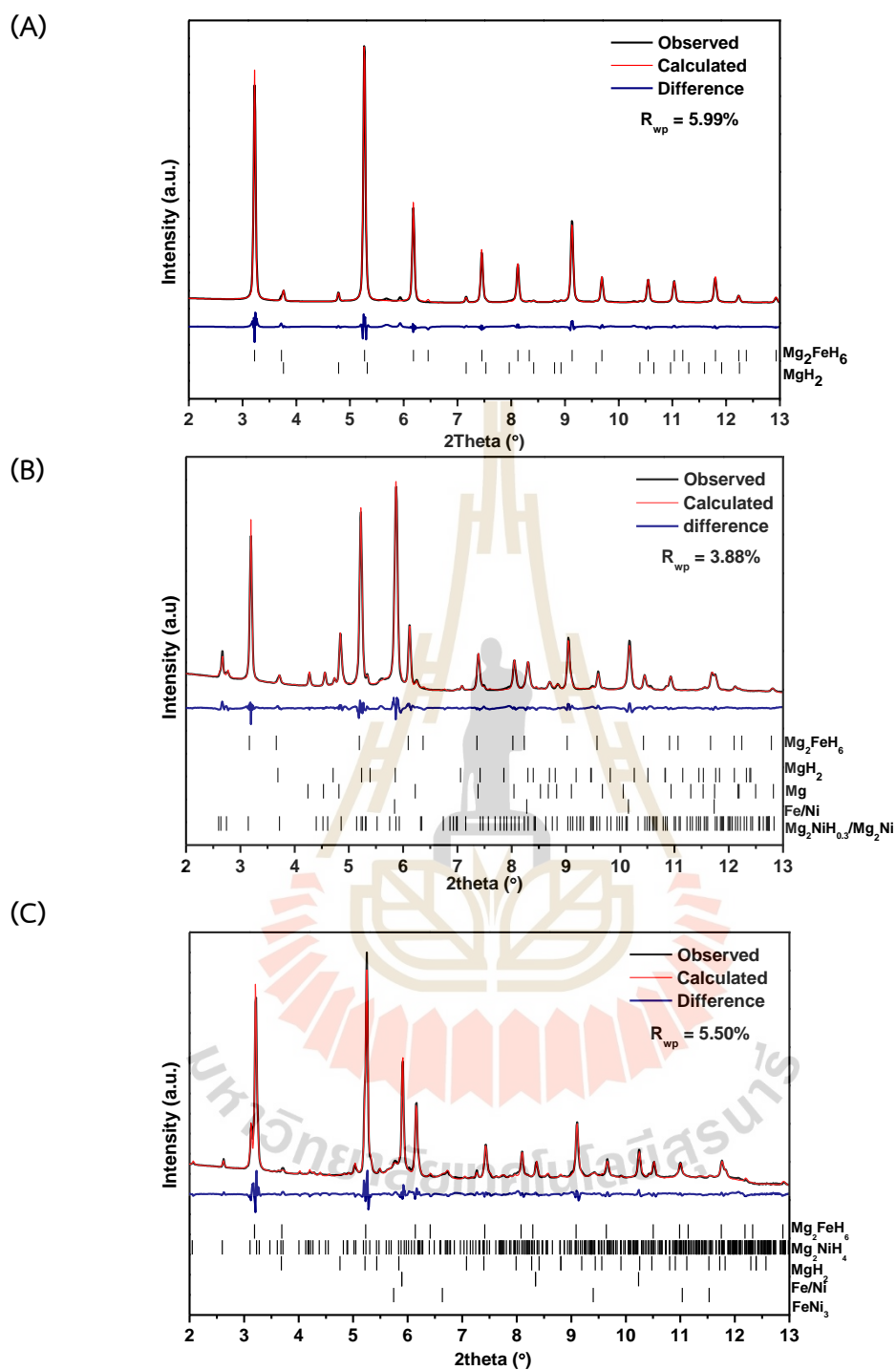


Figure 4.7 Rietveld refinement of SR-PXD results of as-prepared Mg_2FeH_6 (A), 5%Ni-Mg-Fe (B), and 20%Ni-Mg-Fe (C).

In addition, Table 4.3 summarizes the phase compositions and quantities in all as-prepared samples calculated from the Rietveld refinement software. High quantity

of Mg_2FeH_6 in as-prepared Mg_2FeH_6 (92.6 wt.%) suggests an effective preparation method of high energy ball milling and heat treatment under high temperature and hydrogen pressure (Katarzyna et al., 2018, Nyamsi et al., 2018 and Li et al., 2018). For the samples doped with Ni, the content of Mg_2FeH_6 decreases due to Mg_2NiH_4 formation and partial dehydrogenation during sample preparation. It is found that the higher the Ni-loading content, the more the effectiveness of Mg_2NiH_4 formation.

Table 4.3 Phase compositions and quantities in as-prepared samples were determined by Rietveld refinement

Sample	Phase	Space group	wt %
Mg-Fe (Rwp : 5.99%)	Mg_2FeH_6	Fm-3m	92.6
	MgH_2	P42/mnm	7.4
5%Ni-Mg-Fe (Rwp : 3.88%)	Mg_2FeH_6	Fm-3m	61.5
	$\text{Mg}_2\text{NiH}_{0.3}$	P6222	10.6
	Mg_2Ni		
	MgH_2	P42/mnm	6.2
	Fe/Ni	Im-3m	10.6
	Mg	P63/mmc	11.1
20%-Ni-Mg-Fe (Rwp : 5.50%)	Mg_2FeH_6	Fm-3m	48.8
	Mg_2NiH_4	C2/C	31.8
	Fe/Ni	Im-3m	12.1
	FeNi_3	Fm-3m	7.3

Dehydrogenation kinetics and hydrogen storage capacity of as-prepared Mg_2FeH_6 , 5%Ni-Mg-Fe, and 20%Ni-Mg-Fe are characterized by sievert-type apparatus by heating from room temperature to 330 °C under 0.1 bar H_2 . From Figure 4.8, Mg_2FeH_6 reveals single-step dehydrogenation with onset temperature at 250 °C and hydrogen capacity of 5.40 wt.%. 5%Ni-Mg-Fe and 20%Ni-Mg-Fe show two-step dehydrogenation at 170 and 220-275 °C with total hydrogen capacity of 2.83 and 3.70 wt.%, respectively. These correspond to the dehydrogenation of Mg_2NiH_4 and Mg_2FeH_6 , respectively.

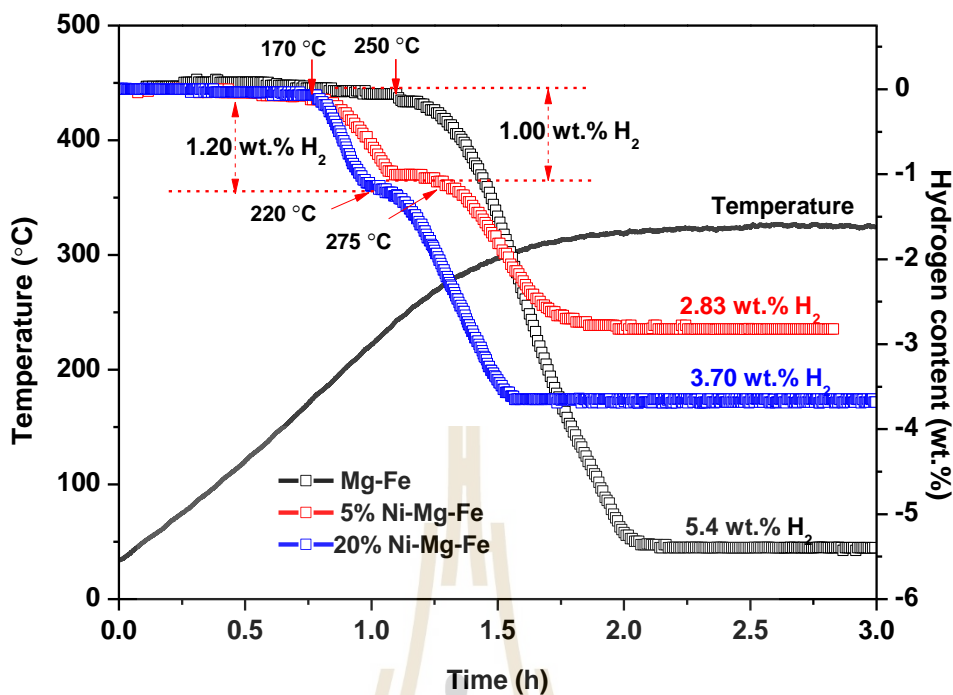


Figure 4.8. First hydrogen desorption kinetics at 330 °C under 10 kPa of pure Mg-Fe, 5%Ni-Mg-Fe, and 20%Ni-Mg-Fe.

Furthermore, dehydrogenation pathways of as-prepared samples are investigated by the in situ SR-XRD technique. The samples are heated under 1 bar Ar from room temperature to 400 °C and kept at the isothermal condition for 30 min. To clearly explain the mechanisms during dehydrogenation, the diffraction intensity versus temperature is plotted. From Figure 4.9, as-prepared Mg_2FeH_6 begins to decompose into Mg and Fe at 300 °C and completes at 370 °C (equation (4.9)) (Khan et al., 2020; Polanski et al., 2010).

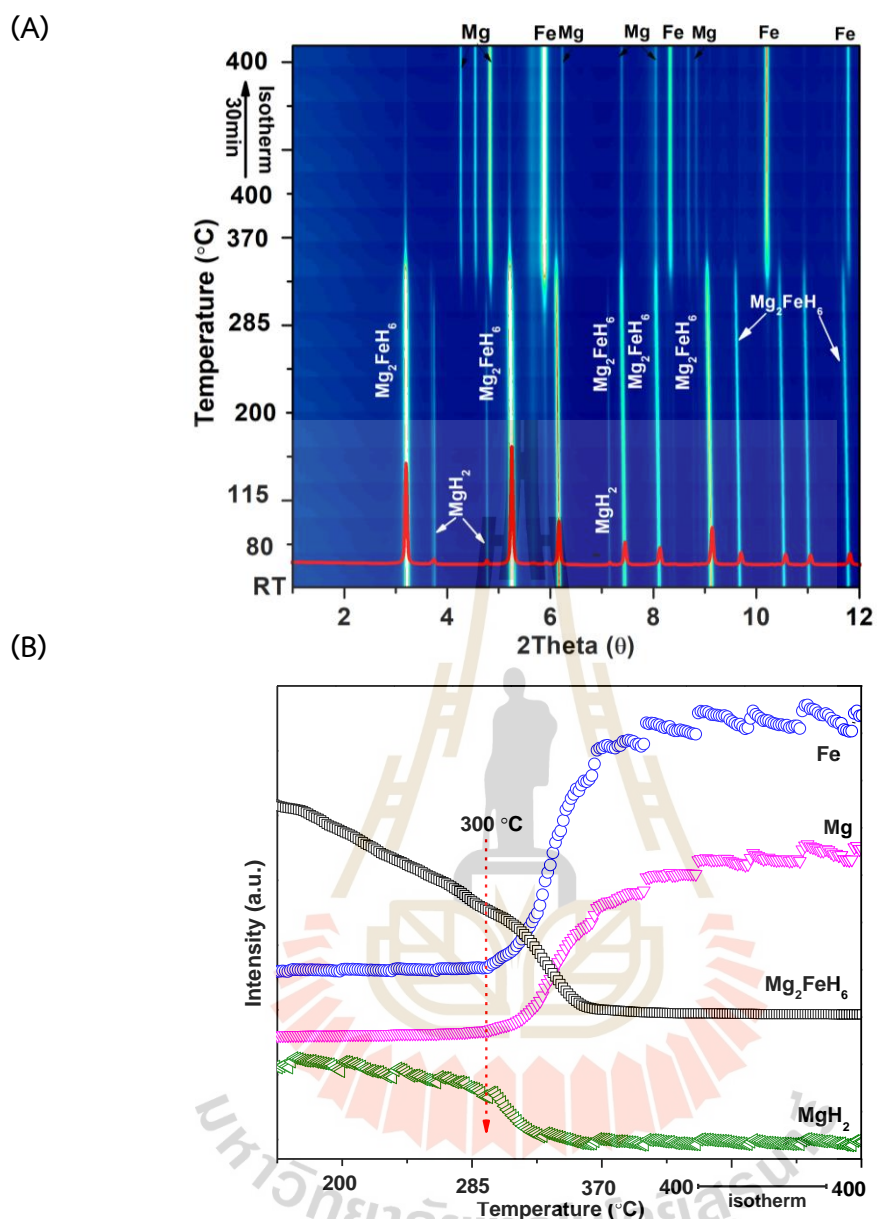


Figure 4.9 In situ SR-XRD spectra of as-prepared Mg_2FeH_6 (A) and peak intensities versus temperature (B).

For 5%Ni-Mg-Fe, $\text{Mg}_2\text{NiH}_{0.3}$ desorbs into Mg_2Ni (equation (4.10)) at 170 °C as well as MgH_2 and Mg_2FeH_6 into Fe and Mg (equations (4.11) and (4.9)) together with the formation of MgO due to the oxidation of Mg-containing phase with air and humidity (Figure 4.10) (Kalinichenka et al., 2011, de Rango et al., 2020 and Luo et al., 2015). Afterward, Mg reacts with Ni to form Mg_2Ni at 325 °C. the dehydrogenation products are Mg_2Ni , Mg, and Fe.

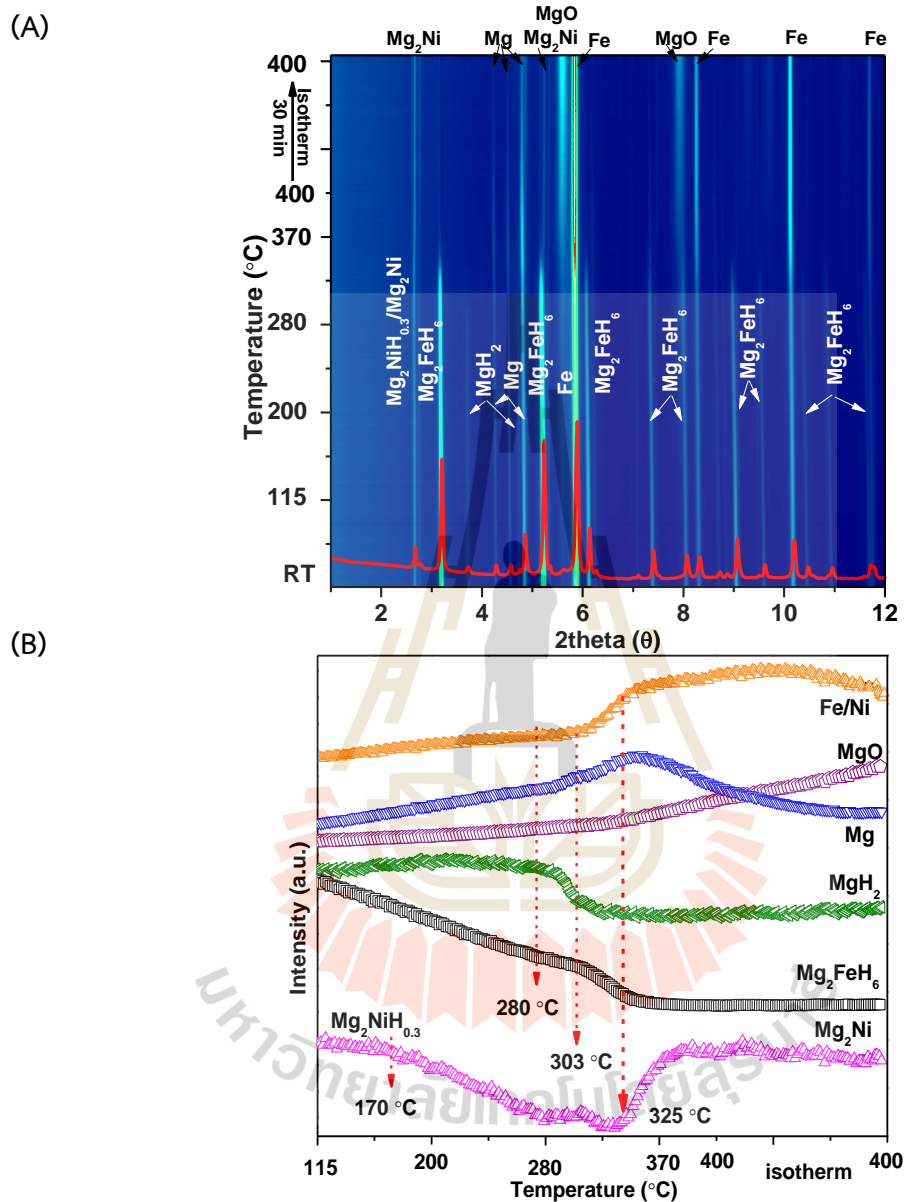


Figure 4.10 In situ SR-XRD spectra of 5%Ni-Mg-Fe (A) and peak intensities versus temperature (B).

In the case of 20%Ni-Mg-Fe, Mg_2NiH_4 decomposes into Mg_2Ni at 200 °C (equation (4.8)) together with the formation of a new phase of $\text{Mg}_2\text{FeH}_6^*$ (Figure 4.11). At 200-320 °C, Mg_2FeH_6 and $\text{Mg}_2\text{FeH}_6^*$ desorb into Mg, Fe, and Mg_2Ni (equations (4.9) and (4.12)) and Fe further reacts with Ni to form FeNi_3 . Partial substitution of Ni for Fe in Mg_2FeH_6

is expected that due to their comparable atomic sizes. XANES and EXAFS techniques are applied to investigate the local environment of Ni atoms in 20%Ni-Mg-Fe to confirm this substitution (Figure 4.12). Moreover, the formation of FeNi_3 benefits dehydrogenation kinetics of Mg_2FeH_6 due to its catalytic effects of FeNi_3 (Chen et al., 2016) and Chen et al., 2018).

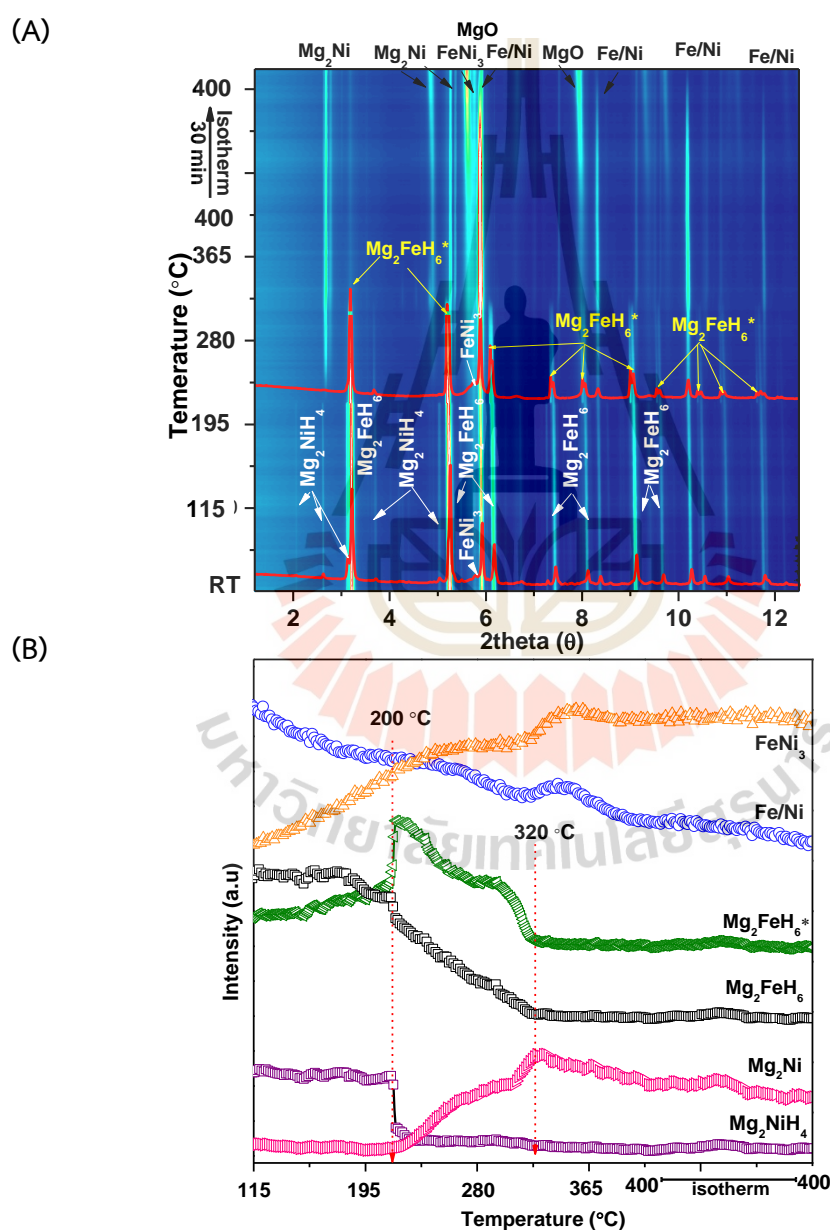


Figure 4.11 In situ SR-XRD spectra of 20%Ni-Mg-Fe (A) and Peak intensities versus temperature (B).

To investigate the local coordination environment of Ni atoms in $\text{Mg}_2\text{FeH}_6^*$ of 20%Ni-Mg-Fe, x-ray absorption (XAS) is applied. $\text{Mg}_2\text{FeH}_6^*$ is prepared by heating as-prepared 20% Ni-Mg-Fe to 235 °C under 1 bar H_2 , dwelling at 235 °C for 10 min, and cooling to room temperature. Based on the previous study using DFT calculation, the optimized lattice constant and Mg-H distance were enhanced. The optimized lattice constant (a) and Mg-H distance of Mg_2FeH_6 increased from 6.418 to 6.442 Å and from 2.269 to 2.276 Å, respectively, when Ni substitution for Fe in Mg_2FeH_6 to form $\text{Mg}_2\text{Fe}_{0.75}\text{Ni}_{0.25}\text{H}_6$ was proposed. (Batalovic et al., 2014). In our work, $\text{Mg}_2\text{Fe}_{0.75}\text{Ni}_{0.25}\text{H}_6$ is used as a model to fit the Ni K-edge EXAFS spectra of $\text{Mg}_2\text{FeH}_6^*$. The fitting result in the k -space shows a perfect match with the model (Figure 4.12(A)). From the fitting result in R -space, radial distances of the scattering paths in the first shell including Ni-H1 and Ni-Mg are 1.49 and 2.73 Å, respectively, while those of the second shell of Ni-H2, Ni-Ni, and Ni-Fe are 3.74, 4.27, and 4.76 Å, respectively (Figure 4.12(B)) and Table 4.4.). The calculated coordination numbers of Ni-H1, Ni-Mg, Ni-H2, Ni-Ni, and Ni-Fe paths are 4.41, 5.52, 16.56, 2.07, and 6.21, respectively. The R -factor value indicates the reliability and quality of the fitting between data and model. The smaller the R -factor, the better the fitting results. The R -factor value of this study is 0.0474, corresponding to the acceptable R -factor for good fitting (<0.05). (Newville et al., 2005 and Pinitsoontorn et al., 2014). Moreover, comparable radial distances of Ni-H1 and Ni-Mg (1.49 and 2.73 Å, respectively) (Table 4.4) to those of Fe-H and Fe-Mg of Mg_2FeH_6 (1.51 and 2.74 Å, respectively) (Zhang et al., 2013), confirm the Ni substitution for Fe in Mg_2FeH_6 to form $\text{Mg}_2\text{Fe}_{0.75}\text{Ni}_{0.25}\text{H}_6$. Thus, $\text{Mg}_2\text{Fe}_{0.75}\text{Ni}_{0.25}\text{H}_6$ phase is detected after dehydrogenation of Mg_2NiH_4 and reduction of Mg_2FeH_6 at 200-228 °C (Figure 4.11(B)) is likely obtained from the reaction between Mg_2Ni , Mg_2FeH_6 , and H_2 (equation (4.13)). Afterwards, $\text{Mg}_2\text{Fe}_{0.75}\text{Ni}_{0.25}\text{H}_6$ dehydrogenates into Mg_2Ni , Fe, and Mg at 228-320 °C (equation (4.14)) (Figure 4.11(B)). DFT calculation suggested that such Ni substitution resulted in the increment of unit cell volume and Mg-H distance of Mg_2FeH_6 as well as the significant reduction of desorption enthalpy of Mg_2FeH_6 from 39.4 to 27.7 kJ/mol H (Batalovic et al., 2014). This is in good agreement with the observed reduction of dehydrogenation temperature (30-55 °C) and greater hydrogen storage capacity (up to 0.85 wt. % H_2) of 20% Ni-Mg-Fe with respect to Mg_2FeH_6 and 5% Ni Mg-Fe (Figure 4.8).



Furthermore, the oxidation state of Ni in $\text{Mg}_2\text{Fe}_{0.75}\text{Ni}_{0.25}\text{H}_6$ is investigated by Ni K-edge XANES technique. From Figure 4.12(C), Ni K-edge XANES spectrum of standard NiO (Ni^{2+}) shows the absorption edge at ~ 8340 eV assigned to $1s$ to $4p$ transition and the strong white line at ~ 8350 eV (Hoffmann et al., 1999), while metallic Ni (Ni^0) reveals the absorption edge at a lower energy of 8333 eV. For Ni K-edge XANES spectrum of $\text{Mg}_2\text{Fe}_{0.75}\text{Ni}_{0.25}\text{H}_6$, the absorption edge energy at 8336 eV is detected. This slight increment of absorption edge energy with respect to Ni^0 (3 eV) implies the increase of Ni oxidation state, corresponding to the oxidation state of $\text{Ni}^{0.5+}$ in $\text{Mg}_2\text{Fe}_{0.75}\text{Ni}_{0.25}\text{H}_6$ (Figure 4.12(C)).

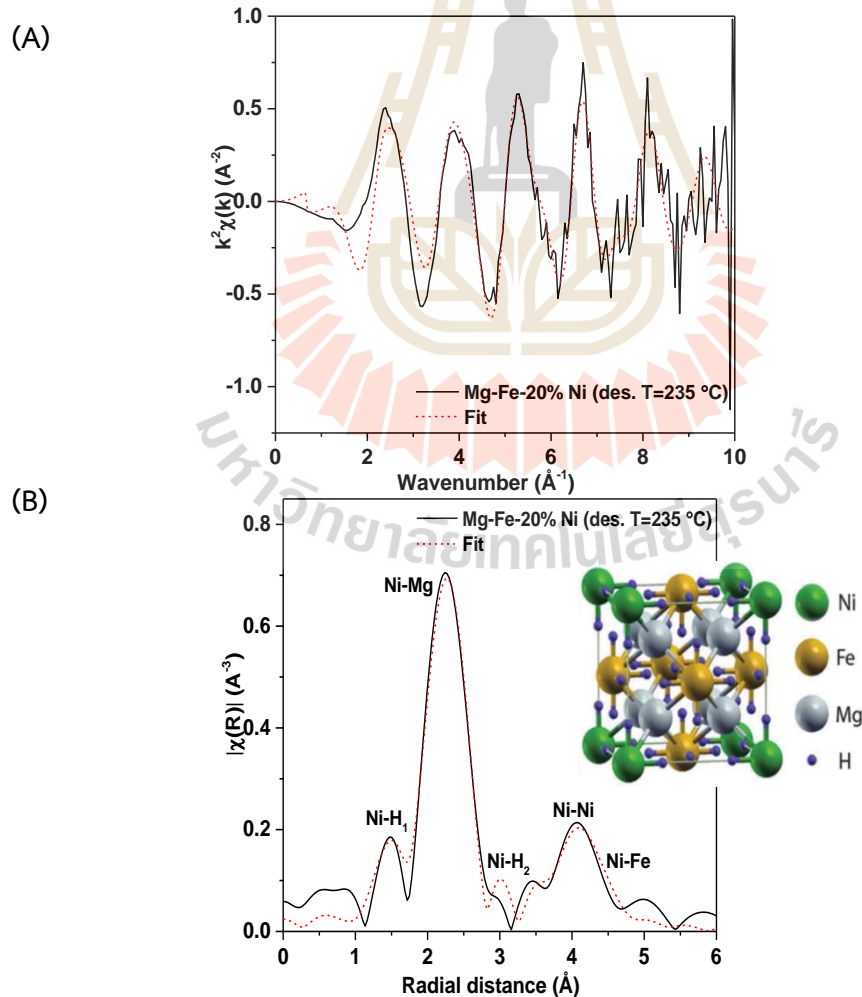


Figure 4.12 Ni K-edge EXAFS data and model fitting in k -space (A) and R -space (B) as well as unit cell structure (inset of (B)).

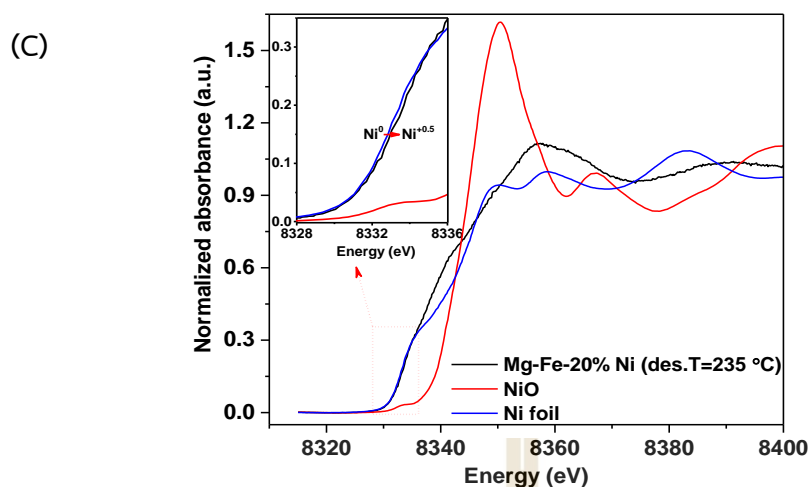


Figure 4.12 (Continued) Ni K-edge XANES spectrum of $\text{Mg}_2\text{Fe}_{0.75}\text{Ni}_{0.25}(\text{C})$. (Batalovic et al., 2014)).

Table 4.4 Scattering paths, coordination number, the path range (R), the mean squared displacement (σ^2) and R -factor extracted from the fitted data for Ni atoms substituted in Mg_2FeH_6 of 20%Ni-Mg-Fe.

Samples	Scattering path	coordination number	$R(\text{\AA})$	σ^2	R -Factor
$\text{Mg}_2\text{Fe}_{0.75}\text{Ni}_{0.25}$ (Ni K-edge EXAFS)	Ni-H1	4.41	1.49	0.031	0.0474
	Ni-Mg	5.52	2.73	0.013	
	Ni-H2	16.56	3.74	0.004	
	Ni-Ni	2.07	4.27	0.101	
	Ni-Fe	6.21	4.76	0.022	
Mg_2FeH_6 (Zhang et al., 2013) (Fe K-edge EXAFS)	Fe-H	6	1.51	-	-
	Fe-Mg	8	2.74	-	

The dehydrogenation kinetics and reversibility of Mg_2FeH_6 with and without Ni addition are measured at 330 °C under 0.1 bar and 40 bar H_2 for dehydrogenation and rehydrogenation, respectively. From Figure 4.13(A), Mg_2FeH_6 releases 5.40 and 4.20

wt.% H₂ during the 1st and 2nd cycles, respectively, at onset temperature of 250 °C and 209 °C, respectively. 5%Ni-Mg-Fe starts to release hydrogen at 170-205 °C together with the hydrogen capacities of 2.85-3.83 wt.% for cycling 1st-4th (Figure 4.13(B)). For 20%Ni-Mg-Fe, dehydrogenation begins at 170 – 207 °C with hydrogen capacities of 3.70 and 2.96-3.15 wt.% for the 1st and 2nd-4th cycles, respectively (Figure 4.13(C)). After doping with Ni, dehydrogenation temperature of Mg₂FeH₆ decreases together with the improved kinetics and cycling stability.

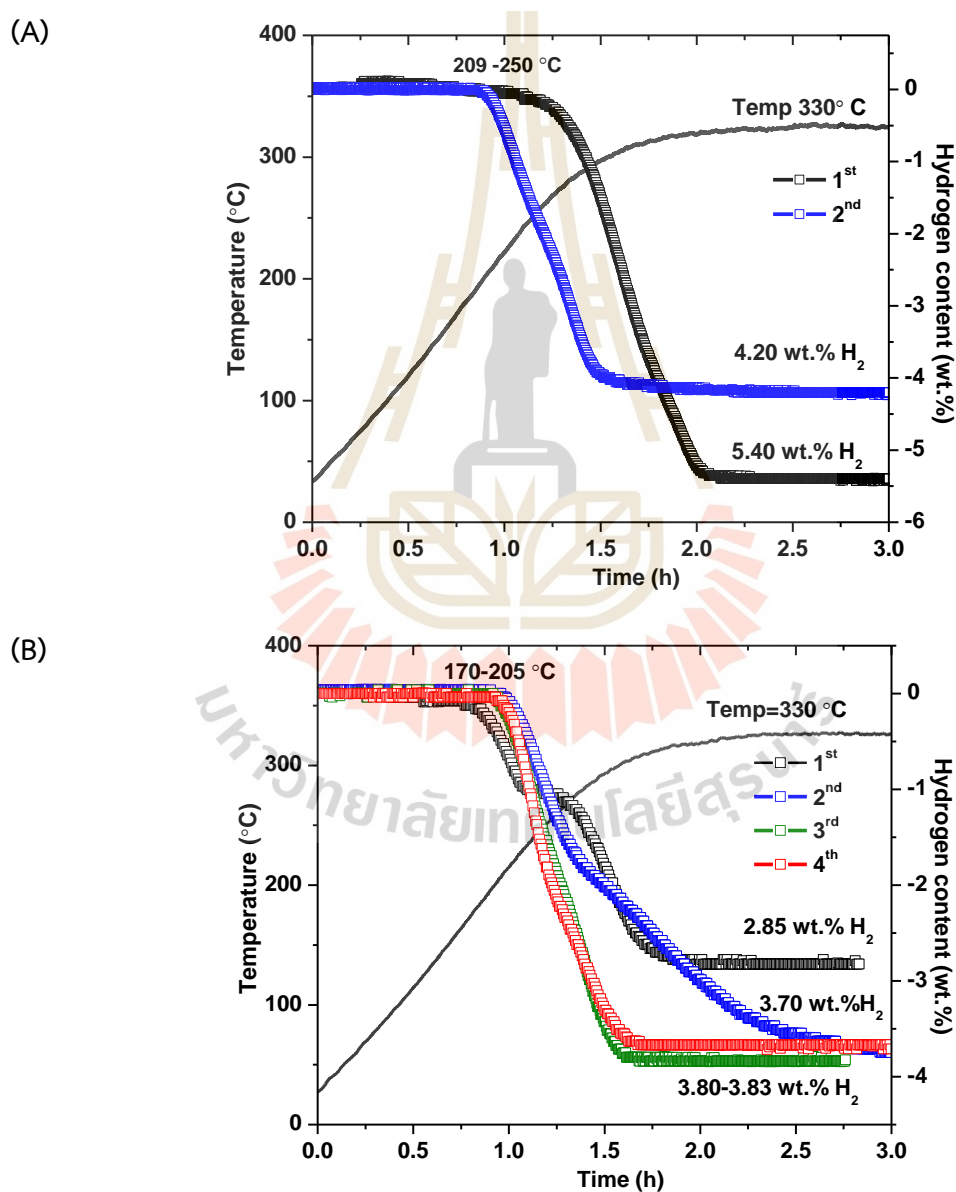


Figure 4.13 Dehydrogenation kinetics and reversibility under vacuum at 330 °C of Mg₂FeH₆ (A) and 5%Ni-Mg-Fe (B).

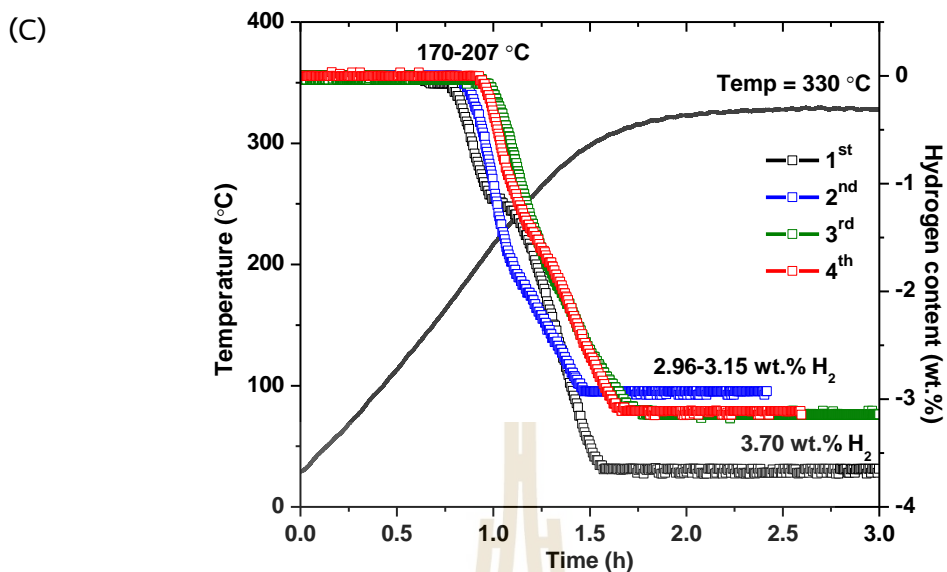


Figure 4.13 (Continued) Dehydrogenation kinetics and reversibility under vacuum at 330 °C of 20%Ni-Mg-Fe (C).

4.3 MgH₂-TiF₄-MWCNT hydrogen storage tank

Successful hydrogenation of MgH₂ and dehydrogenation performance of as-prepared MgH₂ and as-prepared MH-TiF₄-MWCNT are confirmed by PXD and STA-MS techniques. Figure 4.14(A) shows the diffraction peaks of MgH₂ and a small amount of residual Mg. This indicates successful hydrogenation of Mg to MgH₂. Dehydrogenation of as-prepared MH-TiF₄-MWCNTs reveals onset and main temperature at 350 and 388 °C, respectively, (Figure 4.14(B)) which are significantly lower than those of pure MgH₂ ($\Delta T=138$ and 109 °C, respectively) (Thongtan et al., 2018) together with storage capacity of 4.1wt.% H₂. This can be due to incomplete hydrogenation of Mg to MgH₂ (Figure 4.14(B)).

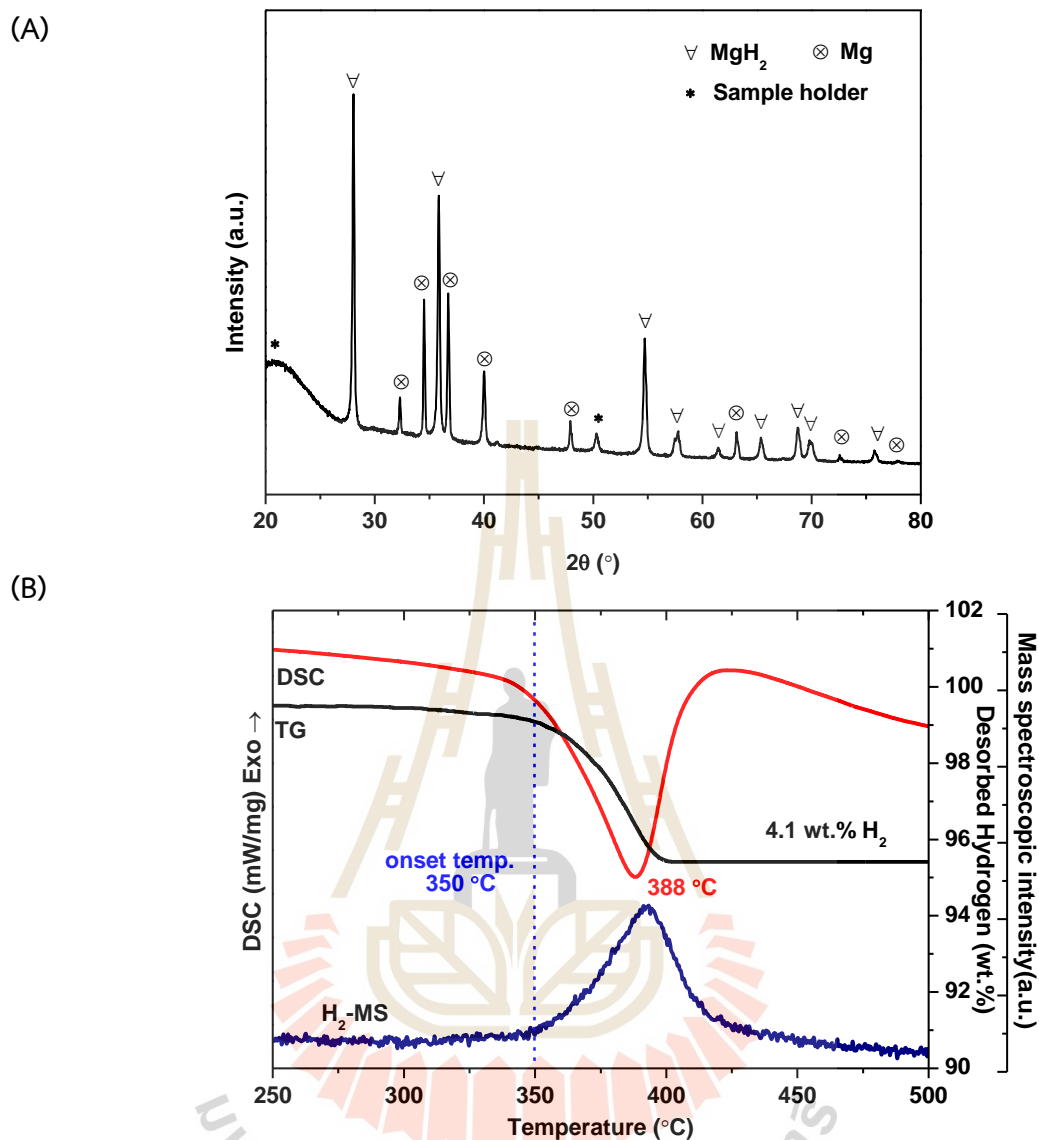


Figure 4.14 PXD (A) and STA-MS (B) results of as-prepared MH-TiF₄-MWCNT.

Furthermore, dehydrogenation of MH-TiF₄-MWCNT based hydrogen storage tank is characterized under isothermal at setting temperature (T_{set}) of 300 °C with the initial pressure of 10.6 bar H₂. Upon hydrogen release from the tank, dehydrogenation begins shown as temperature reduction from the initial temperatures (308-317 °C) to the equilibrium temperature (T_{eq}) of 293-299 °C (TC1-TC5) due to endothermic reaction (Figure 4.15). In the meantime, hydrogen desorbs and flows through the mass flow meter with a flow rate of 0.3 standard L/min (SLM) under ~1.2 bar H₂. After 30 min, the hydrogen flow rate slightly decreases together with the elevated all temperatures at all positions inside the tank. It is found that TC1 and TC2 show the longest plateau

range during endothermic dehydrogenation due to good hydrogen permeability at the positions near H₂ in/outlet. Total hydrogen volume and capacity of 29.70 SL and 5.5 wt.% H₂, respectively, are achieved. (Figure 4.15(A)).

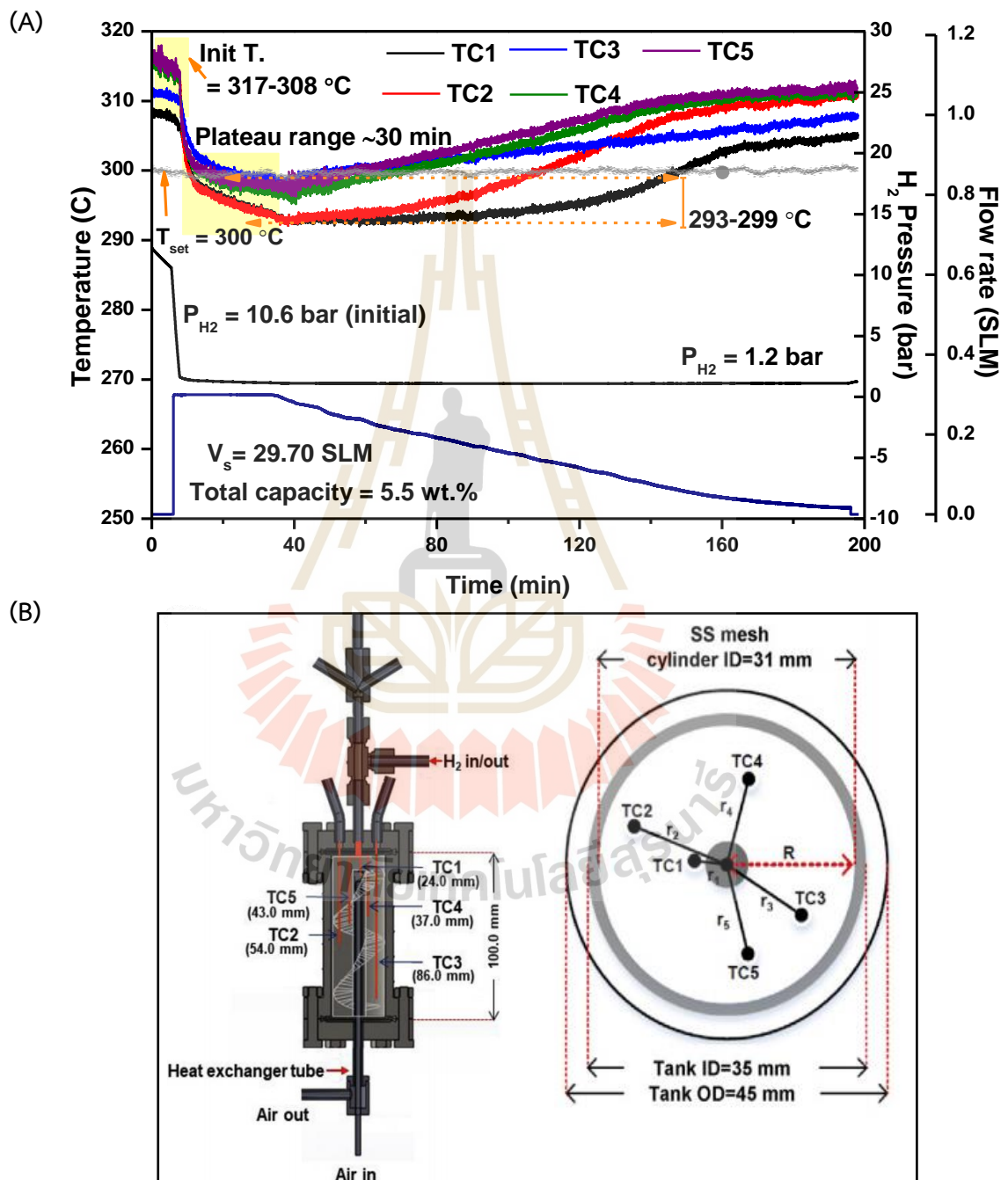


Figure 4.15 Dehydrogenation of MH-TiF₄-MWCNT based tank at isothermal condition ($T_{\text{set}} = 300 \text{ }^{\circ}\text{C}$ under 1.2 bar H₂) (A) and radial directions of the tank (B).

After dehydrogenation, hydrogenation is done by reducing T_{set} to 250 °C and applying 10-16 bar H_2 with compressed air flow of 3 L/min (heat exchanger). From Figure (4.16), temperatures at all positions in the tank increase rapidly to T_{eq} of 340-390 °C, corresponding to P_{eq} of 10-16 bar (Chaise et al., 2010; and Garrier et al., 2013). Different T_{eq} values indicate inhomogeneous hydrogenation performance probable due to poor hydrogen permeability and thermal conductivity. TC1 locating near the cooling tube displays a longer plateau temperature with greater T_{eq} than others (TC2-TC4) due to effective heat transportation at this location. After 25 min, hydrogenation of MH-TiF₄-MWCNT completes, confirmed by temperature reduction to the initial value. The temperature of the heat exchanger increases from 27 to about 100 °C indicating the successful heat transfer from exothermic rehydrogenation.

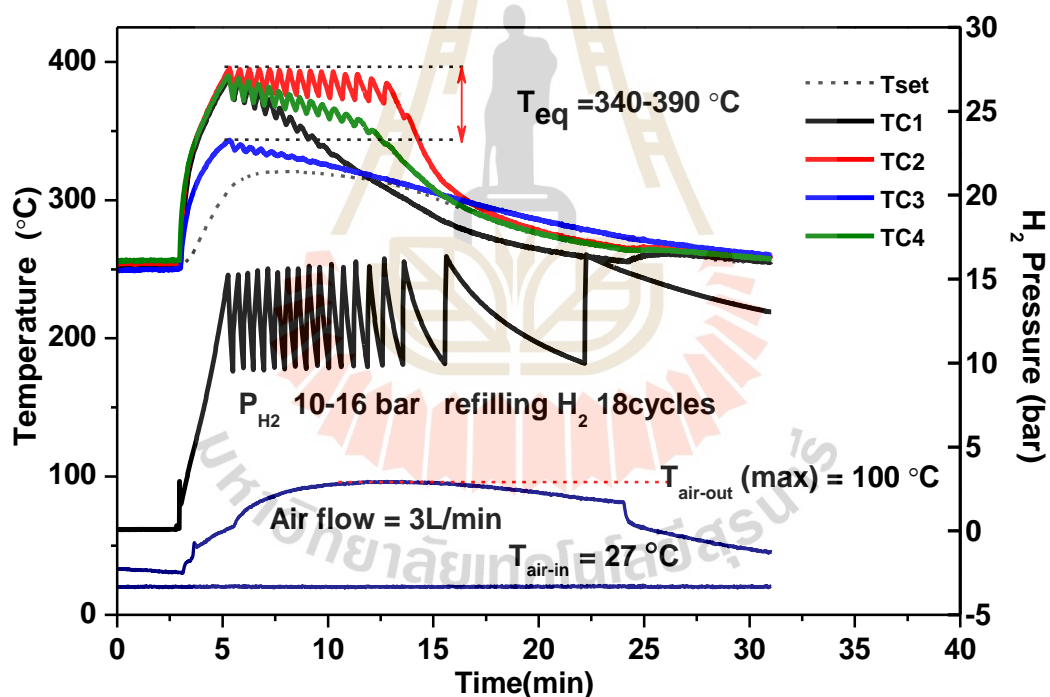


Figure 4.16 Hydrogenation of MH-TiF₄-MWCNT based tank at isothermal condition (T_{set} = 250 °C under 10-16 bar H_2).

Moreover, cycling stability of MH-TiF₄-MWCNT based tank upon 20 cycles is studied. Figure 4.17 shows average total and material capacity of 5.60 and 5.40 wt.% H_2 , respectively, corresponding to 82% of theoretical capacity. These are superior to the results of the MgH₂-based tank without heat exchanger (3.4-3.6 wt.% H_2 and 50-52 %

of theoretical value) previously reported (Thongtan et al., 2018). Thus, the enhanced kinetics and reversibility of MH-TiF₄-MWCNT based tank is explained by not only catalytic effects of TiF₄ and MWCNTs but also effective heat exchanger.

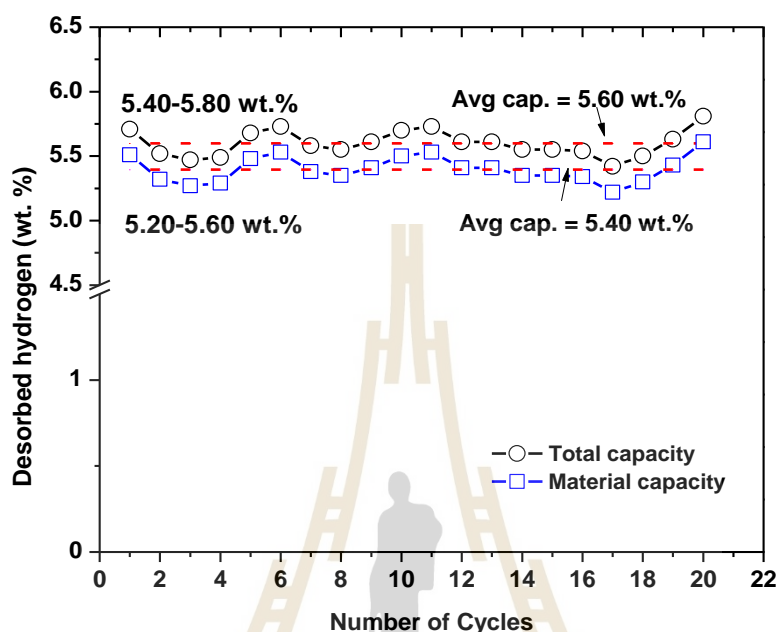


Figure 4.17 Cycling stability upon 20 de/rehydrogenation cycles of MH-TiF₄-MWCNT based tank.

Furthermore, phases composition of the powder sample after the 20th hydrogenation is investigated by PXD. Figure 4.18 shows the diffraction peaks of MgH₂ with slightly Mg, suggesting partial irreversibility. From the inset of Figure 4.19, fine powder of the MH-TiF₄-MWCNT sample after the 20th hydrogenation is observed. Upon cycling at high temperature (>400 °C), MgH₂ tends to agglomerate or sinter. In this study, the storage tank together with heat exchanger able to transport heat up to 75 °C during exothermic rehydrogenation. This benefits the hydrogen sorption kinetics, and cycling stability of MH-TiF₄-MWCNT based tank.

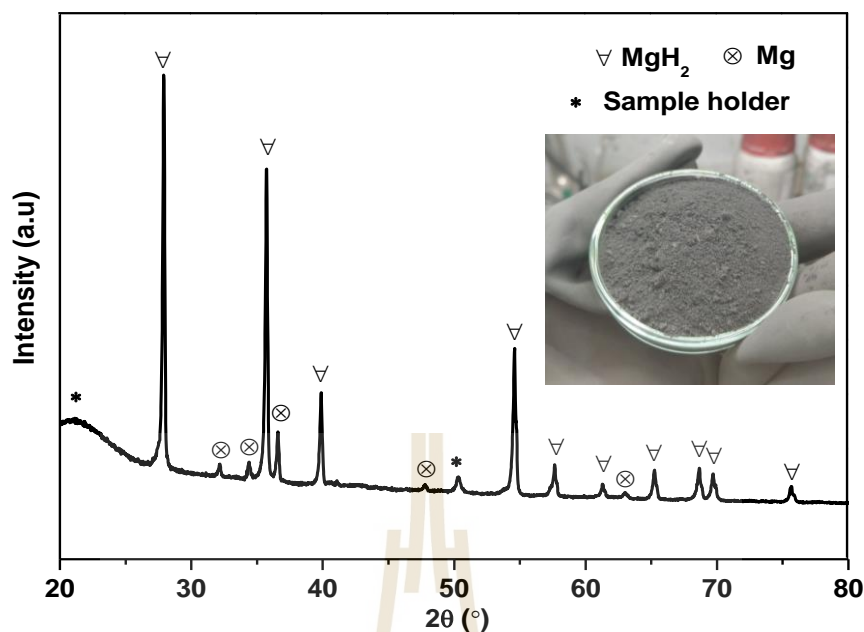


Figure 4.18 PXD spectrum and physical appearance (inset) of MH-TiF₄-MWCNT after the 20th hydrogenation.

The electrical production of proton exchange membrane fuel cell (PEMFC) stack coupled with MH-TiF₄-MWCNT tank is investigated. Prior to the experiment, the voltage (V), current (I), and power (W) of PEMFC stack are measured at different flow rates of 0.10-0.25 SLM to find the most suitable H₂ flow rates (Figure 4.19(A)). The open-circuit voltages of all flow rates are ~11 V, approaching to the specification from the manufacture (12 V). The maximum current and power are increased from 0.8 to 2.5 A and 6.7 to 20.0 W, respectively, with increasing the hydrogen flow rates. Although, the experiment flow rate of 0.25 SLM reveals maximum current and power, the tank can provide this constant flow rate for only 30 min. Therefore, the H₂ flow rate of 0.1 SLM is selected for the experiment using constant current mode at room temperature. Figure 4.19(B) shows the constant current and power of 0.6 A and 5.6 W, respectively, for 2 h 30 min. There is a small fluctuation of power caused by the produced water blocking cathode air hole and disturbing the air transfer. Therefore, the water management is pretty important for stable system operation in the long term uses (Fernández-M et al., 2013 and Kim et al., 2014). In conclusion, total hydrogen capacity used for PEMFC stack is 4.3 wt.% H₂, resulting in the electrical power of 19 Wh.

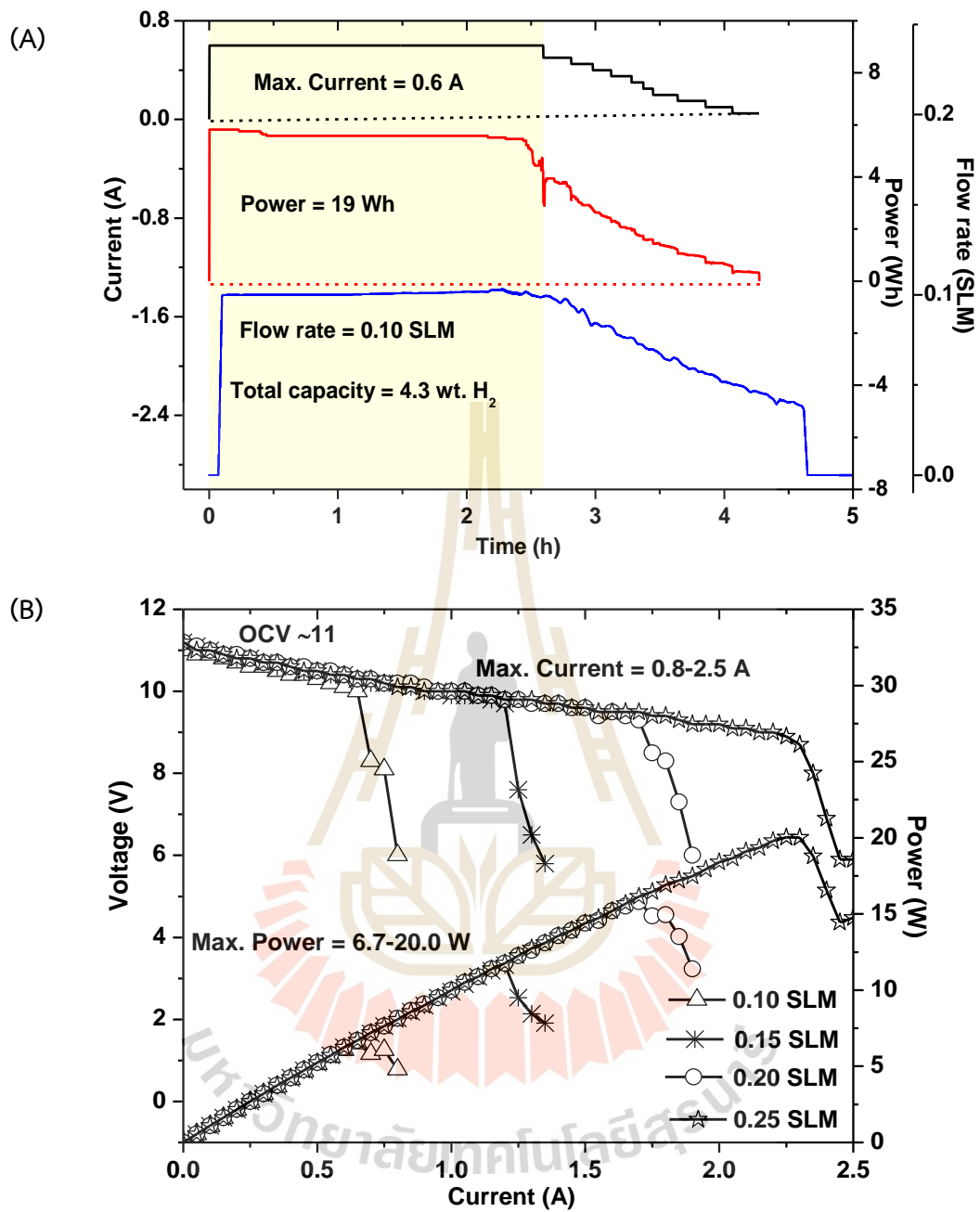


Figure 4.19 Polarization curve (A) and electrical performance (B) of PEMFC stack supplied with hydrogen gas from MH-TiF₄-MWCNT tank.

Table 4.5 Specification of PEMFC stack supplying hydrogen from MH-TiF₄-MCNT tank.

Specification	Values
Total electric energy	19 Wh
Constant current	0.6 A
Constant power	5.6 W
Maintaining time	150 min
Flow rate	0.10 SLM
Total hydrogen storage capacity	4.3 wt.% H ₂
Volume metric capacity (Vs)	23.17 SLM
Sample mass	45.15 g

4.4 References

- Batalovic, K., Radakovic, J., Belosevic-Cavor, J., and Koteski, V. (2014). Transition metal doping of Mg₂FeH₆-a DFT insight into synthesis and electronic structure. *Physical Chemistry Chemical Physics*, 16(24), 12356-12361. doi:10.1039/c4cp01020e.
- Bösenberg, U., Doppiu, S., Mosegaard, L., Barkhordarian, G., Eigen, N., Borgschulte, A., Jensen, T. R., Cerenius, Y., Gutfleisch, O., and Klassen, T. (2007). Hydrogen sorption properties of MgH₂-LiBH₄ composites. *Acta Materialia*, 55(11), 3951-3958.
- Bösenberg, U., Ravnsbæk, D. B., Hagemann, H., D'Anna, V., Minella, C. B., Pistidda, C., Van Beek, W., Jensen, T. R., Bormann, R., and Dornheim, M. (2010). Pressure and temperature influence on the desorption pathway of the LiBH₄-MgH₂ composite system. *The Journal of Physical Chemistry C*, 114(35), 15212-15217.
- Chaise, A., de Rango, P., Marty, P., and Fruchart, D. (2010). Experimental and numerical study of a magnesium hydride tank. *International Journal of Hydrogen Energy*, 35(12), 6311-6322. doi:10.1016/j.ijhydene.2010.03.057.
- Chaise, A., De Rango, P., Marty, P., Fruchart, D., Miraglia, S., Olivès, R., and Garrier, S. (2009). Enhancement of hydrogen sorption in magnesium hydride using expanded natural graphite. *International Journal of Hydrogen Energy*, 34(20), 8589-8596.

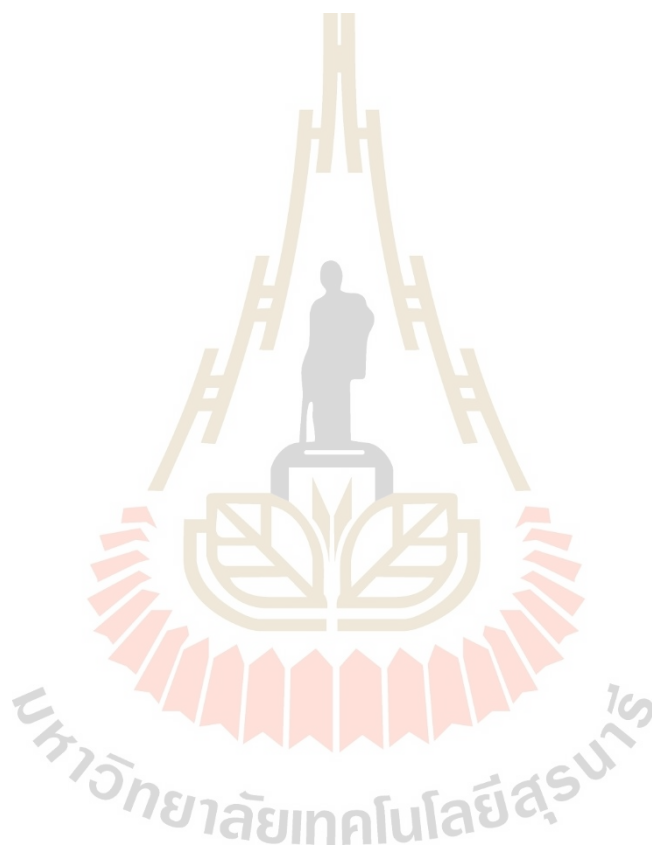
- Chen, X., Zou, J., Huang, S., He, G., Zhao, N., Zeng, X., Zeng, X., and Ding, W. (2018). Hydrogen storage in $Mg_2Ni(Fe)H_4$ nano particles synthesized from coarse-grained Mg and nano sized Ni(Fe) precursor. *RSC Advances*, 8(34), 18959-18965. doi: 10.1039/c8ra01963k.
- Chen, X., Zou, J., Zeng, X., and Ding, W. (2016). Hydrogen storage in $Mg_2Fe(Ni)H_6$ nanowires synthesized from coarse-grained Mg and nano sized γ -Fe(Ni) precursors. *International Journal of Hydrogen Energy*, 41(33), 14795-14806. doi:10.1016/j.ijhydene.2016.06.024.
- De Rango, P., Wen, J., Skryabina, N., Laversenne, L., Fruchart, D., and Borges, M. (2020). Hydrogen Storage Properties of Mg-Ni Alloys Processed by Fast Forging. *Energies*, 13(13). doi:10.3390/en13133509.
- Fang, Z. Z., Kang, X. D., and Wang, P. (2010). Improved hydrogen storage properties of $LiBH_4$ by mechanical milling with various carbon additives. *International Journal of Hydrogen Energy*, 35(15), 8247-8252.
- Fernández, M. J., Guelbenzu, G., Martín, A. J., Folgado, M. A., Ferreira, A. P., and Chaparro, A, M. (2013). A portable system powered with hydrogen and one single air-breathing PEM fuel cell. *Applied Energy*, 109, 60-66. doi:10.1016/j.ap-energy.2013.03.076.
- Garrier, S., Delhomme, B., de Rango, P., Marty, P., Fruchart, D., and Miraglia, S. (2013). A new MgH_2 tank concept using a phase-change material to store the heat of reaction. *International Journal of Hydrogen Energy*, 38(23), 9766-9771. doi:10.1016/j.ijhydene.2013.05.026.
- Hoffmann, M. M., Darab, J. G., Palmer B. J., and Fulton, J. L. (1999). A Transition in the Ni^{2+} Complex Structure from Six- to Four-Coordinate upon Formation of Ion Pair Species in Supercritical Water An X-ray Absorption Fine Structure, Near-Infrared, and Molecular Dynamics Study. *The Journal of Physical Chemistry A*, 103, 8471-8482.
- Kalinichenka, S., Röntzsch, L., Baetz, C., Weißgärber, T., and Kieback, B. (2011). Hydrogen desorption properties of melt-spun and hydrogenated Mg-based alloys using in situ synchrotron X-ray diffraction and TGA. *Journal of Alloys and Compounds*, 509, S629-S632. doi:10.1016/j.jallcom.2010.10.067.

- Witek, K., Karpowicz, M., and Polanski, M. (2018). Mg₂FeH₆ Synthesis Efficiency Map. *Crystals*, 8(2). doi:10.3390/cryst8020094.
- Khan, D., Panda, S., Ma, Z., Ding, W., and Zou, J. (2020). Formation and hydrogen storage behavior of nanostructured Mg₂FeH₆ in a compressed 2MgH₂-Fe composite. *International Journal of Hydrogen Energy*, 45(41), 21676-21686. doi:10.1016/j.ijhydene.2020.06.025.
- Kim, K. B., Shim, J. H., Park, S. H., Choi, I. S., Oh, K. H., and Cho, Y. W. (2015). Dehydrogenation reaction pathway of the LiBH₄-MgH₂ composite under various pressure conditions. *The Journal of Physical Chemistry C*, 119(18), 9714-9720.
- Kim, S. H., Miesse, C. M., Lee, H. B., Chang, I. W., Hwang, Y. S., Jang, J. H., and Cha, S. W. (2014). Ultra compact direct hydrogen fuel cell prototype using a metal hydride hydrogen storage tank for a mobile phone. *Applied Energy*, 134, 382-391. doi:10.1016/j.apenergy.2014.08.019.
- Li, C., Wu, Z. W., and Zhang, Q. A. (2018). Synthesis and hydrogen desorption kinetics of Mg₂FeH₆-and Mg₂CoH₅-based composites with in situ formed YH₃ and Mg₂NiH₄ nanoparticles. *Rare Metals*. doi:10.1007/s12598-018-1174-z.
- Li, Q., Xu, K., Chou, K., Lu, X., and Lin, Q. (2006). Kinetics of hydrogen absorption and desorption of a mechanically milled MgH₂ + 5at% V nanocomposite. *Journal of University of Science and Technology Beijing, Mineral, Metallurgy, Material*, 13(4), 359-362. doi:10.1016/s1005-8850(06)60074-1.
- Luo, Q., Gu, Q. F., Zhang, J. Y., Chen, S. L., Chou, K. C., and Li, Q. (2015). Phase Equilibria, Crystal Structure and Hydriding/Dehydriding Mechanism of Nd₄Mg₈₀Ni₈ Compound. *Scientific Reports*, 5, 15385. doi:10.1038/srep15385.
- Nyallang, N. S., Yartys, V., and Lototsky, M. (2018). Synthesis of Mg₂FeH₆ assisted by heat treatment of starting materials. *Materials Today: Proceedings*, 5(4), 10533-10541. doi:10.1016/j.matpr.2017.12.385.
- Pinitsoontorn, S., Prasoetsopha, N., Srepusharawoot, P., Bootchanont, A., Kidkhunthod, P., Kamwanna, T., Amornkitbamrung, V., Kurosaki, K., and Yamanaka, S. (2014). Local structure determination of substitutional elements in Ca₃Co_{4-x}MxO₉ (M = Fe, Cr, Ga) using X-ray absorption spectroscopy. *physica status solidi (a)*, 211(8), 1732-1739. doi:10.1002/pssa.201330493.

- Pitt, M. P., Paskevicius, M., Brown, D. H., Sheppard, D. A., and Buckley, C. E. (2013). Thermal stability of $\text{Li}_2\text{B}_{12}\text{H}_{12}$ and its role in the decomposition of LiBH_4 . *Journal of the American Chemical Society*, 135(18), 6930-6941. doi:10.1021/ja400131b.
- Plerdsranoy, P., Chanthee, S., and Utke, R. (2017). Compaction of $\text{LiBH}_4\text{-MgH}_2$ doped with MWCNTs- TiO_2 for reversible hydrogen storage. *International Journal of Hydrogen Energy*, 42(2), 978-986.
- Plerdsranoy, P., Javadian, P., Jensen, N. D., Nielsen, U. G., Jensen, T. R., and Utke, R. (2017). Compaction of $\text{LiBH}_4\text{-LiAlH}_4$ nanoconfined in activated carbon nanofibers: Dehydrogenation kinetics, reversibility, and mechanical stability during cycling. *International Journal of Hydrogen Energy*, 42(2), 1036-1047.
- Pohlmann, C., Röntzsch, L., Heubner, F., Weißgärber, T., and Kieback, B. (2013). Solid-state hydrogen storage in Hydralloy-graphite composites. *Journal of Power Sources*, 231, 97-105.
- Pohlmann, C., Röntzsch, L., Kalinichenka, S., Hutsch, T., and Kieback, B. (2010). Magnesium alloy-graphite composites with tailored heat conduction properties for hydrogen storage applications. *International Journal of Hydrogen Energy*, 35(23), 12829-12836. doi:10.1016/j.ijhydene.2010.08.104.
- Polanski, M., Nawra, D., and Zasada, D. (2019). Mg_2FeH_6 synthesized from plain steel and magnesium hydride. *Journal of Alloys and Compounds*, 776, 1029-1040. doi:10.1016/j.jallcom.2018.10.310.
- Polanski, M., Płociński, T., Kunce, I., and Bystrzycki, J. (2010). Dynamic synthesis of ternary Mg_2FeH_6 . *International Journal of Hydrogen Energy*, 35(3), 1257-1266. doi:10.1016/j.ijhydene.2009.09.010.
- Ranjbar, A., Guo, Z. P., Yu, X. B., Attard, D., Calka, A., and Liu, H. K. (2009). Effects of SiC nanoparticles with and without Ni on the hydrogen storage properties of MgH_2 . *International Journal of Hydrogen Energy*, 34(17), 7263-7268. doi:10.1016/j.ijhydene.2009.07.005.
- Ravel, B., and Newville, M. (2005). ATHENA, ARTEMIS, HEPHAESTUS: data analysis for X-ray absorption spectroscopy using IFEFFIT. *Journal of Synchrotron Radiation*, 12(4), 537-541. doi:10.1107/S0909049505012719.

- Shao, H., Felderhoff, M., and Weidenthaler, C. (2015). Kinetics Enhancement, Reaction Pathway Change, and Mechanism Clarification in LiBH_4 with Ti-Catalyzed Nanocrystalline MgH_2 Composite. *The Journal of Physical Chemistry C*, 119(5), 2341-2348.
- Shim, J. H., Park, M., Lee, Y. H., Kim, S., Im, Y. H., Suh, J. Y., and Cho, Y. W. (2014). Effective thermal conductivity of MgH_2 compacts containing expanded natural graphite under a hydrogen atmosphere. *International Journal of Hydrogen Energy*, 39(1), 349-355.
- Sitthiwet, C., Thiangviriyaya, S., Thaweelap, N., Meethom, S., Kaewsuwan, D., Chanlek, N., and Utke, R. (2017). Hydrogen sorption and permeability of compacted LiBH_4 nanoconfined into activated carbon nanofibers impregnated with TiO_2 . *Journal of Physics and Chemistry of Solids*, 110, 344-353.
- Thaweelap, N., Thongtan, P., Sitthiwet, C., Thiangviriyaya, S., Eiamlamai, P., and Utke, R. (2017). Hydrogen sorption, kinetics, reversibility, and reaction mechanisms of MgH_2 -x LiBH_4 doped with activated carbon nanofibers for reversible hydrogen storage based laboratory powder and tank scales. *International Journal of Hydrogen Energy*, 42(39), 24915-24926.
- Thongtan, P., Dansirima, P., Thiangviriyaya, S., Thaweelap, N., Suthummapiwat, A., Plerdsranoy, P., and Utke, R. (2018). Reversible hydrogen sorption and kinetics of hydrogen storage tank based on MgH_2 modified by TiF_4 and activated carbon. *International Journal of Hydrogen Energy*, 43(27), 12260-12270. doi:10.1016/j.ijhydene.2018.04.171.
- Yan, Y., Li, H. W., Maekawa, H., Miwa, K., Towata, S. i., and Orimo, S. i. (2011). Formation of intermediate compound $\text{Li}_2\text{B}_{12}\text{H}_{12}$ during the dehydrogenation process of the LiBH_4 - MgH_2 system. *The Journal of Physical Chemistry C*, 115 (39), 19419-19423.
- Zhang, J., Zaïdi, W., Paul-Boncour, V., Provost, K., Michalowicz, A., Cuevas, F., Latroche, M., Belin, S., Bonnet, J. P., and Aymard, L. (2013). XAS investigations on nanocrystalline Mg_2FeH_6 used as a negative electrode of Li-ion batteries. *Journal of Materials Chemistry A*, 1(15). doi:10.1039/c3ta01482g.

- Zhao, Y., Ding, L., Zhong, T., Yuan, H., and Jiao, L. (2014). Hydrogen storage behavior of $2\text{LiBH}_4/\text{MgH}_2$ composites improved by the catalysis of CoNiB nanoparticles. *International Journal of Hydrogen Energy*, 39(21), 11055-11060.
- Zhou, C., Zhang, J., Bowman, R. C., and Fang, Z. Z. (2021). Roles of Ti-Based Catalysts on Magnesium Hydride and Its Hydrogen Storage Properties. *Inorganics*, 9(5). doi:10.3390/inorganics9050036.

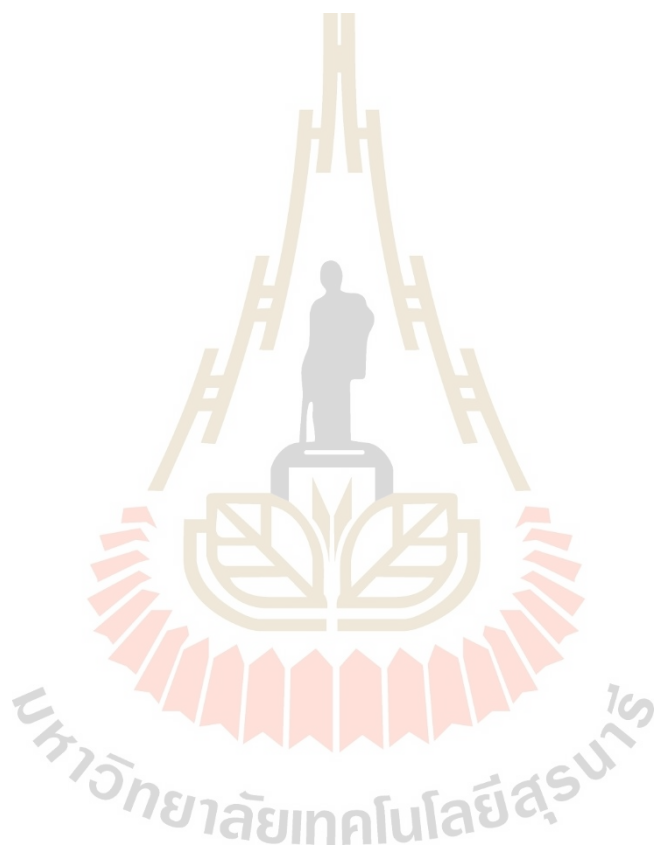


CHAPTER V

CONCLUSIONS

In this work, we focused on the improvement of hydrogen sorption properties of MgH_2 -based hydrogen storage in laboratory and tank scale. The strategies in laboratory scale consisted of (i) compositing with LiBH_4 and doping with activated carbon nanofibers (ACNFs) and (ii) doping with Ni into MgH_2/Fe system. For upscaling to storage tank, the performance of MgH_2 doped with TiF_4 and multi-walled carbon nanotubes (MWCNTs) was investigated. We started with the compacted $2\text{LiBH}_4\text{-MgH}_2$ doped with ACNFs. Dehydrogenation temperature and activation energy of compacted $2\text{LiBH}_4\text{-MgH}_2$ reduced from 360 to 275 °C and from 130-251 to 103-167 kJ/mol, respectively, after doping with ACNFs. Moreover, mechanical stability upon cycling, hydrogen permeability, and heat transfer were also significantly enhanced. These led to superior hydrogen sorption kinetics of the compacted $2\text{LiBH}_4\text{-MgH}_2$. Furthermore, de/rehydrogenation performance and mechanisms of Ni-doped Mg_2FeH_6 (5 and 20 wt.% Ni) were of interest. As-prepared Mg_2FeH_6 showed single-step dehydrogenation at 250 °C with 5.4 wt.% H_2 , while Ni-doped Mg_2FeH_6 performed two-step reaction at 170 and 220-250 °C of Mg_2NiH_4 and Mg_2FeH_6 , respectively. By increasing Ni-loading contents from 5 to 20 wt.%, the substitution of Ni for Fe in Mg_2FeH_6 to form $\text{Mg}_2\text{Fe}_{0.75}\text{Ni}_{0.25}\text{H}_6$ was observed, providing storage capacity of 3.70 wt.% H_2 . The formation of $\text{Mg}_2\text{Fe}_{0.75}\text{Ni}_{0.25}\text{H}_6$ improved hydrogen sorption kinetics, in terms of the reduction of onset dehydrogenation temperature (~80 °C) and cycling stability. For upscaling, a $\text{MgH}_2\text{-TiF}_4\text{-MWCNT}$ -based tank with central tube heat exchanger was proposed. Dehydrogenation and rehydrogenation ($T = 250\text{-}300$ °C and $p(\text{H}_2) = 1.2\text{-}16$ bar) completed within 120-150 and 25 min, respectively. Upon the 20th cycling, average total and material capacities of 5.60 and 5.40 wt.% H_2 , respectively, were obtained without hydride particle agglomeration. The enhanced kinetics and reversibility of the $\text{MH-TiF}_4\text{-MWCNT}$ tank were explained by not only catalytic effects of TiF_4 and MWCNTs but also effective heat exchanger system. Moreover, electrical performances of the

PEMFC stack coupled with the $\text{MgH}_2\text{-TiF}_4\text{-MWCNTs}$ tank at a constant hydrogen flow rate of 0.1 SLM showed the maintained current and power of 0.6 A and 5.6 W, respectively, for 2 h 30 min, leading to total electrical power of 19 Wh.



CURRICULUM VITAE

Name Miss Sophida Thiangviriya

Date of Birth 1st July 1988

Place of Birth Nakhonrachsima, Thailand

Education (Include dates, Major and Details of Degrees, University)

2007-2010 B.Sc. (Chemistry), Rajamankala University of Technology Isan. Thailand

2011-2013 M.Sc. (Chemistry), Suranaree University of Technology, Thailand

2016-2021 Ph.D. (Chemistry), Suranaree University of Technology, Thailand

Publications

Thiangviriya, S., Sitthiwet, C., Plerdsranoy, P., Capurso, G., Pistidda, C., Utke, O., Dornheim, M., Klassen, T., Utke, R. (2019) Hydrogen sorption kinetics, hydrogen permeability, and thermal properties of compacted 2LiBH_4 – MgH_2 doped with activated carbon nanofibers. *Int. J. Hydrogen Energy*. 44(29), pp. 15218-15227.

Thiangviriya, S., Plerdsranoy, P., Sitthiwet, Ch., Dansirima, P., Thongtan, P., Eiamlamai, P., Utke, O., Utke, R. (2019) MgH_2 – TiF_4 –MWCNTs based hydrogen storage tank with central tube heat exchanger. *Int. J. Hydrogen Energy*, 44 (36), pp. 20173-20182.

Thiangviriya, S., Plerdsranoy, P., Hagenah, A., Le, T, T., Kidkhunthod, P., Utke, O., Dornheim, M., Klassen, T., Pistidda, C., Utke, R. (2021) Effects of Ni-loading contents on dehydrogenation kinetics and reversibility of Mg_2FeH_6 . *Int. J Hydrogen Energy*. 46(63), pp. 32099-32109.

Grants and Fellowships The Royal Golden Jubilee (RGJ) Ph.D. Programme,
The Thailand Research Fund (TRF)